Novel DNA-Templated Nanotechnology Devices

David James Stokoe

A thesis submitted for the degree of Doctor of Philosophy

November 2023

Abstract

This thesis describes the preparation and characterisation of DNA-templated nanowires followed by their incorporation into field effect transistors.

DNA has been used as a template in order to grow nanowires consisting of vanadium dioxide (VO_2), cadmium sulphide (CdS) and a cadmium sulphide - carbon nanotube mixture (CNT-CdS) via a precipitation reaction. The growth of these nanowires is a two stage process in which the materials first coordinate with DNA before nucleating and then growing to form long and smooth wire like structures.

The novel VO_2 nanowires formed have been characterised using a mixture of Fourier Transform Infrared Spectroscopy (FTIR), UV-Visible Spectroscopy (UV-Vis), Powder X-ray Diffraction (pXRD) and X-ray Photoelectron Spectroscopy (XPS) in which it was found that the vanadium interacted with the DNA and formed a product with a structure similar to VO_2 nanorods. Further investigations were carried out by using Atomic Force and Scanned Conductance Microscopy (AFM and SCM respectively) which showed long wire-like structures with heights upwards of 8 nm that showed weakly conducting nature when probed with SCM. AFM studies also showed that without DNA being present, no wire like structures were formed. Basic current-voltage (IV) curves were recorded over a range of temperatures using platinum interdigitated electrodes (IDEs) which confirmed the weakly conducting nature of the nanowires and that they showed Arrhenius behaviour. The conductance of the prepared nanowires was noticeably higher than any other DNA-templated nanowires prepared in past studies. Finally the samples were incorporated into field effect transistors (FET) and the source-drain current was measured as the gate voltage was altered. The FETs showed basic transistor functionality in which at larger gate voltages the current between the source and drain also increased. The effect of temperature was also examined for the VO_2-DNA nanowires where it was discovered that heating the samples to 150 $^{\circ}\mathrm{C}$ caused an irreversible rise in conductance.

The CdS nanowires have been characterised in the past however and AFM was used to confirm the formation of nanowires, which showed a diameter of around 6 - 8 nm. IV curves were again recorded over a range of temperatures using IDEs and the samples showed thermally-activated conductivity. The CdS-DNA nanowires were then incorporated into FETs but showed no reliable transistor like behaviour. This is thought to be due to the low conductance of the material as well as the high contact resistance.

The final material investigated was CdS-CNT-DNA in which the DNA was wrapped around multi-walled carbon nanotubes (MWCNTs) before CdS was added. FTIR of this material showed distinct differences in wavenumbers for bare DNA and the templated DNA, showing signs that an interaction is occurring. This was confirmed by using AFM in which wire like structures with heights of 4 nm. In the absence of DNA no wire like structures form, only small particles with heights of 8 - 12 nm. IV curves showed good conductance and by measuring over a temperature range, the materials semiconducting properties were confirmed. The samples were then incorporated into FETs and they showed basic transistor behaviour with a low transconductance.

Acknowledgements

I would like to take this opportunity to give my thanks to everyone who has contributed and supported the work described in this thesis. I am immensely grateful to my supervisors Dr Benjamin Horrocks, Professor Andrew Houlton and Professor Nicholas Wright for their constant support, guidance and knowledge. Without them this thesis would not be possible and I thank them for giving me the opportunity to grow as a research scientist and achieve my very best.

I wish to thank Dr Osama El-Zubir who was always very generous with his time and was always happy to help with any problems I went to him with. I would also like to thank him for his assistance during AFM imaging. Special thanks to Dr Jamie Gould for his help with capturing and analysing pXRD data.

During my time at Newcastle University I have had the pleasure of working with many future friends. I am especially thankful to Dr Pablo Rojas who helped and mentored me during the start of my time on the nano-corridor. I am also thankful for Liam McGarry, Marcello D'Avino, Charlotte Cummings and Morag Grierson who were a constant source of support and fun during my time on the nano-corridor.

I am very fortunate to have an extraordinary family who have always been supportive and encouraging throughout my education. I would like to thank my mam and dad for always being there for me when I needed them, for their constant support and for always listening even if they didn't understand a thing! I am thankful for encouragement from my two sisters Laura and Sarah as well my gran Anne. Finally I am thankful to my girlfriend Sally who always pushed me to work harder and constantly improve.

I am extremely grateful to have been given the opportunity to continue my studies and I would like to express my gratitude to the Engineering and Physical Sciences Research Council for funding my studentship.

Contents

Abbreviations

AFM	Atomic force microscopy
BJT	Bipolar junction transistor
cm	Centimetre
CNT	Carbon nanotube
DNA	Deoxyribonucleic acid
EBPVD	Electron beam physical vapour deposition
eV	Electron volt
EFM	Electrostatic force microscopy
FET	Field effect transistor
FTIR	Fourier transform infrared spectroscopy
IDE	Interdigitated electrode
IPA	Isopropyl alcohol
IPR	Image reversal photoresist
IV	Current - voltage
kV	Kilovolt
$\mu\mathrm{A}$	Microampere
mA	Milliampere
mDNA	Metallo-DNA
(mg)	Milligram
MIT	Metal insulator transition
$\mu\mathrm{L}$	Microlitre
mL	Millilitre
$\mu\mathrm{m}$	Micrometre
mmol	Millimole

MOSFET	Metal oxide field effect transistor
μS	Microsiemens
mS	Millisiemens
mV	Millivolt
mW	Millwatt
MWCNT	Multi-walled carbon nanotube
nA	Nanoampere
ng	Nanogram
nm	Nanometre
NMP	N-Methyl-2-pyrrolidone
nS	Nanosiemens
PR	Photoresist
pXRD	Powder X-ray diffraction
rpm	Revolutions per minute
SWCNT	Single-walled carbon nanotube
TFT	Thin film transistor
UV-Vis	UV-Visible spectroscopy
V	Voltage
XPS	X-ray photoelectron spectroscopy

Chapter 1

Introduction

1.1 Introduction

Ever since the discovery of DNA's structure by Watson and Crick in 1953 there has been a keen interest in potential electronic applications with Eley and Spivey already claiming it could be used as an electrical conductor in 1962.[1,2] The ability of duplex DNA to act as an electrical conductor has, over time, been the subject of contradictory views due to the conflicting evidence found. It has now however, been accepted that at lengths greater than a few nm it is a poor solid state electronic conductor.[3] For this reason, various methods have been attempted in order to add conductive properties to duplex DNA. The area this research covers is DNA templating. In this, positive metal ions can bind to the negative phosphate backbone of DNA and may subsequently be reduced to elemental metal or precipitated as binary semiconductors. The inorganic material initially forms as small particles, but then may transform into a long continuous wire in a process analogous to Ostwald ripening.[4] Ideally this creates a conductive wire which is a few nm thick but with a length of several $\mu\mathrm{m}$ determined by the length of the DNA template.

In electronics, a transistor is used to either amplify or switch an electronic signal and currently silicon is the material of choice to prepare them. Each transistor has two distinct states which correspond to binary 0s and 1s making them the basis of all modern electronics. Difficulties have arisen when trying to further decrease the size of silicon based transistors due to short channelling effects.[5–7] It is thought that by incorporating the prepared nanowires as the semiconducting material, transistors can be further decreased in size.

1.2 DNA

1.2.1 Duplex DNA

Duplex deoxyribonucleic acid (DNA) is made up of two polymer strands that together form a double helix. Each strand is made up of nucleotides which themselves are made up of four bases: adenine (A), guanine (G), thymine (T) and cytosine (C). Owing to complementary hydrogen bonding, A and T bind together, as do C and G, which can be seen in figure 1.1. Each of these nucleobases are attached to a sugar and a phosphate group which together make up a nucleotide. The sugar in each nucleotide binds to the phosphate of the next nucleotide and in doing so creates a sugar-phosphate backbone which adds structure and rigidity to the double stranded DNA.

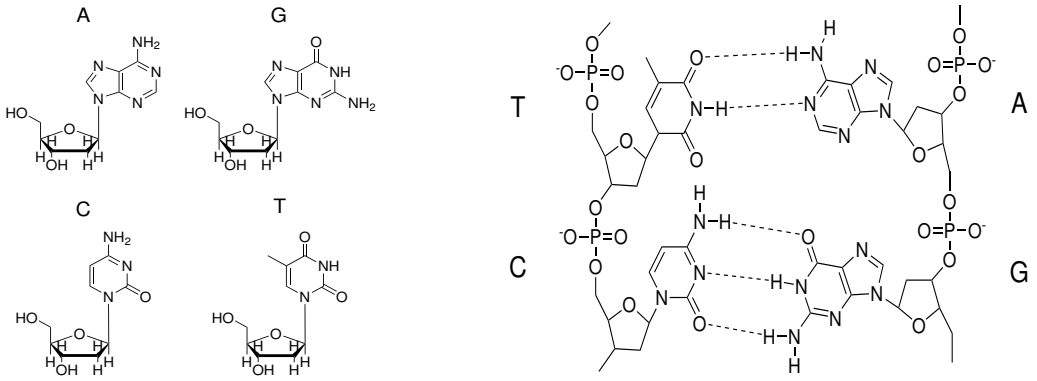

Figure 1.1: The four nucleobases that make up duplex DNA (left).The hydrogen bonding between the complementary base pairs AT and GC (right).

The structure of DNA may be long and is extremely thin at 2 nm in width. This would make it ideal as a building block for nanoscale electronics however early research into the conductivity of DNA yielded contrasting results in both practical and computational methods. The first measurements on DNA mainly involved intercalated donor and acceptor molecules in which the charge transport was measured.[8–10] One of the first direct electrical measurements of DNA was by Fink and Schönenburger in 1999. An ultra high vacuum was used in order to eliminate any contamination. In the experimental, a 600 nm length of DNA was spanned across a hole and attached to a gold plated sample holder. A tip was then brought down to the surface of the DNA strand and a potential applied between the tip and the sample holder.[11] They found that the DNA strands had resistance values in the

range expected for semiconductors. Okahata's group also claimed that DNA showed ohmic behaviour when in a water insoluble lipid film. In their research, a DNA lipid solution was prepared in order to dispel water and this was then cast over gold electrodes. They report conductivities that can be compared to conducting polymers such as polyacetylene and polyphenylene.[12] In contrast to this, there were also experiments showing DNA acted as an insulator with the strongest argument coming from Storm *et al*. In their research lithography was used to create gold or platinum electrodes with gaps ranging between 200 and 500 nm. A range of experiments were carried out in which a variety of base sequences and distances were used. Ultimately they concluded that with a resistance value of 1 TΩ, DNA is an insulating material.[13] A different method was used by de Pablo *et al* in which the same result was found. In this a gold electrode was evaporated onto a mica substrate in which DNA had already been deposited allowing for a solid contact between the electrode and DNA. To make contact with a second electrode a scanning force microscopy tip was metallised with gold before being brought down onto a single DNA molecule. Over a horizontal distance of around 70 nm a minimum resistance of 10^{16} Ω was found again showing DNA to act as an insulator.[14]

Over the years there has been much interest in how charge is transported through DNA molecules not only by chemists but physicists and biologists due to its potential uses. Even though DNA is classed as an insulator at longer distances, charge transfer is still possible over short distances and it is believed to occur via both coherent tunnelling and incoherent hopping.[15] Guanine has the lowest oxidation potential of the four bases present in DNA[16] making this the most likely base for hopping to occur however adenine can also facilitate hopping if there is a distance of 3 or more base pairs between guanines.[17] A diagram of this process can be found in figure 1.2. Tunnelling on the other hand takes place when there is a large gap between guanines and occurs between a donor and acceptor molecule. Tunnelling makes use of the overlapping stacked π system to allow an exchange through over-lapping orbitals.[18] Tunnelling is not viable for long range transfer due to the exponential increase in resistance with the tunnelling length,[19] whereas the resistance increases linearly with molecule length in hopping.[20]

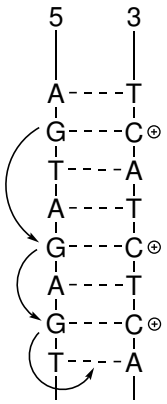

Figure 1.2: A diagram showing the route taken during hopping with the electron ending at an acceptor molecule.

An interesting feature of DNA is its ability to form large, complex and controllable structures as shown by Rothemund in 2006.[21] He showed that single stranded DNA can be folded into complex 2-dimensional shapes by using oligonucleotides to create a scaffolding to which single strands can bind and self assemble. Examples of this can be seen in figure 1.3 This allows DNA to be used as a programmable building block with uses including nano-electronics, drug delivery systems and DNA robotics. More about this will be discussed in further sections.

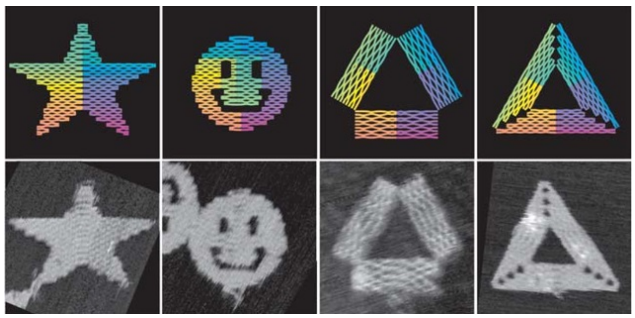

Figure 1.3: An example of some of the shapes created by Rothemund using DNA origami.[21]

1.2.2 Modified DNA

For DNA to be used as a semiconducting device, modifications are required to add conductivity into the molecule. This has been done in a ways such as metallo-DNA and the use of DNA as a template on which conductive material can be grown.

Metallo-DNA

Metals are excellent carriers of electrons due to the absence of a gap between the valence and conduction bands meaning there are many ”free electrons” that can travel throughout the lattice. To prepare metallo-DNA (mDNA), metal is inserted into the hydrogen bonds between bases in a double stranded DNA helix to create new base-metal-base coordinate bonds as seen in figure 1.4.[22]

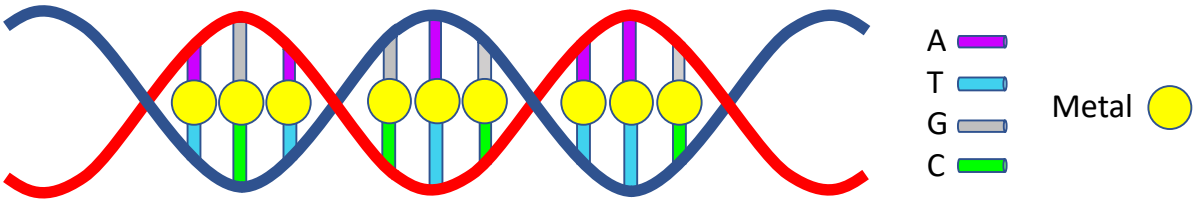

Figure 1.4: A figure showing how metals are incorporated into the DNA double helix during the preparation of mDNA[22]

The first example of mDNA was by Katz in 1963 in which mercury was used to create a thymine-mercury-thymine base pair[23] and since then the area has received great amounts of attention.[24] More recently Aich and his group successfully displaced the imino protons in the DNA bases and replaced them with Zn^{2+} ions causing it to coordinate to the N3 of thymine and N1 of guanine.[25] They report that the mDNA acts as a molecular wire due to the quenching of the fluorescence of a fluorophore showing charge transfer is occurring. Using this they were then able to create a bioactive switch with the addition of EDTA to the sample. Silver ions are now the most used reagent in metallo-DNA owing to their preference for binding to endocyclic ring nitrogen, meaning they are more easily incorporated into the natural base pairs.[26] However even with this, the ability to incorporate metal ions into DNA is synthetically challenging. A new approach however utilises artificial bases in which the metal binding potential is maximised due to increasing the amount of binding sites on the base.[27] A good example of this is from Tanaka *et al* in which they prepare a novel binding motif into the duplex DNA which can be found in figure 1.5.[28–30]

It is possible to then insert compatible artificial bases into duplex DNA to which a metal can then bind. This was first achieved by Meggers, Romesberg and Schultz in 2000.[31] To do this they first prepared an artificial base pair by using the planar tridentate pyridine-2,6-dicarboxylate (Dipic) and a complementary single donor ligand in pyridine (Py). The

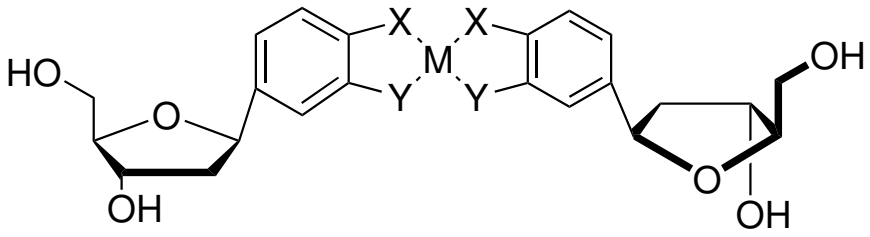

Figure 1.5: The general structure Tanaka's group used when preparing artificial bases.
1: X = Y = NH_2, M = Pd^{2+}.[28]
2: X = O^-, Y = NH_2, M = Pd^{2+}.[29]
3: X = Y = O^-, M = Cu^{2+}.[30]

[3+1] coordination was chosen due to the higher affinity for metal ion bonding compared to that of the [2+2] and natural nucleobases. By then integrating this into duplex DNA they were then able to add Cu^{2+} ions into the double strand. What they found was that without the coordinated metal the artificial bases caused a destabilising effect on the double strand with the melting temperature decreasing by around 27 $^{\circ}\mathrm{C}$ to around 14 $^{\circ}\mathrm{C}$. However when the metal was added this temperature increased to 38.6 $^{\circ}\mathrm{C}$ showing that binding is taking place between the Dipic and Py which was then confirmed using electron paramagnetic resonance.

All the examples above show charge transport however there are few examples of metallic conduction being found in mDNA which could be down to the ions being inserted into the base pairs. In the case of Aich for example, Zn^{2+} has no valence electrons so the main reason why metals have such good electrical conduction has been removed. They found that when a donor and acceptor fluorophore are present at opposite ends of a 20 base pair M-DNA duplex the fluorescence of the donor was quenched but only when the acceptor was present. This shows that charge transfer can still be facilitated due to the empty 4s orbital in which electrons can hop between. Due to this, an alternative modification has been used which is DNA templating. This has prompted an alternative modification to be investigated, which is DNA templating.

DNA Templating

The next modification possible with DNA is to use the strand as a template to which metal or semiconducting materials can be grown on. This occurs due to the attraction be-

tween the positive ion and the negative phosphate backbone of DNA as well as coordination bonding to the bases. When a slightly soluble material is used such as cadmium sulphide it can dissolve and re-precipitate on the bare DNA between the particles in a process that is analogous to Ostwald ripening. This is driven by both the surface energy and the energy of adhesion to the DNA template meaning under the correct conditions the smooth nanowire formation has the lowest free energy. This process can be found in figure 1.6. It is important that the metal cations are added to the DNA first as they need to bind to the phosphate backbone before reacting with the added anion. If the order was switched then the anions would not bind to the DNA and metal sulfide would be formed in solution.

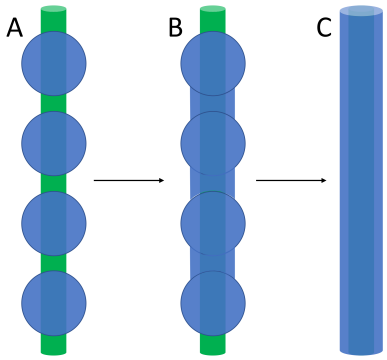

Figure 1.6: A diagram showing the 3 main stages of preparing a nanowire using DNA as a template. The DNA template is shown as a green cylinder and the templated material as blue. (A) Spherical nuclei form on the template via reduction or precipitation of metal ions. (B) 'Necks' form between particles due to material being transferred to bare areas of the template material. (C) When under equilibrium a smooth nanowire is formed.[4]

The reactions involved with this are as follows:

For metals an electroless reduction takes place:

$$M^{+} + Red- > M(s) + Ox \tag{1.1}$$

For binary semiconductors a precipitation reaction takes place:

$$M^{2+} + HS^{-}- > MS + H^{+} \tag{1.2}$$

This was first achieved by Braun *et al* in 1998 in which a DNA strand was stretched between two gold electrodes on which Ag^{+} ions were deposited and developed using hydroquinone and the process can be found in figure 1.7.[32] The IV measurements recorded

for the structure showed resistance values up to an order of 10^6 Ω, which is lower than for unmodified DNA measured in the same way. Since this report, much attention has been put into templating onto DNA with not only silver being used but gold,[33,34] copper,[35,36] conductive polymers[37,38] and compounds.[39–41]

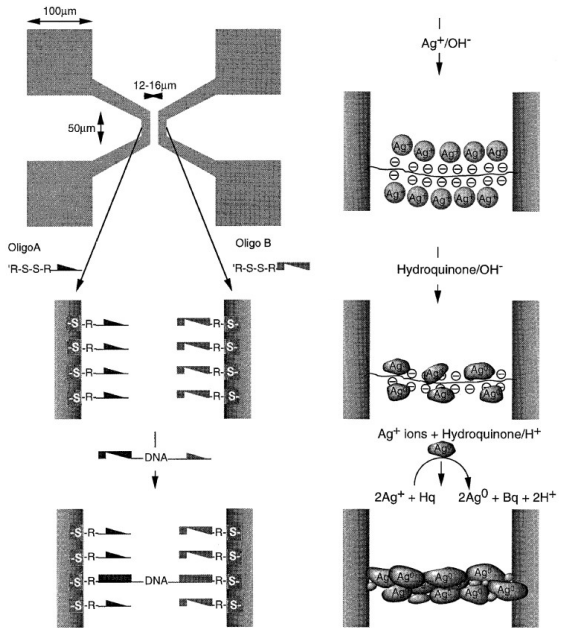

Figure 1.7: A figure showing the steps involved to prepare the first DNA templated nanowire by Braun.[32]

As research moves forward more novel methods are being used involving both DNA origami and carbon nanotubes (CNT). DNA origami was first shown by Rothemund in 2006 in which he showed desired shapes could be produced using DNA as a scaffold with some examples shown in figure 1.3.[21] This has since been used to act as a scaffolding template to insert metals into DNA with a good example of this is the report of Bayrak *et al*. They assembled a DNA mould in which the metal could be deposited in the hopes that it would create a more uniform wire owing to an increased ability to control the size of the metal particles.[42] To do this they used two layers of 10 parallel DNA helices in which they preloaded with DNA-functionalised gold nanoparticles and from which the wire could grow. What they found was that highly the moulds created highly conductive nanowires with current values up to 3 orders of magnitude greater than normal templating methods.

One of the first methods used to wrap carbon nanotubes in DNA was presented by Zheng et al in 2003 in which they sonicated HiPco CNT in aqueous DNA whilst being kept in a ice-water bath.[43] Figure 1.8 below shows the computational model of DNA wrapped

CNTs and the AFM image recorded of the prepared DNA wrapped CNTs.

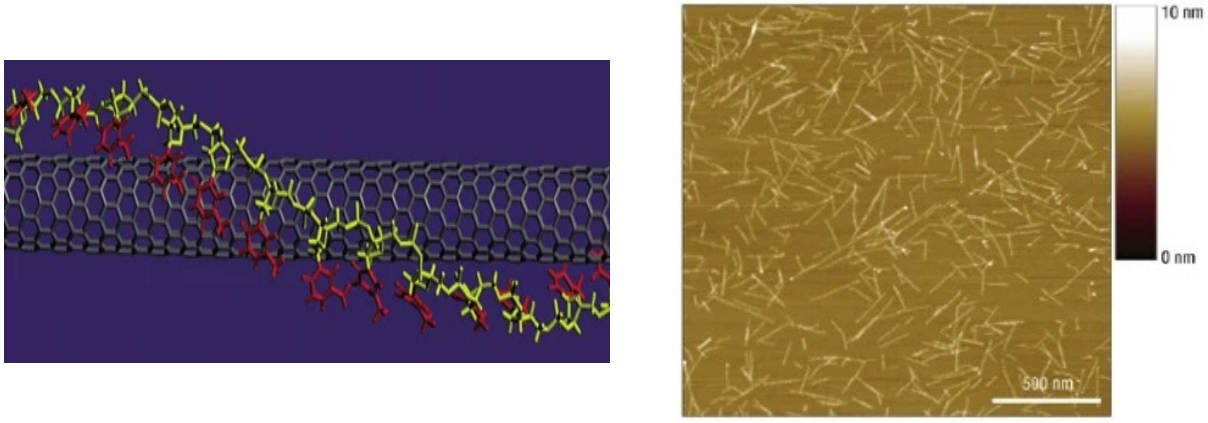

Figure 1.8: The computational model shown by Zheng for how DNA wraps around a CNT is shown on the left. The right image shows a recorded AFM image of the wrapped CNTs.[43]

CNT-DNA can then itself be used as a template for the nucleation and growth of materials such as cadmium sulphide and lead sulphide as found by Ye *et al*.[44] In this work single walled CNTs were first wrapped with ssDNA followed by the addition of either Pb^{2+} or Cd^{2+} and then HS^{-} to create PbS / CdS-DNA-CNT hybrids in order to create solution-processable photoresponsive devices. Interestingly, they found a difference in the photoresponse between the two hybrids in which PbS-DNA-CNT showed increased current within once second once illuminated where as CdS-DNA-CNT showed the opposite behaviour with the current decreasing. Other inorganic materials can also be templated using DNA origami as shown by Liu *et al* in which they prepared DNA-silica hybrids in order to overcome the surface charging of DNA that can inhibit material deposition.[45] Normal DNA-origami requires a high concentration of cations to help maintain their structural integrity however this high ion strength prevents the attaching of the molecules required for silicification. Liu developed a pre-hydrolysis step which hydrolysed thymine within the DNA, allowing silica deposition to occur. Using this method they were able to prepare silica templated structures with nanometre resolution as seen below in figure 1.9.

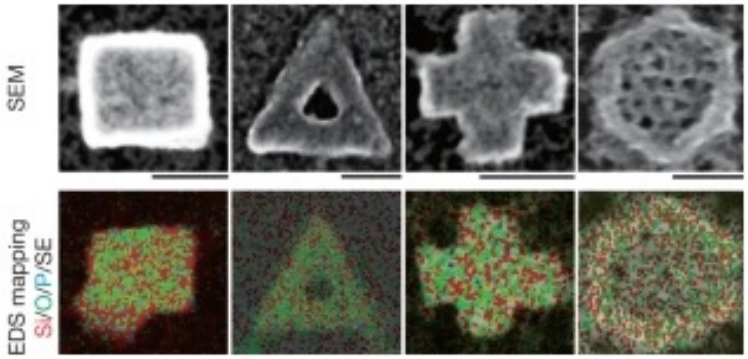

Figure 1.9: An example of some of the shapes created by Liu. The EDS mapping shows the silica molecules in red.[45]

It is also possible to combine DNA origami with CNT templating in order to add CNTs to DNA at specific sites as shown by Maune *et al*.[46] In this work, single walled CNTs were aligned along single stranded DNA which had complementary 'hooks' that then allows CNTs with different properties to be labelled. After labelling the CNTs can self assemble in a geometry defined by DNA origami therefore allowing multiple populations of CNTs to be simultaneously positioned and aligned based on the sequence of the DNA linkers.

1.3 Molecular Combing

Molecular combing is a technique used to analyse and map long stretches of DNA molecules in which individual DNA strands are stretched and aligned over a glass surface.[47] The first examples of molecular combing were released in 1994 by Bensimon *et al* and worked by creating a silane layer on a glass cover slip to which DNA can bind. After a drop of DNA was added to the silanated cover slip an untreated cover slip was floated on the top, making the film spread out to a desired thickness.[48] Since then, varying methods have been produced such as using a motor to pull the cover slip to keep a constant speed or by using a pipette to suck up the DNA droplet.[49,50] The main advantages of molecular combing are that all of the molecules are stretched uniformly across the surface of the cover slip and that a large number of molecules can be combed during a single process, allowing large sets of data to be collected at once.[51] One of the main disadvantages however is the risk of mechanically shearing the DNA during the manipulation meaning that the combing process must start over.[52] The main area molecular combing is utilised is genomic studying

where originally chromosomal DNA molecules and genetic rearrangements were studied.[53]

Molecular combing can also be used to align templated materials such as CdS-DNA as found in the work by Watson *et al* in which molecular combing was used to align a CdS-DNA nanowire between two electrodes, as shown below in figure 1.10, in order to directly measure the IV of a single wire.[4]

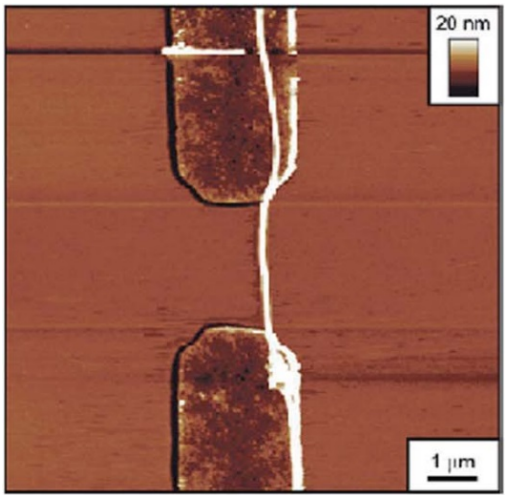

Figure 1.10: A CdS-DNA nanowire stretched between two electrodes using molecular combing in the work done by Watson.[4]

1.4 Cadmium Sulphide

Cadmium sulfide (CdS) is a II-VI semiconductor compound with remarkable optical and electronic properties that make it a highly researched material in optoelectronics, sensors, and photocatalysis. CdS exists as a direct bandgap semiconductor, with a bandgap of approximately 2.42 eV at room temperature, enabling strong absorption in the visible range.[54] In the past few decades, CdS nanostructures, including nanowires, have drawn significant interest due to the quantum confinement effects that alter their optical and electronic properties, making them attractive for applications like solar cells and photodetectors.[55–57] This work focuses on CdS nanowires prepared by a templating reaction on DNA however there are two other ways in which CdS nanowires can be prepared: Vapour-liquid-solid (VLS) and solution based method such as hydrothermal and solvothermal.[58–61]

There are currently no examples of CdS-DNA transistors however CdS has been used to create working transistors as nanoribbons in work completed by Duan.[62] CdS nanorib-

bons were prepared by vacuum vapour transport before being dispersed in ethanol and deposited onto a globally back gated device. They found electron mobilities of 200 - 300 cm^2/V.s which is comparable to the bulk material. Ma *et al* successfully created a metal-semiconductor field effect transistor using a single CdS nanowire that showed an on/off current ratio of 5x10^3 using UV lithography.[63] A more common application for CdS nanowires are in photodetectors due to the high refraction index and transport properties.[64] A good example of this was shown by Heo *et al* in which a flexible ohmic contact photodetector was prepared using CdS nanowires. The nanowires were prepared using the VLS method before being functionalized with a carboxylic acid and aligned using an amine terminated regions patterned on a Al_2O_3 substrate. The final photodetectors showed IV measurements of 10 nA at 2 V plus 10 times photosensitivity and a 100 times faster photoresponse when compared to non-aligned nanowire detectors.[65]

1.5 Vanadium Dioxide

Vanadium dioxide (VO_2) is a transition metal oxide that has gained substantial interest due to its interesting properties with the most notable being a metal to insulator transition temperature around 68 $^{\circ}\mathrm{C}$ in which a change in the crystal structure occurs from monoclinic to rutile.[66–68] Vanadium dioxide can exist in many different polymorphic phases including (B), (M), (R) and (D) with the (M) and (B) phases being the most researched.[69] Vanadium oxides usually exhibit n-type behaviour however for the (B) phase, it has been found that it has shown abnormal p-type properties.[70] There are currently no examples of DNA templated VO_2 as this is a new concept however it has been shown that VO_2 thin films can be modulated by a traditional gate.[71–73] Zhang *et al* have fabricated a ferro field effect transistor using VO_2 nanowires.[74] VO_2 nanowires were grown via chemical vapour deposition on a SiO_2/Si substrate before being laid onto a PZT thin film which had been deposited on Nb-doped $SrTiO_3$ as shown in figure 1.11. They found that the nanowire channel increases from 0.2 $\mu\mathrm{A}$ to 1.2 $\mu\mathrm{A}$ when the gate voltage increases from 0 to 18 V with the resistance decreasing by an order of magnitude.

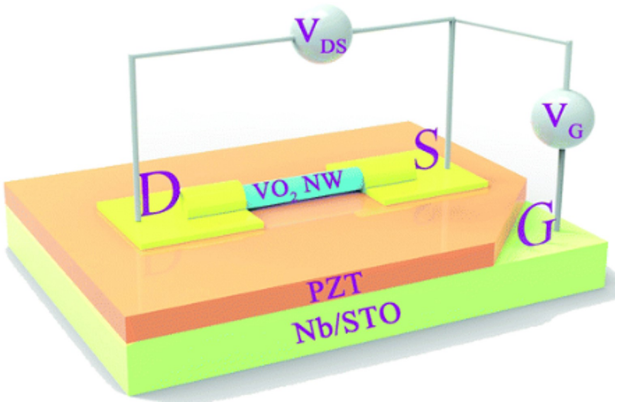

Figure 1.11: The FeFET design used by Zhang to create a 3 terminal VO_2 device.[74]

1.5.1 Vanadium Oxide (B) Phase

VO_2 (B) is a semiconducting metastable polymorph of VO_2 that forms during soft-chemical synthesis.[75] The main application for VO_2 (B) is as a promising cathode material for lithium ion batteries due to both its electrode potential and tunnel structure.[76–78] Recent studies have been working on altering the morphology of VO_2 (B) nanomaterials to create nanorods, nanotubes and nanowires.[79–81] Figure 1.12 shows the C2/m crystal structure of VO_2-B that was discovered by Oka and then drawn by Corr with the larger spheres representing vanadium and the smaller representing oxygen.[82,83]

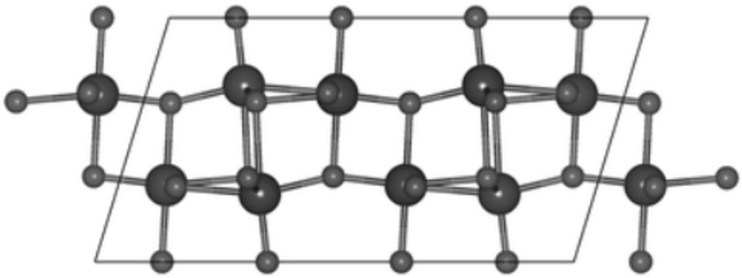

Figure 1.12: The crystal structure of VO_2 (B) as discovered by Oka[82] and then drawn by Corr.[83] VO_2 adopts a monoclinic structure C2/m.

1.5.2 Vanadium Oxide (M) - (R) Phase

The metal to insulator transition (MIT) at around 68 °C mentioned above is found during the transition from the (M) to the (R) phase and was first discovered in 1959.[84] One of the main mechanisms that has been suggested to explain this transition is the Peierls

model. The Peierls model describes a structural change within the crystal structure due to the vanadium atoms transitioning from a shared d-orbital to a localized d-orbital in the V-V dimer which causes the new bond lengths as found in figure 1.13.[85] Further research is now looking at manipulating the MIT of VO_2 through the use of external stimuli including an external field, optical stimulation and electrochemical reactions.[86–90]

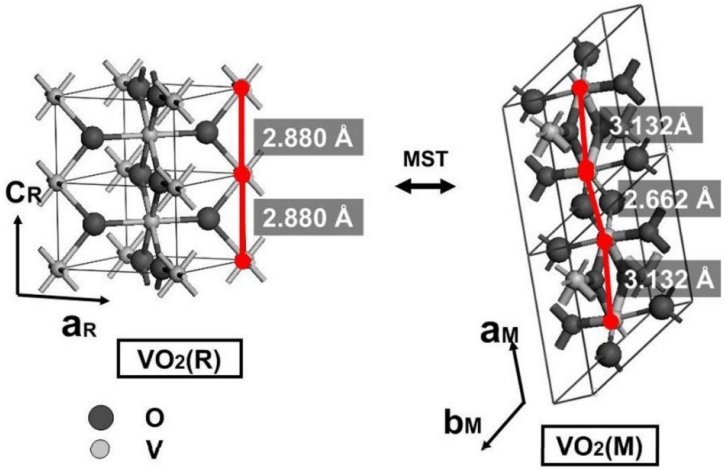

Figure 1.13: The structure of VO_2 (R) and VO_2 (M) as published by Li.[91] After the metal to ligand transition the 2.88 Å V-V chains along the C_R axis become distorted to a monoclinic structure with alternating lengths of 3.132 Å and 2.662 Å.

One of the main potential applications for VO_2 (M) is the integration into electrical switches and field effect transistors (FETs) as it is possible to deliberately trigger the MIT.

1.6 Carbon Nanotubes

Carbon nanotubes (CNT) are tubes made up of sp^2 hybridized carbons with diameters ranging from around 1 - 50 nm and were first discovered in 1991 by the research group led by Iijima.[92] They can be described as graphene sheets that have been rolled up into cylinders and are considered derivatives of both carbon fibres and fullerenes. They can be synthesised using three methods: arc discharge, laser ablation and chemical vapour deposition.[93]

There are two main types of CNT structures, singled-walled CNT (SWCNT) and multi-walled carbon nanotubes (MWCNT). The difference between the two is that SWCNTs are made up of only a single graphene layer compared to MWCNTs which are made from

multiple layers of graphene as shown below in figure 1.14.

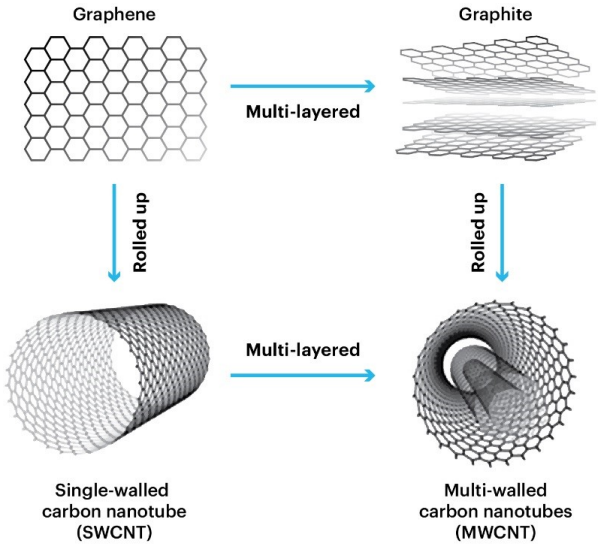

Figure 1.14: The process in which CNTs form. When one graphene sheet is present then a SWCNT is formed compared to multiple graphene sheets which proceed to form MWCNTs.[94]

Although the two structures look similar to one another the physical properties alter significantly from each other as seen in table 1.1:

Property	SWCNTs	MWCNTs
Diameter (nm)	1 - 2	7 - 100
Length (mm)	Up to 1 mm	Up to 1 mm
Aspect ratio	Up to 10000	50 - 4000
Elastic modulus (GPa)	1000 - 3000	300 - 1000
Tensile Strength $(\mathrm{GPa}$	50 - 100	10 - 50
Thermal Conductivity at 300 K $(\mathrm{W/m\,K})$	3000 - 6000	2000 - 3000

Table 1.1: A table comparing some of the properties between SWCNTs and MWCNTs.

The electrical properties of CNTs are dictated by the sheet pattern of the graphite sheet and the subsequent rolling up of this sheet which produces CNTs with differing chirality.

The chiral vector (C_h) is a vector that connects the centre of two hexagons and can be specified by the chiral index (n,m) using vectors a_1 and a_2 of a graphene sheet which is shown in figure 1.15.

$$C_h = na_1 + ma_2 \tag{1.3}$$

There are three distinct ways in which the graphite sheets can be rolled up and the integer pair (n,m) are used to classify the type of CNT formed. When n = m an armchair configuration is formed, for m = 0 zigzag CNTs are produced and for all other combinations chiral CNTs are created.[95] In general all armchair CNTs are metallic, tubes in which n - m = 3j where j is a non zero integer, are tiny-gap semiconductors and all others are large-gap semiconductors.[96]

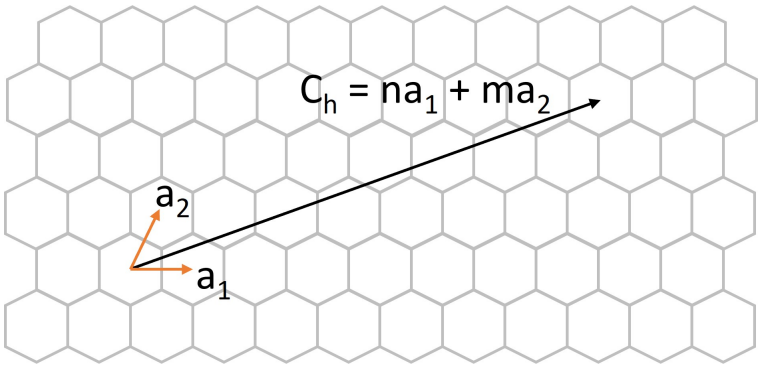

Figure 1.15: The chiral vector C can be specified by the use of the vectors a_1 and a_2 to to calculate the chiral index (n,m) of a graphene sheet.

In 2003 Braun's group reported a self assembling SWNT field effect transistor using DNA as a scaffold. The SWCNTs were coated in the protein streptavidin in which they were then attached to double stranded DNA using complementary antibodies. Silver was then templated to the DNA to make a highly conductive wire before electroless gold plating was used to create contact points. Overall using this method 14 devices out of the 45 created were functional FETs.[97] An interesting method to create a CNT-FET was completed by Zhao *et al* in which they wrapped CNTs in sacrificial DNA which is used for alignment purposes.[98] To do this they applied a DNA-CNT solution to a PMMA coated Si wafer that had been patterned with grooves that the solution could diffuse into. Once the DNA-CNT were in the correct place, the DNA was removed from the CNTs, by thermal decomposition at 400 $^{\circ}$C, to leave a highly organised system of CNTs remaining on the Si wafer. Using this

method, 63 % of devices showed typical gate modulation with a current density exceeding 10^3. A similar and more recent method is utilised by Chen *et al* however instead of a PMMA film to produce the trenches, DNA bricks are used to create trenches to which ssDNA wrapped CNTs are then added which assemble within the nanotrenches before the DNA is removed by H_2O_2.[99]

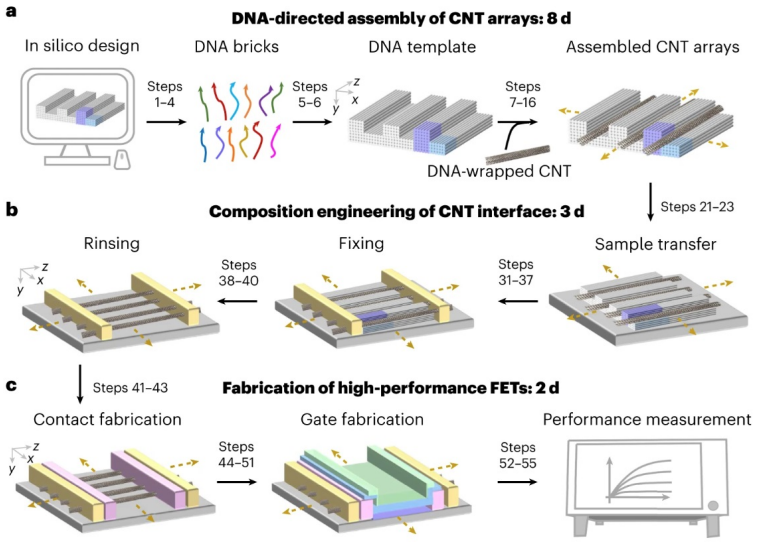

Figure 1.16: A schematic showing the fabrication process for the CNT-FET device prepared by chen.[99]

1.7 Charge Transport

Charge transport in semiconductors is a complex phenomenon that can be understood through various models and concepts including the two discussed below, band transport and hopping.

1.7.1 Band Transport

Band Theory of Solids

Band theory is a key concept in solid-state physics that explains the behaviour of electrons in a solid material. It describes how atomic orbitals combine to form energy bands and how these bands determine the electrical properties of solids. In isolated atoms, electrons occupy discrete energy levels which are quantized and are described by the solutions to the Schrödinger equation. In a solid material, the proximity of atoms means that the

electron wavefunctions can overlap. This overlap causes the discrete energy levels found in individual atoms to broaden and form continuous energy bands, of whoch the valence and conduction band are the most relevant tp understanding the electronic conductivity. The valence band is the highest range of electron energy where electrons are present at absolute zero and are loosely bound to the nucleus of the atom. The conduction band is the band above the valence band (unoccupied at T = 0K). Electrons promoted to the conduction band are free to move as seen in figure 1.17. If the bandgap is greater than the thermal energy, an external energy source is required to move electrons from the valence to conduction band.

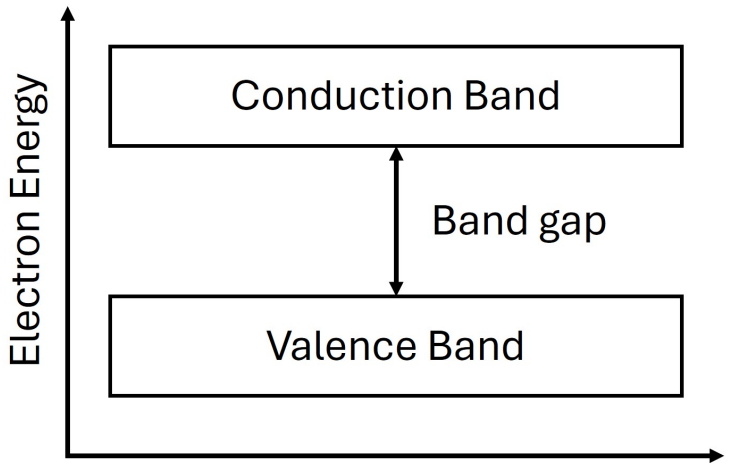

Figure 1.17: A basic band gap diagram showing the respective energies of both the valence and conduction bands along with the band gap energy.

Between the valence and conduction bands is an energy gap which can vary is size. The size of the energy gap can help classify the material as either a conductor, a semiconductor or an insulator as seen in figure 1.18. When the valence and conductance band overlap, electrons are always free to move and conduct therefore these materials are classed as metals. On the other hand, when the band gap is large, very few electrons can move to the conduction band. Those in the filled valence band do not contribute to the conductivity because of the Pauli exclusion principle and therefore these materials are classed as insulators. The distinction between insulators and semiconductors is a matter of degree. Typically materials with band gaps less than about 3 eV are referred to as semiconductors, but this is not a rigid definition. Finally, when there is a small band gap, electrons are able to move up to the conduction band if their energy is raised externally such as a potential

being applied. Samples can also be doped with impurities which may be easily ionised to add electrons to the conduction band (donors) or may capture electrons from the valence band (acceptors) to create holes in the filled band that behave as positive charge carriers. Semiconductors that have been doped are called extrinsic and those that have a pure crystal structure are intrinsic. Figure 1.18 also shows the fermi level, this being the highest energy level occupied by electrons at absolute zero. In a conductor, the fermi level is at an energy within one of the bands. In both semiconductors and insulators the fermi level lies within the band gap. However in a semiconductor, the level may be close to one of the bands. In the case of an n-type semiconductor where the donor impurities provide electrons in the conduction band, the fermi level is close to the bottom of the conduction band. For a p-type semiconductor where the charge carriers are holes in the valence band, the fermi level is close to the top of the valence band.

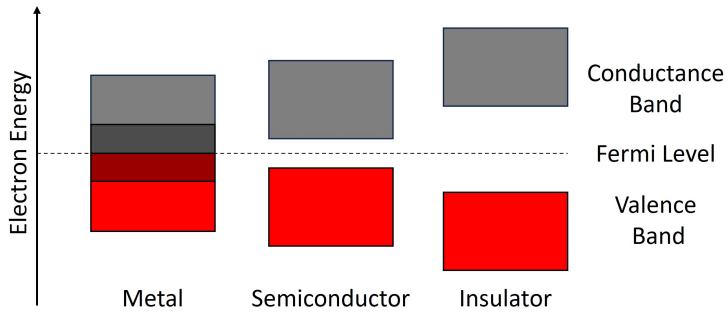

Figure 1.18: A diagram showing the difference in band gaps between a metal, a semiconductor and an insulator.

Electronic Wavefunctions in Crystalline Solids

One of the fundamental models that describes electrical, thermal and optical properties within metals is the free electron model which was first developed by Arnold Sommerfield in 1927.[100] In this model, the valence electrons are not bound to the ion cores and considered to travel freely throughout the solid. For example in Na, the 3s valence electron is free and the remaining core electrons are bound to the atomic nucleus, forming the ion core, Na^+. In the free and independent electron model, the valence electrons are assumed not to interact with the potential of the lattice of ion cores (free) or with each other (independent). The only effect of the ion cores is to maintain electroneutrality. As a result, only the kinetic energy of the electrons is included in the Schrödinger equation, which may be

written for time-independent states as,

$$H\psi(x) = \frac{p^2}{2m}\psi(x) = -\frac{\hbar^2}{2m}\left(\frac{d^2}{dx^2} + \frac{d^2}{dy^2} + \frac{d^2}{dz^2}\right)\psi(x) = E\psi(x). \tag{1.4}$$

The wavefunction is simply,

$$\psi(x) = e^{ik.r}, \tag{1.5}$$

where r is a vector with components x, y and z and $k.r$ means the dot product. The energy is

$$E = \frac{\hbar^2 k^2}{2m}. \tag{1.6}$$

Each level is associated with a wavevector k and a momentum $p = \hbar k$. Clearly the free electron model is a drastic simplification which does not allow for the existence of any bandgap. The origin of the gap is the scattering of electrons from the periodic potential of the ion cores. However, the Bloch theorem shows that the wavefunctions of electrons in a periodic potential can be written as the product of a plane wave and a function that has the same periodicity as the lattice. Mathematically, the Bloch wavefunction ($\psi_k(r)$) takes the form:

$$\psi_{n,k}(r) = e^{ik.r}u_{n,k}(r) \tag{1.7}$$

in which $\hbar k$ is the crystal momentum associated with the electron and n is an index that denotes a particular band. The factor $e^{ik.r}$ is a plane wave which describes the free particle-like motion of the electron and $u_{n,k}(r)$ is a periodic function that has the same periodicity as the crystal lattice:

$$u_{n,k}(r) = u_{n,k}(r + R) \tag{1.8}$$

where R is any lattice vector. $u_{n,k}(r)$ accounts for the effect of the periodic potential - the electrons are now being treated as independent, but not free. Nevertheless, the energy of an electron may still approximately obey a free-electron like relation, especially near the bottom of the conduction band.

$$E_n(k) = \frac{\hbar^2 k^2}{2m^*} \tag{1.9}$$

In equation (1.9) the energy is measured with respect to the bottom of the band n and m^* is an effective mass which incorporates the effect of the periodic potential on the electron motion. This effective mass (m^*) can be used in place of the free electron mass to assess how the electron responds to external forces such as an electric field.

Drude Model of Transport

The Drude model was first proposed in 1900 by Paul Drude in order to explain the transport properties of electrons in metals.[101] Drudes model attempted to use the idea of a gas cloud of electrons which were free to move between positively charged ionic cores and there were 5 assumptions:

- A collision indicates the scattering of an electron
- Between collisions, electrons do not interact with each other or with ions
- Collisions are instantaneous and result in a randomisation of velocity such that the average momentum after a collision is zero
- an electron suffers a collision with a probability per unit time τ^{-1}, this is known as the relaxation time
- Electrons achieve thermal equilibrium with the surroundings only through collisions

When considering the motion of an electron with the momentum p and at a time t, two effects determine the momentum at $t + dt$. There is the probability that the electron will scatter to zero momentum ($\frac{dt}{\tau}$) and then if it does not scatter, it will accelerate according to the equation of motion $\frac{dp}{dt} = F$.[102] When the two terms are put together, equation 1.10 is obtained:

$$\frac{dp}{dt} = F - \frac{p}{\tau} \tag{1.10}$$

In an electric field the equation of motion becomes:

$$\frac{dp}{dt} = -eE - \frac{p}{\tau} \tag{1.11}$$

in which E is the applied electric field. The effect of the collisions is seen to be a term $-\frac{p}{\tau}$ which opposes the acceleration in the field, i.e., a drag force. When the electron is in a steady state, $\frac{dp}{dt} = 0$ in which case:

$$m^* v = p = -e\tau E \tag{1.12}$$

where m^* is the effective mass of the electron and v it's velocity. If there is a density (n) of electrons within a metal, all with a charge of -e whilst moving at a velocity (v), the electrical current density j can be calculate by equation 1.13:

$$j = -env = \frac{e^2 \tau n}{m} E \tag{1.13}$$

By substituting j for σE (Ohm's law), the conductivity of a metal can be given by:

$$\sigma = \frac{e^2 \tau n}{m} \tag{1.14}$$

Based on measured conductivities and valence electron densities, τ is of the order of 10^{-14} s. Simple collision with ion cores would give values that are much smaller and the effect of scattering from the ion cores is already taken into account in the factor $u_{n,k}(r)$.[102] Although the Drude model did not provide a satisfactory mechanism for the collisions, a consideration of the mechanism of scattering provides an understanding of the temperature dependence of conductivity in metallic conductors.

Electrical Resistance in Metals

Simply put electrical resistance is the opposition a material offers to the flow of electric current. When a voltage is applied across a metal conductor, electrons move, creating an electric current. However, their movement isn't smooth; they collide with atoms and other electrons in the material, impeding their flow, which manifests as resistance. Resistance is related to both the materials dimensions and resistivity:

$$R = \rho \frac{L}{A} \tag{1.15}$$

in which R is the resistance, ρ is the resistivity, L is the length of the conductor and A is the cross-sectional area.

Metals are composed of a lattice of positively charged ions surrounded by free electrons as mentioned before in section 1.7.1 and it is these free electrons which move in response to an electric field. When the electrons are moving, they can be interrupted by multiple scattering events with the main one being phonon scattering. At non-zero temperatures, the ion cores vibrate around their fixed positions giving rise to waves, the quanta of which are called phonons. Electrons can collide with phonons causing the electrons to scatter and lose momentum, this then results in an increase in resistance. Less influential scattering events include impurity scattering in which impurities within the metal can disrupt the regular arrangement of the lattice and defect scattering where dislocations and irregularities form within the lattice such as vacancies or grain boundaries. One main difference between the three is that phonon scattering is temperature dependent, where as the other two are not. The mean free path of an electron is the average distance in which it can travel between collisions meaning that the longer the mean free path, the fewer collisions experience by an electron and the lower the resistance.

Resistance in metals typically increases as the temperature does due to the higher energy and density of phonons leading to more frequent collisions between phonons and electrons. This means that the mean free path of the electron also changes with temperature. At lower temperatures with minimal scattering, the mean free path can approach the size of the metal sample, known as the ballistic regime. At higher temperature though, the interactions with phonons increases meaning a decrease in the mean free path. The typical metallic relationship between resistance and temperature at temperatures of the order of ambient and above can be expressed as:

$$R(T) = R_0[1 + \alpha(T - T_0)] \tag{1.16}$$

in which R(T) is the resistance at temperature T, R_0 is the resistance at a reference temperature, α is the temperature coefficient of resistance and T_0 is the reference temperature. For metals, the temperature coefficient is positive, meaning that as the temperature rises, so to does the resistance.

Conduction in Intrinsic Semiconductors

Intrinsic semiconductors are pure semiconductor materials where the electrical properties are determined solely by the material itself, without the influence of impurities or external doping. The two most common intrinsic semiconductors are silicon (Si) and germanium (Ge). When an electron gains enough energy to move to the conduction band it leaves behind a positively charged hole. Both the free electron in the conduction band and the positively charged hole contribute to the electric conduction. In intrinsic semiconductors, the number of free electrons in the conduction band (n_i) is always equal to the number of holes in the valence band (p_i), because every electron that is excited to the conduction band leaves behind a corresponding hole. At thermal equilibrium, the rate at which electron-hole pairs are generated is equal to the rate at which they recombine. Recombination occurs when an electron from the conduction band loses energy and falls back into a hole in the valence band.

The intrinsic carrier concentration at thermal equilibrium is given by the equation:

$$n_i p_i = n_i^2 = K e^{-\frac{E_g}{k_B T}} \tag{1.17}$$

In which K is a material dependent constant, E_g is the band gap, k_B is the Boltzmann constant and T is the temperature. As equation 1.18 shows, as the temperature is increased the density of carriers present within an intrinsic semiconducting material increases exponentially. The same phonon interactions mentioned above are also present within semiconductors however this effect is weaker than the exponential increase in charge carriers. The result is a conductivity whose value is proportional to the carrier concentration.

$$\sigma \propto n_i = \sqrt{K} e^{-\frac{E_g}{2k_B T}} \tag{1.18}$$

Conduction in Extrinsic Semiconductors

Extrinsic semiconductors are semiconductors whose electrical properties have been modified through the deliberate introduction of impurities, a process known as doping. Doping adds additional charge carriers—either electrons or holes—depending on the type of impurity added, which significantly enhances the conductivity of the semiconductor.

There are two types of extrinsic semiconductor depending on the nature of the dopant; n-type in which additional electrons are added into the system and p-type in which additional holes are introduced into the system as seen in figure 1.19.

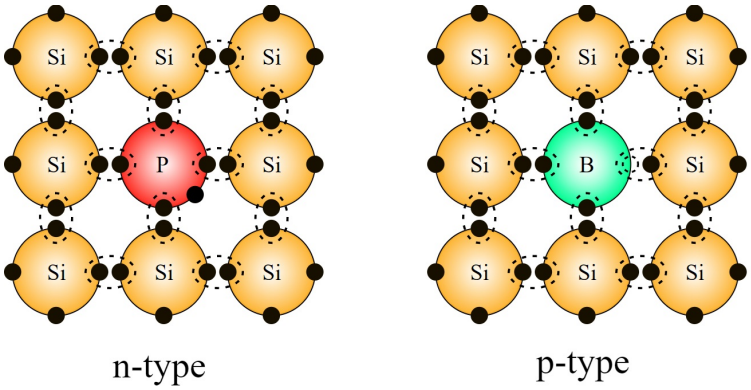

Figure 1.19: A diagram showing the main difference between n-type and p-type doping in semiconductors. In n-type, the dopant adds an electron whereas in p-type, a hole is introduced.[103]

The dopant in n-type Si are typically pentavalent atoms such as phosphorous (P), arsenic (As) and antimony (Sb) because when a pentavalent atom replaces a tetravalent atom such as silicon, the fifth electron is only weakly bound to the dopant atom. This means the electron requires little energy to be excited to the conduction band therefore the band gap decreases. Due to this, electrons are the majority carriers within n-type semiconductors as they outnumber the thermally generated holes within the valence band.

Conversely, the dopant in p-type Si are typically trivalent atoms such as boron (B), gallium (Ga) and indium (In) which introduce additional holes into the semiconducting material. When a trivalent atom is added to a semiconducting material, only three of the neighbouring four silicon atoms can form a bond which then creates a hole which can then act as an electron acceptor. This means that holes are the majority carrier within p-type semiconductors.

The conductivity of extrinsic semiconductors increases as the temperature rises due to the points mentioned earlier however the behaviour differs when compared to intrinsic semiconductors. At low temperatures, n-type semiconductors act as insulators due to the thermal energy being insufficient to excite electrons to the conduction band. As the temperature increases, the conductivity is determined by the carrier concentration of the dopant due to the lower thermal energy required to excite the donor electrons and holes. Finally at

high temperatures, the thermal energy is large enough that electrons in the valence band can be excited to the conduction band and the behaviour is more like that of an intrinsic semiconductor. This occurs when there is a high concentration of intrinsic electrons compared to dopant atoms.

1.7.2 Localized vs Delocalized Wavefunctions

There is a fundamental difference between localized and delocalized wavefunctions which impacts the behaviour of different materials. Localized wave functions describe a quantum state that is confined to a small region of space which has most of its amplitude concentrated within a a smaller spatial range and decays rapidly when outside of this region. Localized wavefunctions are most commonly found in disordered materials and charge carriers undergo hopping conduction between such localized sites. Delocalized wavefunctions on the other hand describe a state in which a particle is spread out over a larger region of space with a near uniform amplitude throughout the system. As described above, this is the case in crystalline solids, whether metallic or semiconducting.

1.7.3 Hopping Conduction

Hopping conduction is a mechanism of electrical conduction where charge carriers (usually electrons or holes) move between localized sites (such as atoms, molecules, or defects) normally through a quantum mechanical tunnelling process. It is more commonly found in disordered and amorphous semiconductors which often do not have well-delocalised electron wavefunctions. There are two main types of hopping conduction: nearest-neighbour hopping (NNH) and variable range hopping (VRH). NNH occurs when an electrons hops to the nearest localized site and is more prominent at higher temperatures.[104] At lower temperatures hopping is described by the Mott VRH model in which electrons can hop to further sites if the energy difference between the sites is small.[105]

Hopping conduction can also be described as thermally aided tunnelling from one localized electronic state to the neighbouring state. The probability of this occurring is dependent on the tunnelling distance and the energy of the barrier through which the particle must tunnel:

$$P = X \exp(-aR) \tag{1.19}$$

in which R is the distance. The factor a is dependent on both the energy of the barrier (U) as well as the energy of the particle that is tunnelling (E) so that:

$$a^2 = 2m_e \frac{U - E}{\hbar^2} \tag{1.20}$$

The rate of hopping is also dependent on the overall occupancy of localized sites to which an electron can hop to. In an ideal scenario there is one site occupied with an empty neighbour for the electron to hop to with no penalty. If both sites are occupied then it is still possible for hopping to occur however there is an energy penalty when two electrons occupy the same site. Finally, if neither site is occupied then no hopping can occur due to the lack of charge carriers.

Temperature dependence of hopping conductivity

Hopping conductors typically show a temperature-dependent conductivity which can be expressed by equation 1.21.

$$\sigma = \sigma_0 e^{-\left(\frac{\Delta E}{k_B T}\right)^{\beta}} \tag{1.21}$$

The parameter β is 1 for nearest-neighbour hopping and then an Arrhenius plot of $\ln G$ against $1/T$ will be a straight line of slope $-\frac{\Delta E}{k_B}$. This temperature-dependence has the same functional form as that of an intrinsic semiconductor where the underlying process is thermal excitation of electrons and holes across the bandgap E_g. If the bandgap can be established independently, e.g., by optical absorption spectra, then the slope of the Arrhenius plot will be $E_g/2k_B$, which provides a test to discriminate between hopping and a mechanism based on intrinsic semiconductivity.

In the case of variable range hopping $0 < \beta < 1$ and β depends on the dimensionality of the material. The weaker temperature dependence of VRH reflects the fact that, in 2D or 3D samples, the charges may take a variety of routes and therefore avoid the largest barriers. This form of temperature dependence is also observed in grannular metal, for which $\beta = 1/2$.[106]

Potential-dependence of conductivity

If the conductivity is independent of applied potential, then Ohm's law applies and a linear IV characteristic is obtained. Nonlinear IV characteristics are also frequently observed and some sources of these effects relevant to the measurements in later chapters are discussed here. The IV characteristic of a metal/semiconductor junction is typically of the form,

$$j = j_0 \left(e^{\frac{eV}{nk_BT}} - 1 \right), \tag{1.22}$$

which describes the asymmetric IV curve of a Schottky diode with current density j. In equation 1.22, j_0 is the reverse bias current density, V is the applied potential and n is the diode quality factor. However, the two-terminal devices in this work are of the form metal/nanowire/metal and therefore, even when the metal/nanowire interface is expected to behave in accordance with equation 1.22, the exponential rise of current with voltage is not expected because one of the interfaces will be reverse-biased. At low voltages, an approximately linear IV characteristic is expected, gradually reaching a plateau determined by the value of j_0 which expresses the potential-independent current density in reverse bias. In principle, a nonlinear IV characteristic could be observed at sufficiently high voltages to induce breakdown.

In the case of hopping conduction, a non-linear IV characteristic is also possible because the field drives electron transfer between sites.[107–109] This can be modelled by equation 1.23.

$$j = npk^{\ominus}(e^{\alpha\frac{deV}{LK_BT}} - e^{-(1-\alpha)\frac{deV}{LK_BT}}) \tag{1.23}$$

in which d is the site-site separation, V is the applied voltage, L is distance between the contacts, i.e. the sample length or thickness and n, p are the concentrations of occupied/unoccupied sites. The parameter $k^{\ominus}$ is a proportionality constant which determines the differential conductance at zero applied potential. α determines the symmetry of the IV characteristic. In the case $\alpha = 1/2$ the positive and negative branches of the IV curve are symmetrical. In the context of hopping conductivity of polymers or electron transfer at metal/molecular interfaces, α is known as the transfer coefficient or symmetry factor.

It is also related to the diode quality factor for metal/semiconductor interfaces. Finally, it is worth noting that if the current is limited by the kinetics of of electron transfer at the contacts, a similar exponential dependence on applied potential would be expected.

1.8 Transistors

Transistors are semiconducting devices that are used to either switch a circuit or amplify a signal and revolutionised the field of electronics allowing smaller and more powerful devices to be created. There are normally three terminals on a transistor: gate, source and drain in which the voltage on one effects the current through the other two. Figure 1.20 shows the different types of bipolar junction transistors (BJT) and metal-oxide semiconductor field effect transistor (MOSFET).

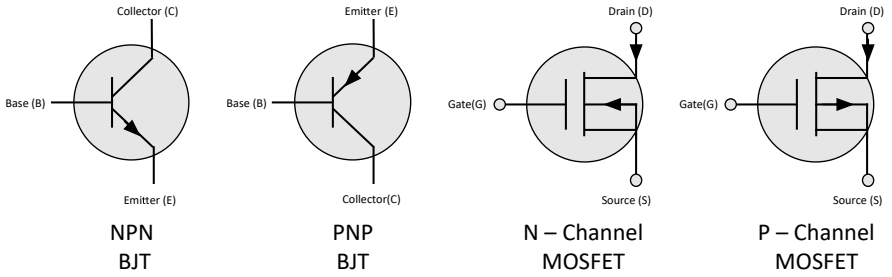

Figure 1.20: The electrical symbols for both types of BJTs and MOSFETs.

The majority of transistors are normally made from silicon however germanium has also been used. There are two main types of transistor, a bipolar junction and more commonly a metal-oxide semiconductor field effect transistor. The main aim of research into transistors is to both decrease the size and increase the efficiency to further enhance computing capabilities. A common guide to the decreasing size of transistors is Moore's Law in which the co-founder of Intel, Gordon Moore noticed that the number of transistors that can be present in a given area doubles every two years.[110] A visual representation of this is given in figure 1.21.

1.8.1 Bipolar Junction Transistors (BJT)

The BJT was invented in 1948 by William Shockley and was the main device used in integrated circuits for 30 years until the invention of the MOSFET. BJT's are three terminal

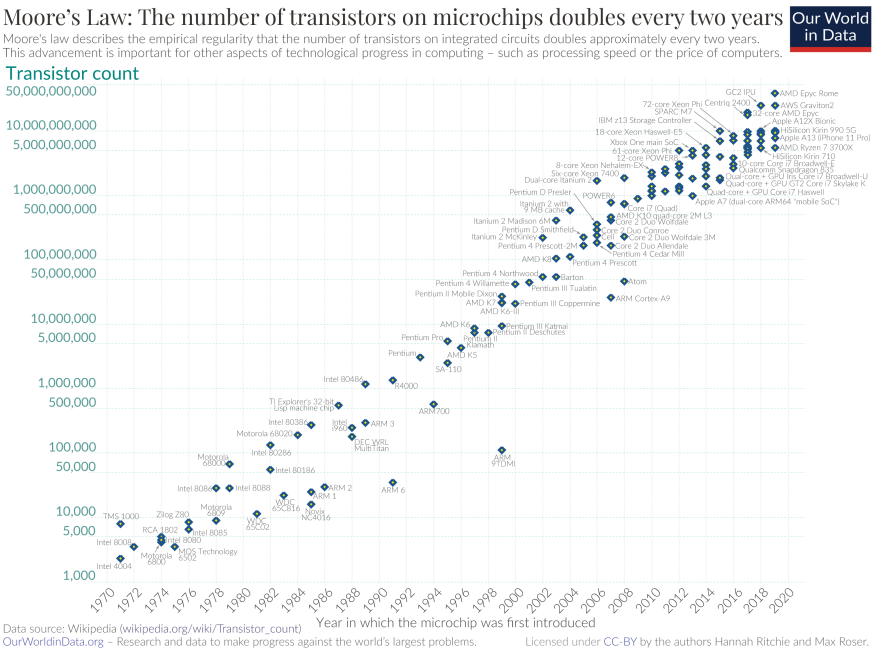

Figure 1.21: Moore's law predicted that the total number of transistors in a given area doubles every two years. This graph shows the transistor count on a given microchip and the year it was produced, proving Moore's law.[111]

devices which consist of 2 p-n junctions that can be controlled by a current in order to either amplify or magnify a signal.

Silicon is the material of choice for BJTs however doping is required to introduce semiconducting properties. Pure silicon has 4 valence electrons which can covalently bond to 4 other silicon atoms meaning there are no free electrons to travel. Doping involves adding other molecules in order to either add electrons or holes into the material. Boron has 3 valence electrons meaning a hole forms where the fourth silicon would have normally been present. This hole acts as an electron acceptor or p-type. Phosphorous has 5 valence electrons and when this is added to pure silicon the four atoms bond as they normally would, however there is also the fifth electron present that is now free to move and act as an electron donor or n-type. BJTs are then created by combining these doped materials in either NPN or PNP order to create three terminals: Base (B), Collector (C) and Emitter (E). Essentially this creates two back to back n-p or p-n diodes to which a voltage source is added between B and E as well as C and E as can be seen in figure 1.22. The BJT works in this example by forward biasing the emitter and base moiety meaning electrons can move into the p-doped region. The other diode is reverse biased meaning the electrons that moved to

the p-doped section are pulled to the positive side. To make this viable, the p-type region must be very thin and only lightly doped in order to reduce the amount of recombination as well as the number of electrons travelling around BE instead of CE.

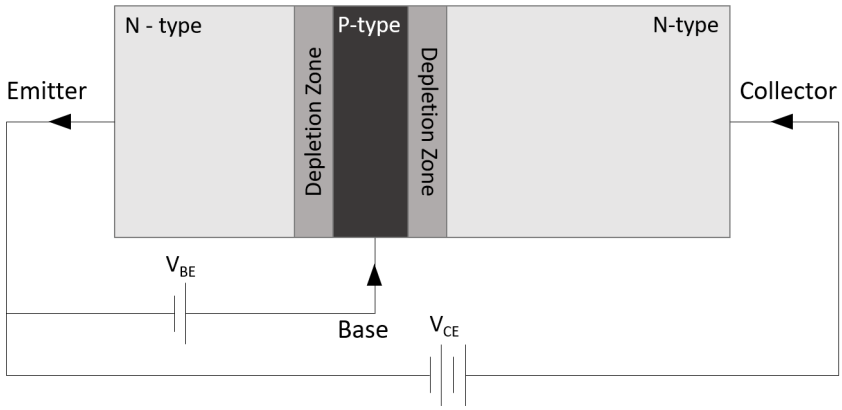

Figure 1.22: A schematic of a n-p-n bipolar junction transistor. Two back to back diodes are formed to which a voltage is applied between the base and emitter moieties so electrons can move into the p-doped region. The other diode is reverse biased so that the electrons within the p-doped region are pulled to the positive side.

1.8.2 Metal-Oxide Semiconductor Field Effect Transistors

The FET was first proposed by Julius Lilienfield in 1926 however it wasn't until 1959 that Mohammed Atalla invented the first working MOSFET which was presented in early 1960.[112] Since this original invention there has been emphasis researching how to reduce the size and the increase in overall efficiency of this device. Figure 1.23 shows a basic diagram of a standard MOSFET.

Similar to the BJT a MOSFET utilises semiconducting n- and p- doped silicon to create PN junctions. There are four main sections to a MOSFET: the gate, the insulating layer (gate dielectric), the source and drain and the semiconducting material. The gate is insulated from the source, drain and semiconducting material by a gate dielectric however it is important that the dielectric be sufficiently thin so that when a voltage is applied to the gate, the semiconductor can be effected by the electric field caused by the gate. The source and drain are normally made from a conductive material and are separated by the semiconducting material which can be either n or p type. When no voltage is being applied to the gate then the MOSFET is in an off state. A MOSFET operates by varying the applied voltage

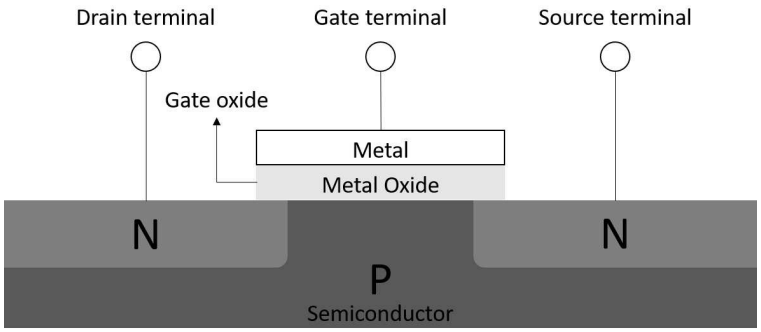

Figure 1.23: A schematic diagram of a typical N - channel MOSFET. Under the influence of a positive charge the holes in the p-type substrate are repelled leaving a negative depletion zone. This allows electrons to flow between the source and drain.

to the gate terminal to establish an electric field perpendicular to the channel region. When a positive charge is applied, the holes in a p-type substrate are repelled leaving an electron rich channel, also known as the inversion layer, in which charge can flow through when another voltage is applied between the source and drain. By altering the magnitude of the voltage applied to the gate, the width of the channel can be controlled to allow a higher or lower source to drain current. A shorter channel length is favoured within a MOSFET as the resistance is inversely proportional to the width:length ratio. There are three ways in which a MOSFET can be used depending on the voltages applied to both the gate and the source and drain. When the gate voltage is below the threshold voltage then a channel does not form and no drain current flows, this is known as the cutoff region. The triode region is when the gate voltage is above the threshold however the source to drain voltage is low and the FET behaves as a resistor. In this mode, the drain current increases linearly with the drain voltage. Finally when the gate voltage is above the threshold and the source to drain voltage is high, the drain current reaches its maximum and is classed as saturated (saturation region).

1.9 Device Fabrication Techniques

In order to fabricate the devices, clean room techniques were utilised in order to define the various circuit elements. The two main techniques were photolithography and e-beam deposition. When used in tandem, a pattern can be transferred onto a substrate before the required metal is deposited to create the desired features.

1.9.1 Photolithography - MJB-3 Mask Aligner

Mask alignment is a vital step in the preparation of integrated circuits as they are used to transfer the desired pattern from a photomask to the photoresist (PR) covered substrate. For this work the PR used is an image reversal photoresist (IPR) which result in a negative pattern of the mask. In image reversal photolithography the substrate is first exposed to UV light, using a mask to block out the required features and is followed by a hard bake. This hard bake is vital as during this, the exposed areas become both insoluble in developer and are no longer light sensitive due to a cross linking agent that is activated. The non-exposed areas however still act like a standard PR. After this, a flood exposure step then exposes the entire substrate causing the past non-exposed areas to become soluble and easily removed in a suitable developer. The instrument used for this was an MJB-3 Mask Aligner (later shown in figure 2.8). The exposure time and mode of exposure are controlled using the front panel. There are two modes of exposure: hard and soft contact. In hard contact mode purging nitrogen is used to push the substrate upwards, therefore reducing the gap to the mask and is used when a high level of resolution is required. Soft contact involves a vacuum holding the substrate in place and is used during flood exposure when no mask is present. The chuck is where the substrate is aligned using X, Y and Theta adjustment knobs before exposure is provided by a mercury lamp. A microscope is also present to assist with the alignment. Immersion liquids can be used for to further improve the resolution as the refractive index of these liquids matches that of the PR meaning any small gaps or impurities have a decreased effect. A more detailed explanation can be found later in section 2.4.2.

1.9.2 E-beam Deposition

The deposition of metal to create the contact points was achieved by using electron-beam physical vapour deposition (EBPVD). The first stage of the process is to evacuate the chamber that the deposition is taking place, down to around 4 x 10^{-6} mbar, using a diffusion pump to remove any possible contaminants that could affect the sample. Electrons are produced by passing a large current through a tungsten filament before being accelerated through an electric field caused by a 5 kV voltage. This electron beam then comes in con-

tact with the desired metal causing sublimation and evaporation of the material towards the substrate. The rate of deposition can be controlled by varying the power of the beam and the thickness is monitored by a quartz crystal.

1.10 Aims

The main aim of this work is to further investigate the ability of DNA to act as a template for various compound materials and the effect this has on the electrical properties of the material. The compound materials to be examined are vanadium oxide, cadmium sulphide and carbon nanotubes with cadmium sulphide. This involves assessing the electrical performance of transistors in which the DNA templated nanowires have been incorporated. This is a major aim for the project as thus far no measurements have been recorded for a three terminal gated device using DNA templated nanowires. Finally some more novel measurements are to be recorded including the use of carbon nanotubes.

Bibliography

[1] J. D. Watson and F. H. C. Crick, *Nature*, 1953, **171**, 737–738.

[2] D. D. Eley and D. I. Spivey, *Transactions of the Faraday Society*, 1962, **58**, 411–415.

[3] A. J. Storm, J. van Noort, S. de Vries and C. Dekker, *Applied Physics Letters*, 2001, **79**, 3881–3883.

[4] S. M. D. Watson, A. R. Pike, J. Pate, A. Houlton and B. R. Horrocks, *Nanoscale*, 2014, **6**, 4027–4037.

[5] S. Veeraraghavan and J. Fossum, *IEEE Transactions on Electron Devices*, 1989, **36**, 522–528.

[6] V. K. Khanna, in *Integrated Nanoelectronics: Nanoscale CMOS, Post-CMOS and Allied Nanotechnologies*, ed. V. K. Khanna, Springer India, New Delhi, 2016, pp. 73–93.

[7] C. Duvvury, *IEEE Circuits and Devices Magazine*, 1986, **2**, 6–10.

[8] M. R. Arkin, E. D. A. Stemp, R. E. Holmlin, J. K. Barton, A. Hörmann, E. J. C. Olson and P. F. Barbara, *Science*, 1996, **273**, 475–480.

[9] M. D. Purugganan, C. V. Kumar, N. J. Turro and J. K. Barton, *Science*, 1988, **241**, 1645–1649.

[10] A. M. Brun and A. Harriman, *Journal of the American Chemical Society*, 1992, **114**, 3656–3660.

[11] H. W. Fink and C. Schönenberger, *Nature*, 1999, **398**, 407–410.

[12] Y. Okahata, T. Kobayashi, H. Nakayama and K. Tanaka, *Supramolecular Science*, 1998, **5**, 317–320.

[13] C. Dekker and M. Ratner, *Physics World*, 2001, **14**, 29–33.

[14] P. J. de Pablo, F. Moreno-Herrero, J. Colchero, J. Gómez Herrero, P. Herrero, A. M. Baró, P. Ordejón, J. M. Soler and E. Artacho, *Physical Review Letters*, 2000, **85**, 4992–4995.

[15] L. Xiang, J. L. Palma, C. Bruot, V. Mujica, M. A. Ratner and N. Tao, *Nature Chemistry*, 2015, **7**, 221–226.

[16] C. A. M. Seidel, A. Schulz and M. H. M. Sauer, *The Journal of Physical Chemistry*, 1996, **100**, 5541–5553.

[17] B. Giese, J. Amaudrut, A.-K. Köhler, M. Spormann and S. Wessely, *Nature*, 2001, **412**, 318–320.

[18] M. Cordes and B. Giese, *Chemical Society Reviews*, 2009, **38**, 892–901.

[19] S. M. Risser, D. N. Beratan and T. J. Meade, *Journal of the American Chemical Society*, 1993, **115**, 2508–2510.

[20] J. Jortner, M. Bixon, T. Langenbacher and M. E. Michel-Beyerle, *Proceedings of the National Academy of Sciences*, 1998, **95**, 12759–12765.

[21] P. W. K. Rothemund, *Nature*, 2006, **440**, 297–302.

[22] L. Mistry, O. El-Zubir, G. Dura, W. Clegg, P. G. Waddell, T. Pope, W. A. Hofer, N. G. Wright, B. R. Horrocks and A. Houlton, *Chemical Science*, 2019, **10**, 3186–3195.

[23] S. Katz, *Nature*, 1962, **195**, 997–998.

[24] A. Ono and H. Togashi, *Angewandte Chemie International Edition*, 2004, **43**, 4300–4302.

[25] P. Aich, S. L. Labiuk, L. W. Tari, L. J. T. Delbaere, W. J. Roesler, K. J. Falk, R. P. Steer and J. S. Lee, *Journal of Molecular Biology*, 1999, **294**, 477–485.

[26] S. Menzer, M. Sabat and B. Lippert, *Journal of the American Chemical Society*, 1992, **114**, 4644–4649.

[27] G. H. Clever and M. Shionoya, *Coordination Chemistry Reviews*, 2010, **254**, 2391–2402.

[28] K. Tanaka and M. Shionoya, *The Journal of Organic Chemistry*, 1999, **64**, 5002–5003.

[29] M. Tasaka, K. Tanaka, M. Shiro and M. Shionoya, *Supramolecular Chemistry*, 2001, **13**, 671–675.

[30] K. Tanaka, M. Tasaka, H. Cao and M. Shionoya, *European Journal of Pharmaceutical Sciences*, 2001, **13**, 77–83.

[31] E. Meggers, P. L. Holland, W. B. Tolman, F. E. Romesberg and P. G. Schultz, *Journal of the American Chemical Society*, 2000, **122**, 10714–10715.

[32] E. Braun, Y. Eichen, U. Sivan and G. Ben-Yoseph, *Nature*, 1998, **391**, 775–778.

[33] R. Mohammadzadegan, H. Mohabatkar, M. H. Sheikhi, A. Safavi and M. B. Khajouee, *Physica E: Low-dimensional Systems and Nanostructures*, 2008, **41**, 142–145.

[34] A. Ongaro, F. Griffin, P. Beecher, L. Nagle, D. Iacopino, A. Quinn, G. Redmond and D. Fitzmaurice, *Chemistry of Materials*, 2005, **17**, 1959–1964.

[35] S. M. D. Watson, N. G. Wright, B. R. Horrocks and A. Houlton, *Langmuir*, 2010, **26**, 2068–2075.

[36] H. Kudo and M. Fujihira, *IEEE Transactions on Nanotechnology*, 2006, **5**, 90–92.

[37] R. Hassanien, M. Al-Hinai, S. A. Farha Al-Said, R. Little, L. Šiller, N. G. Wright, A. Houlton and B. R. Horrocks, *ACS Nano*, 2010, **4**, 2149–2159.

[38] S. Pruneanu, S. A. F. Al-Said, L. Dong, T. A. Hollis, M. A. Galindo, N. G. Wright, A. Houlton and B. R. Horrocks, *Advanced Functional Materials*, 2008, **18**, 2444–2454.

[39] R. Hassanien, S. A. F. Al-Said, L. Šiller, R. Little, N. G. Wright, A. Houlton and B. R. Horrocks, *Nanotechnology*, 2012, **23**, 075601.

[40] J. Liu, B. Uprety, S. Gyawali, A. T. Woolley, N. V. Myung and J. N. Harb, *Langmuir*, 2013, **29**, 11176–11184.

[41] R. N. Nurdillayeva, B. R. Horrocks and A. R. Pike, *Materials Today: Proceedings*, 2018, **5**, 22825–22834.

[42] T. Bayrak, S. Helmi, J. Ye, D. Kauert, J. Kelling, T. Schönherr, R. Weichelt, A. Erbe and R. Seidel, *Nano Letters*, 2018, **18**, 2116–2123.

[43] M. Zheng, A. Jagota, E. D. Semke, B. A. Diner, R. S. Mclean, S. R. Lustig, R. E. Richardson and N. G. Tassi, *Nature Materials*, 2003, **2**, 338–342.

[44] Q. Ye, X. Xu, A. Paghi, T. Bamford, B. R. Horrocks, A. Houlton, G. Barillaro, S. Dimitrov and M. Palma, *Advanced Functional Materials*, 2021, **31**, 2105719.

[45] X. Liu, F. Zhang, X. Jing, M. Pan, P. Liu, W. Li, B. Zhu, J. Li, H. Chen, L. Wang, J. Lin, Y. Liu, D. Zhao, H. Yan and C. Fan, *Nature*, 2018, **559**, 593–598.

[46] H. T. Maune, S.-p. Han, R. D. Barish, M. Bockrath, W. A. G. Iii, P. W. K. Rothemund and E. Winfree, *Nature Nanotechnology*, 2010, **5**, 61–66.

[47] J. Allemand, D. Bensimon, L. Jullien, A. Bensimon and V. Croquette, *Biophysical Journal*, 1997, **73**, 2064–2070.

[48] A. Bensimon, A. Simon, A. Chiffaudel, V. Croquette, F. Heslot and D. Bensimon, *Science*, 1994, **265**, 2096–2098.

[49] H. Yokota, F. Johnson, H. Lu, R. M. Robinson, A. M. Belu, M. D. Garrison, B. D. Ratner, B. J. Trask and D. L. Miller, *Nucleic Acids Research*, 1997, **25**, 1064–1070.

[50] H. Nakao, H. Hayashi, T. Yoshino, S. Sugiyama, K. Otobe and T. Ohtani, *Nano Letters*, 2002, **2**, 475–479.

[51] J. Herrick and A. Bensimon, in *DNA Replication: Methods and Protocols*, ed. S. Vengrova and J. Z. Dalgaard, Humana Press, Totowa, NJ, 2009, pp. 71–101.

[52] C. Conti, S. Caburet, C. Schurra and A. Bensimon, *Current protocols in cytometry / editorial board, J. Paul Robinson, managing editor ... [et al.]*, 2001, **Chapter 8**, Unit 8.10.

[53] Z. E. Nazari and L. Gurevich, *Journal of Self Assembly and Molecular Electronics*, 2023, 125 – 148.

[54] A. I. Oliva, O. Solis-Canto, R. Castro-Rodriguez and P. Quintana, *Thin Solid Films*, 2001, **391**, 28–35.

[55] X. Mathew, J. P. Enriquez, A. Romeo and A. N. Tiwari, *Solar Energy*, 2004, **77**, 831–838.

[56] K. Deng and L. Li, *Advanced Materials*, 2014, **26**, 2619–2635.

[57] W. Zhao, L. Liu, M. Xu, X. Wang, T. Zhang, Y. Wang, Z. Zhang, S. Qin and Z. Liu, *Advanced Optical Materials*, 2017, **5**, 1700159.

[58] L. Dong, T. Hollis, B. Connolly, N. Wright, B. Horrocks and A. Houlton, *Advanced Materials*, 2007, **19**, 1748–1751.

[59] L. Q. Qian, S. L. Wang, X. Jia, Y. Y. Liu and W. H. Tang, *Journal of Alloys and Compounds*, 2009, **477**, 888–891.

[60] W. Qingqing, X. Gang and H. Gaorong, *Journal of Solid State Chemistry*, 2005, **178**, 2680–2685.

[61] S. Yan, L. Sun, Y. Sheng, N. Huang and Z. Xiao, *New Journal of Chemistry*, 2011, **35**, 299–302.

[62] X. Duan, C. Niu, V. Sahi, J. Chen, J. W. Parce, S. Empedocles and J. L. Goldman, *Nature*, 2003, **425**, 274–278.

[63] R. M. Ma, L. Dai and G. G. Qin, *Applied Physics Letters*, 2007, **90**, 093109.

[64] L. Li, Z. Lou and G. Shen, *ACS Applied Materials & Interfaces*, 2015, **7**, 23507–23514.

[65] K. Heo, H. Lee, Y. Park, J. Park, H.-J. Lim, D. Yoon, C. Lee, M. Kim, H. Cheong, J. Park, J. Jian and S. Hong, *Journal of Materials Chemistry*, 2012, **22**, 2173–2179.

[66] Q. Lu, S. R. Bishop, D. Lee, S. Lee, H. Bluhm, H. L. Tuller, H. N. Lee and B. Yildiz, *Adv. Funct. Mater.*, 2018, **28**, 1803024.

[67] Z. Shao, X. Cao, H. Luo and P. Jin, *NPG Asia Mater*, 2018, **10**, 581–605.

[68] G. Stefanovich, A. Pergament and D. Stefanovich, *J. Phys.: Condens. Matter*, 2000, **12**, 8837.

[69] M. Li, S. Magdassi, Y. Gao and Y. Long, *Small*, 2017, **13**, 1701147.

[70] H. Yin, C. Song, Z. Wang, H. Shao, Y. Li, H. Deng, Q. Ma and K. Yu, *Nanomaterials*, 2019, **9**, 317.

[71] T. Yajima, T. Nishimura and A. Toriumi, *Nature Communications*, 2015, **6**, 10104.

[72] D. Ruzmetov, G. Gopalakrishnan, C. Ko, V. Narayanamurti and S. Ramanathan, *Journal of Applied Physics*, 2010, **107**, 114516.

[73] T. Wei, T. Kanki, K. Fujiwara, M. Chikanari and H. Tanaka, *Applied Physics Letters*, 2016, **108**, 053503.

[74] Y. Zhang, W. Xiong, W. Chen, X. Luo, X. Zhang and Y. Zheng, *Physical Chemistry Chemical Physics*, 2020, **22**, 4685–4691.

[75] F. Théobald, R. Cabala and J. Bernard, *Journal of Solid State Chemistry*, 1976, **17**, 431–438.

[76] Q. Zhao, L. Jiao, W. Peng, H. Gao, J. Yang, Q. Wang, H. Du, L. Li, Z. Qi, Y. Si, Y. Wang and H. Yuan, *Journal of Power Sources*, 2012, **199**, 350–354.

[77] S. Choi, G. Ahn, S. J. Moon and S. Lee, *Sci Rep*, 2020, **10**, 9721.

[78] S. Lee, X.-G. Sun, A. A. Lubimtsev, X. Gao, P. Ganesh, T. Z. Ward, G. Eres, M. F. Chisholm, S. Dai and H. N. Lee, *Nano Lett.*, 2017, **17**, 2229–2233.

[79] C. Subba Reddy, E. H. Walker, S. Wicker, Q. L. Williams and R. R. Kalluru, *Current Applied Physics*, 2009, **9**, 1195–1198.

[80] F. Krumeich, H.-J. Muhr, M. Niederberger, F. Bieri, B. Schnyder and R. Nesper, *Journal of the American Chemical Society*, 1999, **121**, 8324–8331.

[81] W. Chen, J. Peng, L. Mai, H. Yu and Y. Qi, *Solid State Communications*, 2004, **132**, 513–516.

[82] Y. Oka, T. Yao, N. Yamamoto, Y. Ueda and A. Hayashi, *Journal of Solid State Chemistry*, 1993, **105**, 271–278.

[83] S. A. Corr, M. Grossman, Y. Shi, K. R. Heier, G. D. Stucky and R. Seshadri, *J. Mater. Chem.*, 2009, **19**, 4362–4367.

[84] F. J. Morin, *Physical Review Letters*, 1959, **3**, 34.

[85] P. Hu, P. Hu, T. D. Vu, M. Li, S. Wang, Y. Ke, X. Zeng, L. Mai and Y. Long, *Chem. Rev.*, 2023, **123**, 4353–4415.

[86] N. Vardi, E. Anouchi, T. Yamin, S. Middey, M. Kareev, J. Chakhalian, Y. Dubi and A. Sharoni, *Advanced Materials*, 2017, **29**, 1605029.

[87] T. Driscoll, H.-T. Kim, B.-G. Chae, B.-J. Kim, Y.-W. Lee, N. M. Jokerst, S. Palit, D. R. Smith, M. Di Ventra and D. N. Basov, *Science*, 2009, **325**, 1518 – 1521.

[88] J. M. Wu and W. E. Chang, *ACS Applied Materials Interfaces*, 2014, **6**, 14286 – 14292.

[89] P. Markov, R. E. Marvel, H. J. Conley, K. J. Miller, R. F. J. Haglund and S. M. Weiss, *ACS Photonics*, 2015, **2**, 1175–1182.

[90] C. J. Dahlman, G. LeBlanc, A. Bergerud, C. Staller, J. Adair and D. J. Milliron, *Nano Letters*, 2016, **16**, 6021 – 6027.

[91] Y. Li, S. ji, Y. Gao, H. Luo and M. Kanehira, *Scientific reports*, 2013, **3**, 1370.

[92] S. Iijima, *Nature*, 1991, **354**, 56–58.

[93] N. Anzar, R. Hasan, M. Tyagi, N. Yadav and J. Narang, *Sensors International*, 2020, **1**, 100003.

[94] M. Filchakova and V. Saik, *Single-walled Carbon Nanotubes: Structure, Properties, Applications*, `https://tuball.com/articles/single-walled-carbon-nanotubes`.

[95] K. Lönnecke, O. Eberhardt and T. Wallmersperger, *Acta Mech*, 2023, **234**, 1–16.

[96] S. G. Louie, in *Carbon Nanotubes: Synthesis, Structure, Properties, and Applications*, ed. M. S. Dresselhaus, G. Dresselhaus and P. Avouris, Springer, Berlin, Heidelberg, 2001, pp. 113–145.

[97] K. Keren, R. S. Berman, E. Buchstab, U. Sivan and E. Braun, *Science*, 2003, **302**, 1380–1382.

[98] M. Zhao, Y. Chen, K. Wang, Z. Zhang, J. K. Streit, J. A. Fagan, J. Tang, M. Zheng, C. Yang, Z. Zhu and W. Sun, *Science*, 2020, **368**, 878–881.

[99] Y. Chen, M. Zhao, Y. Ouyang, S. Zhang, Z. Liu, K. Wang, Z. Zhang, Y. Liu, C. Yang, W. Sun, J. Shen and Z. Zhu, *Nature Protocols*, 2023, **18**, 2975–2997.

[100] A. Sommerfeld, *Zeitschrift für Physik*, 1928, **47**, 1–32.

[101] P. Drude, *Annalen der Physik*, 1900, **306**, 566–613.

[102] S. H. Simon, *The Oxford Solid State Basics*, Oxford University Press, Incorporated, Oxford, UNITED KINGDOM, 2013.

[103] *P-N Junction*, 2020, `https://devxplained.eu/en/blog/p-n-junction`.

[104] N. A. Poklonskii, S. Y. Lopatin and A. G. Zabrodskii, *Physics of the Solid State*, 2000, **42**, 441–449.

[105] N. F. Mott, *The Philosophical Magazine: A Journal of Theoretical Experimental and Applied Physics*, 1969, **19**, 835–852.

[106] A. L. Efros and B. I. Shklovskii, *Journal of Physics C: Solid State Physics*, 1975, **8**, L49.

[107] J. C. Jernigan and R. W. Murray, *The Journal of Physical Chemistry*, 1987, **91**, 2030–2032.

[108] R. H. Terrill, J. E. Hutchison and R. W. Murray, *The Journal of Physical Chemistry B*, 1997, **101**, 1535–1542.

[109] E. F. Dalton, N. A. Surridge, J. C. Jernigan, K. O. Wilbourn, J. S. Facci and R. W. Murray, *Chemical Physics*, 1990, **141**, 143–157.

[110] M. Roser, H. Ritchie and M. Edouard, *What is Moore's Law?*, 2023, `https://ourworldindata.org/moores-law`, Publication Title: Our World in Data.

[111] M. R. Ritchie, Hannah, *English: A logarithmic graph showing the timeline of how transistor counts in microchips are almost doubling every two years from 1970 to 2020;*

Moore's Law., 2020, https://commons.wikimedia.org/wiki/File:Moore%27s_Law_Transistor_Count_1970-2020.png.

[112] M. M. Atalla, E. Tannenbaum and E. J. Scheibner, *Bell System Technical Journal*, 1959, **38**, 749–783.

Chapter 2

Materials and Techniques

2.1 Reagents and Materials

For all preparations λ-DNA was purchased from New England Bio Labs (product code N3011L) and was used without any further treatment. The V_2O_5, oxalic acid, [$Cd(NO_3)_2.4H_2O$] and Na_2S used for the preparation of VO_2 and CdS were purchased from Sigma-Aldrich and were used without any further purification. All water used was obtained from a Millipore water system that produced type I water of 18.2 $\mathrm{M\Omega\,cm}$ nominal resistivity.

Multi-walled carbon nanotubes (Elicarb^{TM} P940) were purchased from Thomas Swan (Consett, UK). The MWCNTs were specified as having a mean diameter range of 10 - 12 nm and a maximum metal oxide content of 5 wt%. The interdigitated electrodes (IDEs) were purchased from DropSens, catalogue G-IDEPT10, and had a cell constant of 0.0188 $\mathrm{cm^{-1}}$. The IDEs were made up of 125 x 2 platinum digits with a width of 10 $\mu\mathrm{m}$ and length of 6760 $\mu\mathrm{m}$ on glass with a 10 $\mu\mathrm{m}$ gap between each digit. They were cleaned in ethanol before the first use. All electrodes were tested for faults before the sample was added. The silicon used for the FET devices was purchased from Inseto. The wafer had a crystallographic orientation of 100 and had been doped with phosphorus to make it a N-type wafer. The resistivity of the silicon was 1 - 10 $\Omega.\mathrm{cm}$ and the oxide thickness was 25 nm. The silicon was cleaned by sonicating in deionised water and then acetone before use.

2.2 Preparation of DNA-Templated Nanowires

2.2.1 Preparation of DNA-Templated Vanadium Dioxide Nanowires

VO_2-DNA nanowires were prepared through the reduction of V_2O_5 using oxalic acid. 191 mg of V_2O_5 (1.05 mmol) was added to a 35 mL H_2O:acetone (5:2) solution. This was followed by 397 mg of oxalic acid ($C_2H_2O_4$, 3.14 mmol). The flask was then evacuated and left stirring for 18 hours at 40 °C during which time the solution colour had changed from bright orange to light blue. The solution was allowed to cool to room temperature before 100 $\mu\mathrm{L}$ of λ-DNA (500 $\mathrm{ng}\ \mu\mathrm{L}^{-1}$) was slowly added and allowed to stir for 24 hours. The solution was transferred to a Teflon lined steel autoclave (4 cm diameter, 125 cm^3 volume) and heated to 180 °C for 24 hours and allowed to cool naturally to room temperature. The solution was then filtered and the black precipitate was kept and washed with H_2O and acetone.

To then prepare VO_2-DNA dispersions, 5 mg of the precipitate was added to 500 $\mu\mathrm{L}$ of deionized H_2O, mixed vigorously before being left for a further 24 hours after which the solution was centrifuged for 5 minutes and the supernatant removed and stored.

2.2.2 Preparation of DNA-Templated Cadmium Sulphide Nanowires

To prepare the cadmium sulphide (CdS) nanowires the same method was followed as found in the paper by Dong.[1] A two stage reaction was used in which $Cd(NO_3)_2$ (100 $\mu\mathrm{L}$ 0.2 mM) was added dropwise to a stirring solution of λ-DNA (100 $\mu\mathrm{L}$, 500 $\mathrm{ng\,mL}^{-1}$) followed by Na_2S (100 $\mu\mathrm{L}$ 0.2 mM) also added drop-wise. The suspension was left for 24 hours at 4 °C. After this incubation , $Cd(NO_3)_2$ (10 $\mu\mathrm{L}$ 20 mM) was added drop-wise to the stirring solution. Finally Na_2S (10 $\mu\mathrm{L}$ 20 mM) was added drop-wise and the dispersion was stored at 4 °C for 24 before it was ready to be used.

2.2.3 Preparation of DNA-Templated Carbon Nanotube-Cadmium Sulphide Nanowires

Previous work has shown that CdS can be formed on DNA-wrapped SWCNTs.[2] In this work, MWCNTs were used with DNA to template the precipitation of CdS as described

below.

0.1 mg of MWCNTs was added to 10 mL of methanol and sonicated for 3 hours at room temperature. 100 μL of λ-DNA (100 μL, 500 $\mathrm{ng\,mL^{-1}}$) was added to 500 μL of the MWCNT suspension before being sonicated for 5 min and allowed to stand overnight. To finish the composite, the same method mentioned in section 2.2.2 was used in which $Cd(NO_3)_2$ (100 μL 0.2 mM) was added drop-wise to the CNT-DNA suspension followed by Na_2S (100 μL 0.2 mM) also being added drop-wise. The suspension was left for 24 hours at 4 $^{\circ}\mathrm{C}$. After this incubation $Cd(NO_3)_2$ (10 μL 20 mM) was added drop-wise to the stirring solution. Finally Na_2S (10 μL 20 mM) was added drop-wise and left at 4 $^{\circ}\mathrm{C}$ for 24 before it was ready to be used.[1]

2.3 Characterisation Techniques

2.3.1 Fourier Transform Infrared Spectroscopy

Fourier Transform Infrared Spectroscopy (FTIR) was used in order to help characterize VO_2-DNA and CNT-CdS-DNA nanowires. Samples were recorded on a Shimadzu IRAffinity-1S Fourier Transform Infrared Spectrophotometer with a 4 $\mathrm{cm^{-1}}$ spectral resolution in the range of 400 - 4000 $\mathrm{cm^{-1}}$ in which 50 scans were collected and averaged. For aqueous samples a background was recorded using a clean silicon wafer after the instrument had been purged with nitrogen. The samples were then dropcast onto the silicon and allowed to dry, after which the spectra obtained. For powder samples, an attenuated total reflectance (ATR) attachment was used. The instrument was again purged with nitrogen before a background reading was recorded, after which the desired spectra were recorded.

2.3.2 Ultraviolet Visible Spectroscopy

Ultraviolet Visible Spectroscopy (UV-Vis) samples were measured between 240 - 800 nm using a Thermo Scientific NanoDrop One MicroVolume spectrometer at room temperature. VO_2-DNA samples were measured in a 1 cm path-length cuvette using deionised water as a background. They were prepared for the measurement by mixing 1 mL of VO_2-DNA with 2 mL of deionised water.

Owing to the smaller volumes of CdS-DNA and CNT-CdS-DNA available for measurements, the nanodrop functionality of the spectrometer was utilised. Using the nanodrop allows smaller amounts of sample to be used at higher concentrations. After recording a background using the respective solvents stated in sections 2.2.1,2.2.2 and 2.2.3, 2 μL of sample was used in order to obtain a spectrum.

2.3.3 Atomic Force Microscopy

Atomic force microscopy (AFM) is a high resolution surface analysis technique that is used for a large variety of applications in a range of different disciplines including polymers, cell biology and semiconductor technology. It was first invented by Binnig et al in 1986.[3] AFM is a type of scanned probe microscopy, that relies on the interaction of a small probe (the tip) with the sample surface. Probe microscopes rely heavily on the use of piezoelectric actuators to enable the fine (nanometre-scale or better) control over the tip motion.

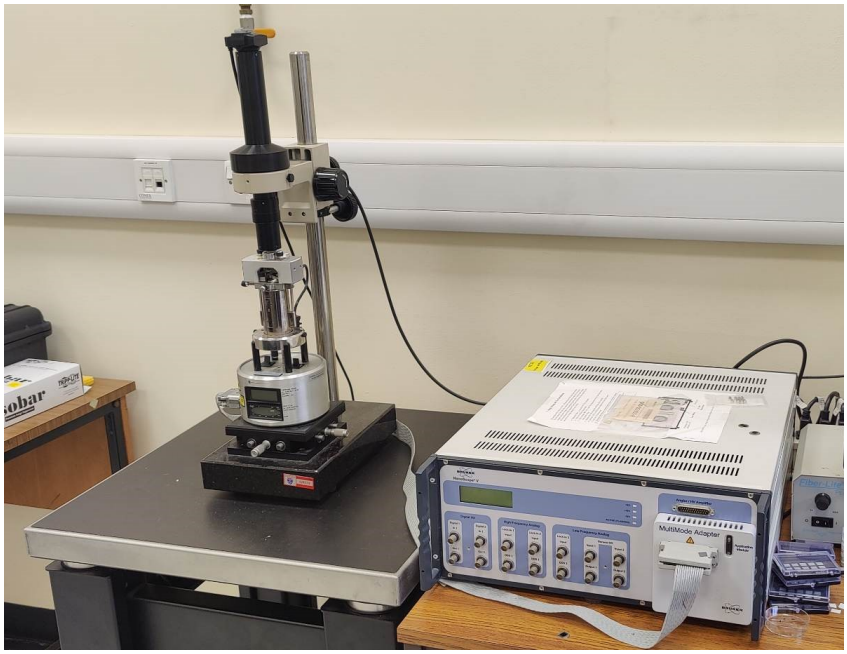

Figure 2.1: The atomic force microscope used for this research.

There are three main modes used in AFM: contact mode, non-contact mode and tapping mode of which are described in more detail below. The AFM used in this research was a Nanoscope Multimode VIII system utilising ScanAsyst image mode and is shown in figure 2.1. A silicon nitride cantilever with a spring constant of 0.4 $\mathrm{N\,m^{-1}}$ was used. All images

were analysed using the manufacturer-supplied Nanoscope analysis software version 1.8. AFM also has other functionalities such as conductive AFM (C-AFM) which measures the conductivity of a material by applying a bias to the tip and electrostatic force microscopy (EFM) which measures the electrostatic forces between the tip and the surface. Finally, scanned conductance microscopy (SCM) is similar to EFM, but is used to detect weakly conductive objects in a non-contact manner described below.

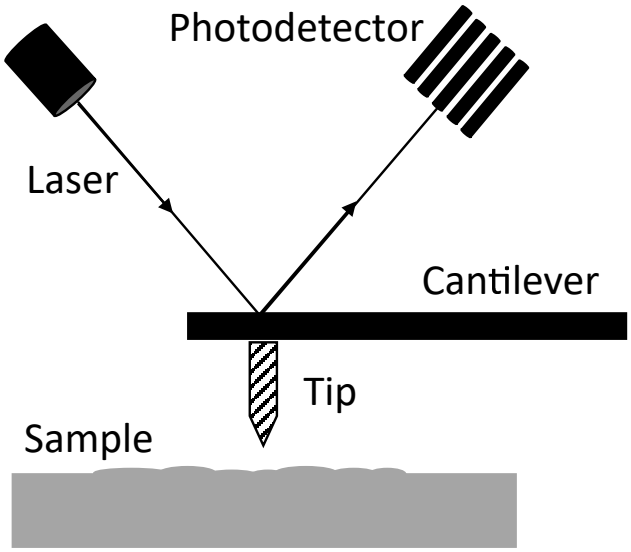

Figure 2.2: A schematic of the working principle of atomic force microscopy. As the tip is attracted or repelled by the sample the cantilever bends. This bending is detected by reflection of a low power laser beam from the back of the cantilever onto a split photodiode. The difference in the signals measured by the two halves of the photodetector determines the displacement of the cantilever compared to the original equilibrium.

Figure 2.2 shows a general schematic of the working principle of an AFM. The tip is moved across the sample under the control of a three-axis piezoelectric actuator. The tip may be in contact, above the sample or tapping on the sample depending on the mode being used. As the cantilever is repelled or attracted to the surface, its deflection is detected optically using a low power laser reflecting from the back of the cantilever and a split photodiode as a photodetector. Height variations across the sample correspond to differences in light intensity on the separate sections of the split photodiode. Using the feedback control system to maintain constant deflection (height), a false colour map of the topography of the surface is constructed line-by-line as the tip scans over the surface in a raster pattern. Using 4-section split photodiodes, the twisting motion of the tip may also be recorded.

During AFM there are multiple interactions that occur between the tip at the end of

the cantilever and the sample itself. The two main interactions are van der Waals interactions and the Pauli repulsion which occur between atoms or molecules and depend on the distance between them. If these atoms or molecules get close to each other then the wavefunctions can overlap which leads to a repulsion. The Lennard-Jones potential is an approximate form for the combination of these two effects.

$$V(r) = 4\epsilon \left[\left(\frac{\sigma}{r}\right)^{12} - \left(\frac{\sigma}{r}\right)^{6} \right] \tag{2.1}$$

in which r is the distance between the atoms or molecules, ϵ is the depth of the potential minimum and σ is the distance between the atoms or molecules when the potential is zero (V(r = σ) = 0). The positive term describes the repulsion and the negative, the attractive interactions.

As mentioned above there are three modes of AFM, contact, tapping and non-contact, which vary by the way the cantilever is positioned and moves during image collection. Contact mode involves the tip making contact with the surface before being moved across the sample. Owing to the distance between the tip and sample being kept small it is then possible to measure the tip-sample force directly. It is more common however to keep the force on the tip constant and to measure the displacement of the cantilever. A topographical image can then be created by plotting the relative displacement value at each point. The disadvantage of contact mode is the tendency to cause damage to samples because of the strong tip/sample interaction.

Tapping mode AFM (TM-AFM) was the mode chosen for this work due to the non-destructive nature which renders it suitable for the soft samples being imaged. Other benefits include being able to scan samples with loosely attached objects and the decreased risk of damage of the tip. In TM-AFM the cantilever oscillates up and down near the resonant frequency with the tip touching the surface of the sample intermittently as the tip moves down. During the oscillation the frequency and amplitude of the drive signal are kept at a constant however as the cantilever approaches the sample surface the amplitude changes due to tip-surface interactions.[4–6] Tapping mode was chosen for this research due to the delicate nature of the samples. It was chosen over non-contact mode (described below) due to the ease of use and lack of extra hardware required.

Non-contact mode AFM is different from contact and tapping mode as it operates in

an attractive tip-sample force regime. In non-contact mode, the cantilever oscillates at its resonance frequency in close proximity to the sample (in the order of angstroms). At short tip-sample distances the Pauli repulsion is the dominant force due to the principle forbidding the overlap of electron clouds, this is what is seen in contact and tapping mode AFM. As the tip is moved further from the sample the attractive van der Waals forces start to become the dominant interaction. Non-contact mode shares the benefit of being usable on soft samples due to the non-destructive nature of the method.

Samples were prepared for atomic force microscopy by first diluting them by a factor of 10^4. If the concentration of the solution is too high, individual details such as wires will not be seen owing to film formation on the substrate. Silicon chips were used as a substrate for VO_2-DNA samples. The chips were first sonicated in deionised water for 15 minutes followed by 15 minutes sonication in acetone. Next, they were immersed in a 3:1 piranha solution (H_2O_2 : conc H_2SO_4) for 1 hour and rinsed under running deionised water. 2 μL of the diluted samples were then dropcast onto the cleaned silicon chips and left to dry in a laminar flow hood before being imaged. The laminar flow hood was used in order to minimise the risk of any outside impurities such as dust being present when an image was recorded.

Mica was the substrate of choice for CdS-DNA and CNT-CdS-DNA samples as the preparation process is easier and more efficient than silicon. The top few layers of mica were removed using sellotape to reveal a fresh, clean surface. Then 2 μL of dilute sample was applied and the chip was allowed to dry in a laminar flow hood. Mica sheets (75 mm $\times$ 20 mm, 0.15 mm thick) were purchased from Agar Scientific (Stansted, Essex, UK) and cut into 1 cm^2 squares. The mica was mounted on steel specimen discs using carbon tape.

2.3.4 Scanned Conductance Microscopy

Electrostatic force microscopy (EFM) is a variation of AFM in which the electrostatic forces between the sample surface and a biased, metallised AFM tip are investigated as shown in figure 2.3. Most users of EFM are looking for trapped charges within a sample however in this research EFM was used to detect the conductance of the sample, a mode which has been referred to as using scanned conductance microscopy (SCM).[7,8] Both methods are detailed below as well as the method to distinguish the two effects.

The main working principle for standard EFM is the different dependence on tip-sample distance between van der Waals and electrostatic forces. Van der Waals forces act at a tip-sample distance of between 1 - 10 nm whereas electrostatic forces have a range of more than 1 $\mu\mathrm{m}$ meaning van der Waals forces are the main factor when the tip is close to the sample, however when the tip is moved to a greater distance from the sample the electrostatic forces become dominant. In lift mode EFM the cantilever passes over the sample twice in which the first scan measures the topography before the cantilever is then lifted a constant height (typically a few tens of nm) so that the distance between the tip and the sample allows for the electrostatic interactions to be measured. As the tip is moved over the sample in the second pass, the cantilever oscillates at its resonant frequency, however this frequency is altered due to attractive and repulsive electrostatic forces between the tip and sample. When an attractive force is encountered, the cantilever 'softens' and the tip is moved towards the sample and the resonant frequency decreasing. The opposite is true for repulsive forces in which the cantilever 'hardens' and the tip moves away from the sample with the resonant frequency increasing. A phase image can then be produced by comparing the difference between the cantilever oscillation signal and the driving signal to the piezoelectric actuator.

The tip and sample during the second scan of lift mode EFM can be compared to the small capacitor in which:

$$U = \frac{1}{2}CV^2 \tag{2.2}$$

where U is the energy stored in the the capacitance (C) which is charged by application of a bias voltage (V). From this the magnitude of the force is given by the first derivative of the potential as a function of the tip height z:

$$F = \frac{1}{2}\frac{dC}{dz}(\Delta V)^2 \tag{2.3}$$

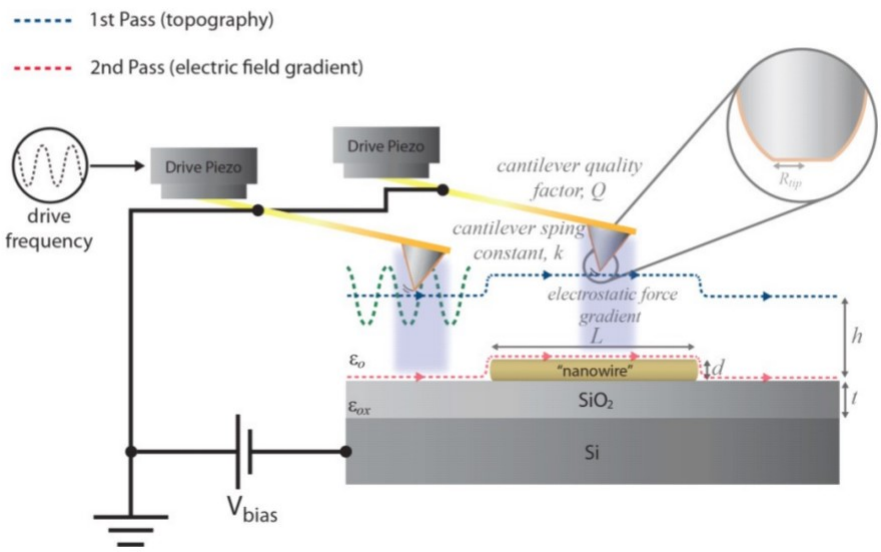

Figure 2.3: A schematic of the working principle of electrostatic force microscopy. As the charged tip passes over the sample the amplitude is effected due to electrostatic forces.

For SCM, the cantilever with a metal tip also passes over the sample twice; the first being to measure the topography of the sample and the second measures the phase change of the tip oscillation with respect to the signal driving the tapping motion when the tip is raised to a fixed height as in EFM. However, even in the absence of electrostatic charge on the surface, the tip and sample constitute a capacitor in which energy is stored due to the DC bias applied to the tip. It is this capacitive coupling that is the source of the SCM effect. SCM can be understood by considering the system shown in figure 2.3 in which the sample comprises a nanowire lying on top of a silicon substrate with an intervening SiO_2 oxide film. The presence of the nanowire affects the capactance between tip and the underlying Si substrate.

As the tip oscillates above the nanowire in lift mode, the nanowire will be polarised. The extent of this polarisation depends on the conductivity of the nanowire; for an insulating nanowire, only the region immediately below the tip will be polarised because of the absence of mobile charges. The effect can be appreciated by considering a simple model in which the nanowire is a thin strip of thickness d and permittivity ϵ. R is the tip radius and L is the length of nanowire polarised by the tip. For an insulating material the measured phase shift will always show as positive because $L = R$ and the first term on the right of equation 2.4, representing a contribution from the tip/dielectric/substrate background, is

always greater than the second term which represents the tip/nanowire/dielectric/substrate contribution. However, when a sample is conductive, the phase shift in relation to the background is negative. This is due to the potential polarising a larger region along a conductive nanowire and therefore $L >> R$. A criterion for this case can be determined by comparing the oscillation frequency of the tip to the RC time constant for the nanowire/substrate capacitance.[7] When the sample is a nanostructure the capacitance is small meaning that $\omega RC << 1$. Due to the second derivative of the energy stored within the tip / sample capacitor in relation to the tip is equivalent to an additional contribution to the force constant of the cantilever, the phase shift shows as negative. Importantly, the phase shift ($\Delta\phi$) owing to the SCM effect can be distinguished from that due to the usual EFM effect because it is proportional to the applied DC bias potential squared (V^2) and is given by equation 2.4:[8]

$$\tan(\Delta\phi) = \frac{Q}{2k}V^2\left[\frac{2\pi R^2\epsilon_0}{(h+\frac{t}{\epsilon_{ox}})^3} - \frac{2\pi L^2\epsilon_0}{(h+\frac{t}{\epsilon_{ox}}+\frac{d}{\epsilon})^3}\right] \tag{2.4}$$

In which d is the nanowire thickness, t is the dielectric layer thickness on the substrate and ϵ and ϵ_{ox} are the corresponding relative permittivities. Using this equation, $\Delta\phi$ will depend on the bias on the tip V and the ration between the cantilever spring constant to the quality factor $\frac{Q}{k}$. L and R are the size of the polarized region and the tip radius respectively in which $L \simeq R$ and $\Delta\phi > 0$ if the sample is insulating and $L \gg R$ and $\Delta\phi < 0$ if it is conductive. In contrast, the usual electrostatic charge effects studied by EFM will change sign when the sign of the bias applied to the tip changes.

2.3.5 Powder X-ray Diffraction

Powder X-ray diffraction (pXRD) is derived from X-ray diffraction of individual crystallites in random orientations with respect to the incident beam. It involves the measurement of the intensity of X-rays scattered from electrons bound to atoms.[9] pXRD is a non destructive and non contact method of analysis that can be used to provide accurate information about the arrangement of atoms and their spacing. In laboratory equipment, X-rays are produced by a cathode ray tube, filtered to produce monochromatic radiation, and concentrated before being sent towards a sample. When the incident rays interact with a sample,

most rays penetrate the sample, but some are reflected from crystal plans within the sample. At most scattering angles, the reflected beams cancel each other out by destructive interference. However, constructive interference is produced when the pathlength difference for beams reflected from different atomic planes is an integer number of wavelengths. The scattering angles θ at which this occurs are given by Bragg's Law:

$$n\lambda = 2dsin\theta \tag{2.5}$$

This can also be shown visually as found below in figure 2.4:

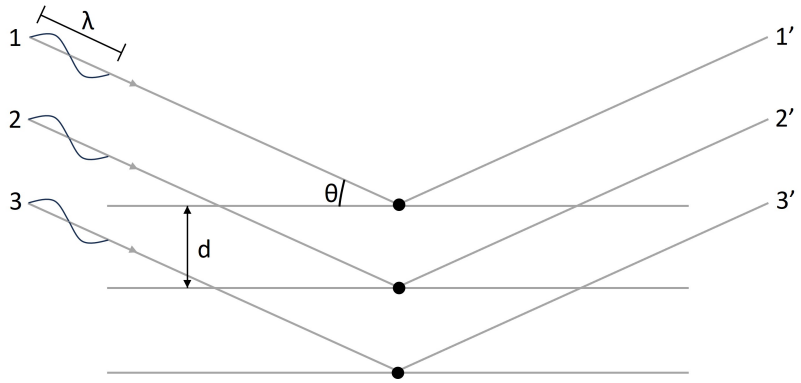

Figure 2.4: A diagram showing Bragg diffraction in which 3 beams of identical wavelengths scattering of 3 different atoms. The lower the beam the further it has to travel by an extra $2dsin\theta$.

in which λ is the wavelength of the X-ray, d is the crystal spacing, θ is the incident angle and n is an integer. X-rays get diffracted by crystals because the wavelength of X-rays is similar to the inter-atomic spacing inside crystals.

The samples were suspended in methanol and transferred to a zero-background holder. A preliminary scan was measured to determine the location of all the diffraction peaks before a higher resolution scan was run. The 2θ range: 10 - 90°, step size: 0.0334°, time per step: 12 s. Soller slit: 0.04 rad, beam mask: 20 mm and slit 2 = 0.5°.

2.3.6 X-ray Photoelectron Spectroscopy

X-ray photoelectron spectroscopy (XPS) is a widely used surface sensitive electron emission spectroscopic technique. It utilises the photoelectric effect caused by X-ray radiation in which a photon enters the sample and when it interacts with an atom, a core electron is ionized and ejected. A simplistic view of this can be seen in figure 2.5. This ejected

electron is then transported through an ultra high vacuum to a detector which measures the kinetic energy. The binding energy can then be calculated using equation 2.6:

$$E_k = hv - E_b - \phi \tag{2.6}$$

in which E_k is the kinetic energy, E_b is the binding energy, hv is the incident photon energy and ϕ is the work function of the spectrometer. Each element has a unique binding energy which can then be used to identify the elemental composition of the sample. Owing to the short mean free path of photoelectrons XPS is sensitive to the top few nm of sample surface.

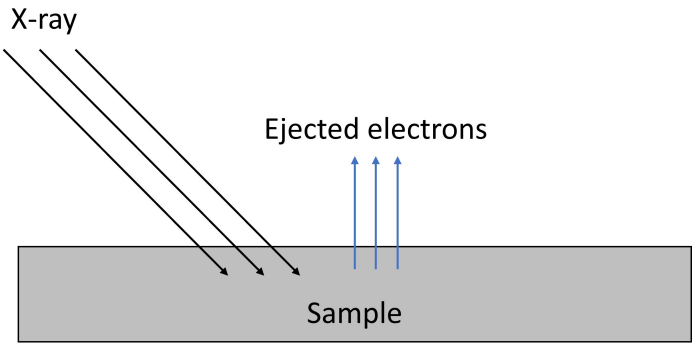

Figure 2.5: A simple diagram for the working principle of XPS. As X-rays enter a sample, core electrons are ionized and ejected from the sample.

Samples of VO_2-DNA were prepared in two ways for X-ray photoelectron spectroscopy (XPS) in order to compare the black precipitate formed during the autoclave stage and the aqueous solution prepared from the precipitate. For the solid samples a thin layer of powder was applied to a carbon tape tipped metal stub which was then used for all measurements. For aqueous samples of VO_2-DNA and CdS-CNT-DNA samples were first dropcast onto clean silicon wafers and allowed to dry before being attached to carbon taped tipped metal stubs. The samples were measured using a monochromic Al Kα X-ray excitation source of a Thermo Scientific K-Alpha X-ray photoelectron spectrometer with a 30 - 400 μm spot size. The photoelectrons were filtered with a hemispherical analyser and the measured with a multichannel detector. To eliminate electrostatic charges on the surface of the sample a dual beam neutralisation gun was used. For survey scans, the pass energy was 150 eV with 0.4 eV per step and for high resolution scans it was 40 eV with 0.1 eV per step. The calibration for the vanadium samples was done using the Au 4f

peak at 84 eV and the CdS-CNT-DNA samples were calibrated using the C 1s peak at 284.8 eV. CasaXPS (version 2.3.16 Casa Software Ltd, Teignmouth, UK) was then used for peak fitting and analysis.

2.4 Electrical Measurements

2.4.1 Current Voltage Curves

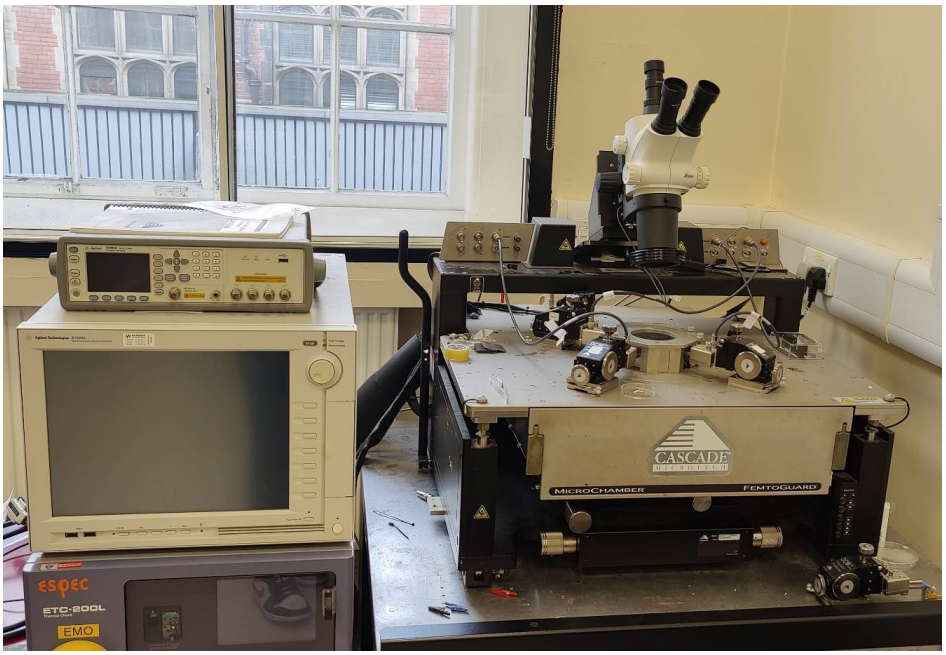

Figure 2.6: The Cascade Micro-Tech probe station used for this research.

Current - voltage curves were recorded by first dropcasting 10 $\mu\mathrm{L}$ of the desired nanowire solution onto a 10 $\mu\mathrm{m}$ platinum interdigitated electrode (IDE) and allowed to dry for 2 hours. After drying the IDEs were inserted into a Cascade Mirco-Tech probe station (pictured in figure 2.6) under a nitrogen atmosphere. For non-ohmic IV curves, a differential conductivity $g(V)$ can be defined by equation 2.7.

$$g(V) = \frac{\partial i}{\partial V} = \sigma \tag{2.7}$$

A representative example of an IV recording for a sufficiently cleaned electrode is shown in figure 2.7. Curves were then recorded between -2 to + 2 V in the dark, with a step of 200 mV and a delay of 10 ms. Agilent Easy EXPERT software was used to collect the results.

For temperature measurements an ESQEC ETC-200L thermal chuck was used to heat the samples. The chuck was brought up to the desired temperature and the sample allowed to equilibrate over 20 minutes before a measurement was recorded.

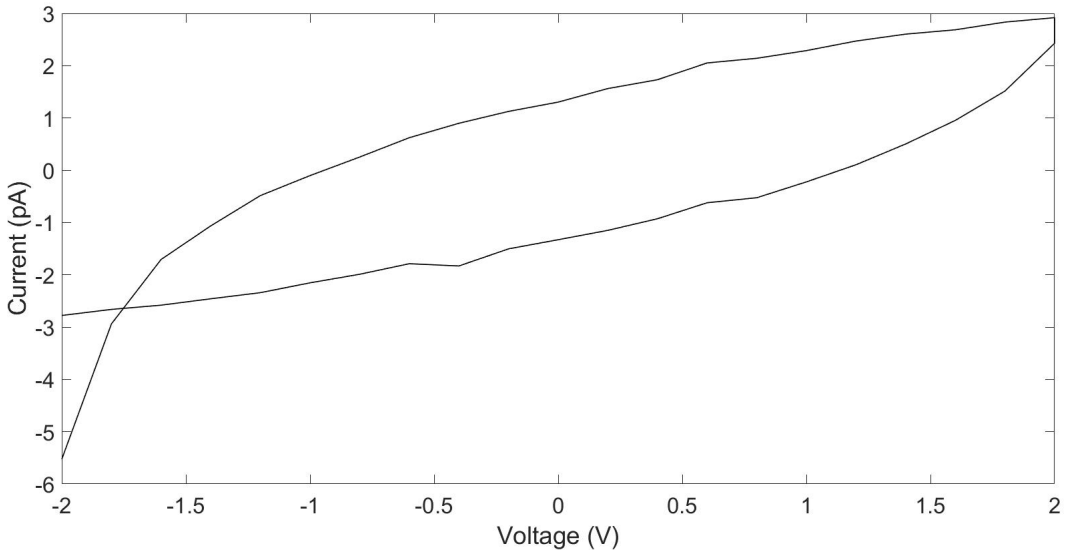

Figure 2.7: An IV curve of a fresh interdigitated electrode. New and freshly cleaned electrodes were characterised by measurement of IV curves in order to check for contaminants. Electrodes which showed background currents in the low pA range were deemed suitable for use.

2.4.2 Fabrication of Field Effect Transistors

To test the ability of the DNA-templated nanowires 3 terminal devices were prepared using standard clean room techniques such as photolithography and metal deposition. The full process is detailed below as well as a figure showing each step. The substrate used is a N-doped Si (100) wafer with a resistivity of 1 - 10 $\Omega.\mathrm{cm}$ which is precoated with a 25 nm oxide layer. In all stages the photoresist used was AZ-5214E and the developer AZ-326. All exposure steps were carried out using an 11.5 $\mathrm{mW/cm^2}$ UV light using a MJB-3 Mask Aligner imaged below (figure 2.8).

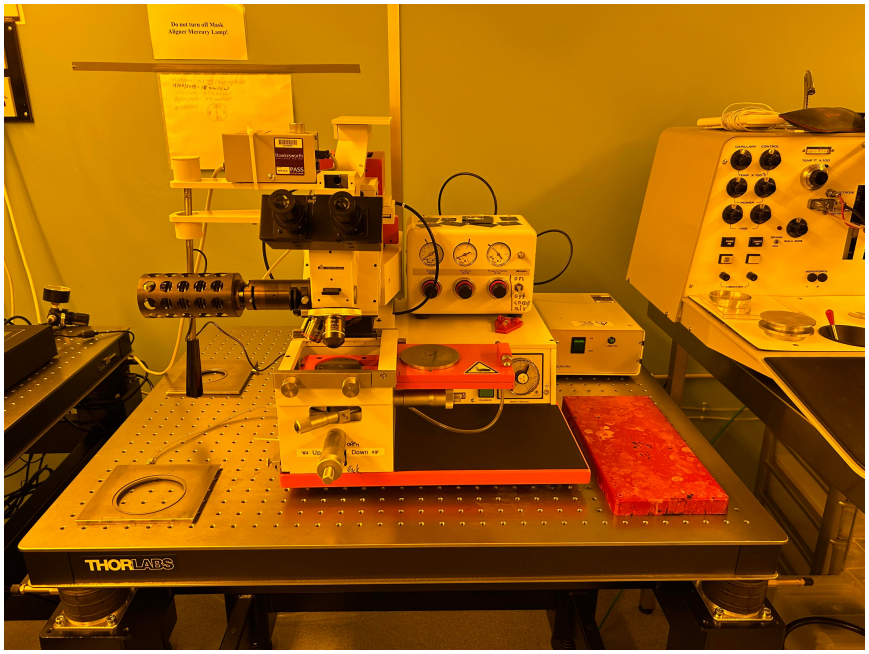

Figure 2.8: The MJB-13 Mask Aligner used for this research.

Silicon chips (1.2 cm) were cleaned by first sonicating in acetone at 40 °C for 5 minutes followed by deionised water at 60 °C for 5 minutes in order to remove any surface impurities, before being dried at 160 °C for 30 minutes. Photoresist was applied via spin coating by spinning at 700 rpm for 10 seconds followed by 4200 RPM at 40 seconds to produce a film with a thickness of approximately 1.4 $\mu\mathrm{m}$ (Figure 2.10A). During the spin coating process an edge bead can form which is a heightened region of photoresist at the edge of the substrate. This edge bead can become a problem if not removed as it can cause a gap to form between the photomask and sample during lithography often causing poor resolution. To remove this, a 1 cm photomask is used to mask the centre of the sample whilst leaving a 0.1 cm edge (Figure 2.10B). This is then exposed for 40 seconds and developed for 1 minute. Any remaining edge bead is then manually scraped and the sample rinsed in deionised water to leave a clean area around the central photoresist (Figure 2.10C). In this design the silicon is utilised as a global back-gate and in order to make contact with this, the oxide must be removed and a conductive layer deposited. The chips are dipped in buffered oxide etch (6:1) for 1 minute before being rinsed in running deionised water.

Figure 2.9: The Edwards 306 e-beam evaporator used for this research.

They are then placed into an Edwards 306 e-beam evaporator pictured above in figure 2.9 and pumped down to a pressure of 6 x10^{-6} bar. Titanium was used as an adhesion layer and was deposited at a rate of 0.18 $\mathrm{nm/sec}$ until a thickness of 10 nm is formed. Silver was then deposited at a rate of 0.4 $\mathrm{nm/sec}$ until a thickness of 50 nm is formed (Figure 2.10D. A lift-off process was then used by sonicating the chip in N-Methyl-2-pyrrolidone (NMP) at 60 °C for 10 minutes, Isopropyl alcohol (IPA) at 60 °C for 5 minutes and deionised water at 60 °C for 5 minutes in order to remove the remaining photoresist (Figure 2.10E).

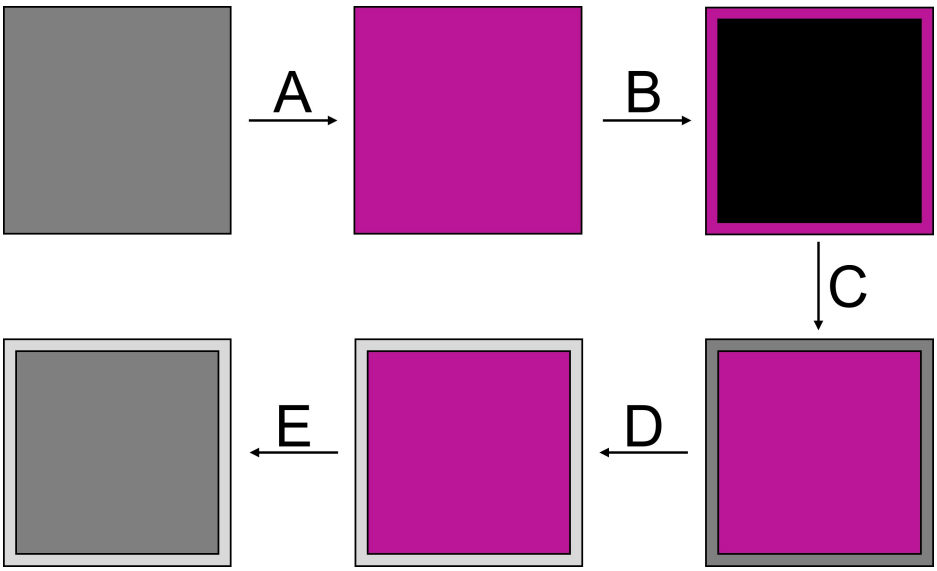

Figure 2.10: The preparation of the global back-gate. (A) Photoresist is applied to the entire chip to a height of around 1.4 μm. (B) The edge of the chip is exposed for 40 seconds to UV light whilst the centre is masked. (C) Photoresist is removed from the edge of the chip. (D) The silicon oxide is removed from the edge of the chip by being exposed to buffered oxide etch (6:1) and then Ti/Ag is evaporated. (E) The photoresist is removed from the centre to leave a 25 nm silicon oxide gate. The silver acts as a bridge to the conductive silicon global back-gate.

The TFT utilises the 25 nm oxide layer to act as an insulating layer therefore the next stages were to add a source and drain which was achieved by using image reversal lithography. A layer of photoresist was applied as mentioned in the last paragraph and the edge beading removed (Figure 2.11F). From here the pattern required was aligned with the centre square created in the last step and a drop of decane was applied to the chip before it was exposed for 5 seconds. Decane is an immersion liquid used to improve the resolution of the lithography as the refractive index matches that of the UV light, therefore minimising unwanted scattering. The samples were then left for 15 minutes to allow the evaporation of the decane and then hard baked at 105 °C for 8 minutes. After this the samples were exposed again for 12 seconds unmasked and developed for 1 minute (Figure 2.11G). The metal probes were then deposited in which titanium and silver were used. Silver was selected due to the higher conductance shown when compared to other metals such as gold and copper.

The titanium was deposited at a rate of 0.18 nm/sec for a thickness of 20 nm followed by the deposition of silver at a rate of 0.4 nm/sec for a thickness of 100 nm (Figure 2.11H). The

lift-off process was then repeated as mentioned earlier to remove the photoresist (Figure 2.11I). The final step is the deposit the DNA-templated nanowires in which 10 μL of the solutions were drop-cast onto the samples and allowed to dry. This was repeated 4 more times so each chip has 5 layers of material present (Figure 2.11J).

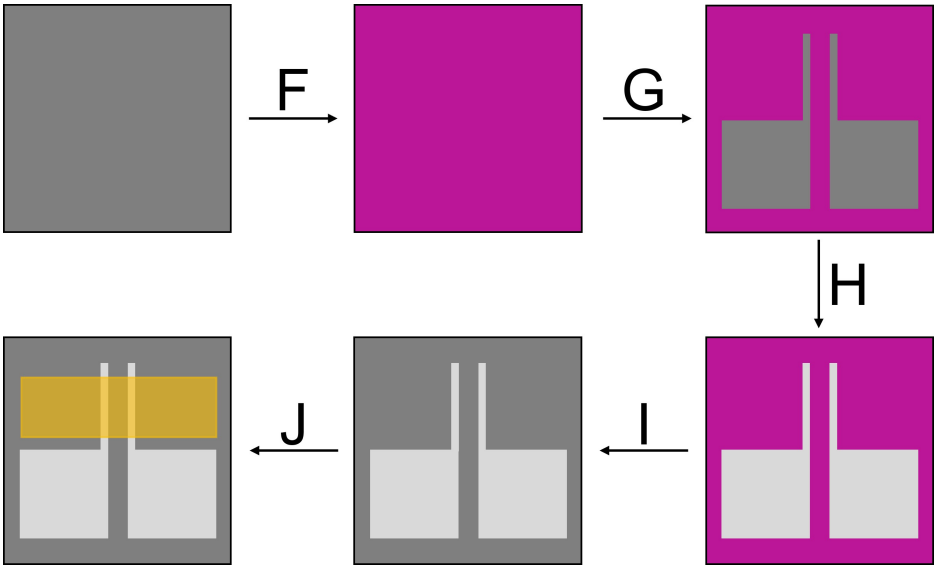

Figure 2.11: The preparation of the source and drain. (F) Photoresist is applied to a thickness of 1.4 μm. (G) The source and drain are patterned into the photoresist. (H) Negative photolithography is used to remove the photoresist from the source and drain pattern before Ti/Ag is deposited. (I) The remaining photoresist is removed. (J) the semiconducting material is applied to the devices by via drop-casting.

Figure 2.12 shows an example of the devices prepared; each contact point is a 100 μm square the source and drain 'fingers' are 25 μm long and 10 μm wide with the inter-electrode gap ranging from 2 - 10 μm.

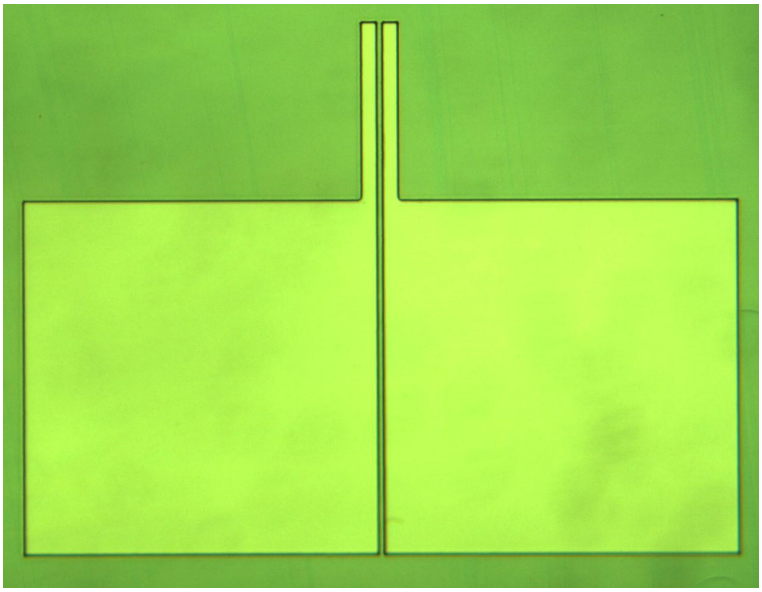

Figure 2.12: An example of the source and drain prepared through negative photolithography. This example shows a 2 μm gap between the source and drain.

Various top contact designs were originally attempted due to the better connection between the source and drain when they are evaporated directly onto the material. The main problem with this was the gate dielectric since the normal way of growing a thin SiO_2 layer was not possible therefore polyimide was used as a 'spin on' gate dielectric. For this preparation the silicon chips were prepared as stated above and the nanowires drop cast and allowed the dry before the source and drain were evaporated on using the same procedure as the bottom gate, bottom contact design. The polyimide (PI-255) was then applied via spin coating (2 x 700 rpm for 10 secs followed by 4200 rpm for 40 secs) before the gate was deposited. The minimum thickness of polyimide possible by this method was 1.2 mm which was too thick for the gate voltage to affect the source - drain current.

Bibliography

[1] L. Dong, T. Hollis, B. Connolly, N. Wright, B. Horrocks and A. Houlton, *Advanced Materials*, 2007, **19**, 1748–1751.

[2] Q. Ye, X. Xu, A. Paghi, T. Bamford, B. R. Horrocks, A. Houlton, G. Barillaro, S. Dimitrov and M. Palma, *Advanced Functional Materials*, 2021, **31**, 2105719.

[3] G. Binnig, C. F. Quate and C. Gerber, *Physical Review Letters*, 1986, **56**, 930–933.

[4] C. Putman, K. Van Der Werf, B. De Grooth, N. Van Hulst and J. Greve, *Biophysical Journal*, 1994, **67**, 1749–1753.

[5] K. Xu, W. Sun, Y. Shao, F. Wei, X. Zhang, W. Wang and P. Li, *Nanotechnology Reviews*, 2018, **7**, 605–621.

[6] Q. Zhong, D. Inniss, K. Kjoller and V. B. Elings, *Surface Science Letters*, 1993, **290**, L688–L692.

[7] M. Bockrath, N. Markovic, A. Shepard, M. Tinkham, L. Gurevich, L. P. Kouwenhoven, M. W. Wu and L. L. Sohn, *Nano Letters*, 2002, **2**, 187–190.

[8] C. Staii, A. T. Johnson and N. J. Pinto, *Nano Letters*, 2004, **4**, 859–862.

[9] R. E. Dinnebier and S. J. L. Billinge, *Powder Diffraction: Theory and Practice*, Royal Society of Chemistry, 2008.

Chapter 3

Preparation, Characterisation and Transistor Behaviour of Vanadium Dioxide-DNA Nanowires

3.1 Introduction

Vanadium oxides present a fascinating and promising class of nanomaterials that have garnered significant attention in recent years due to their unique properties and potential applications.[1–3] Their remarkable electronic, optical, and thermal properties make them a subject of intense research across various scientific disciplines, including materials science, nanotechnology, and electronics.[4–6] Vanadium oxide nanowires owe their exceptional properties to their unique crystal structures, which can be tuned by varying their synthesis methods and conditions.[7] These nanowires often exhibit distinct phase transitions, resulting in intriguing phenomena such as metal-insulator transitions and thermochromism.[8,9] These properties have led to their extensive use in various technological applications.

This chapter focuses on the chemical and electrical properties of novel VO_2-DNA nanowires that have been prepared through a templating reaction. The material has been fully chemically characterised using spectroscopic methods such as UV-Visible spectroscopy, Fourier transform infrared spectroscopy, powder X-ray diffraction and X-ray photoelectron spectroscopy. The structure of VO_2-DNA was has then been investigated using both atomic and electrostatic force microscopy. The structure of VO_2-DNA was then investigated using both atomic and electrostatic force microscopy. After a full chemical characterisation, the electronic properties of VO_2-DNA were investigated using temperature-dependent 2-terminal IV measurements. Finally the VO_2-DNA has been integrated into a novel field effect transistor design and tested for transistor-like behaviour.

3.2 Results and Discussion

3.2.1 Preparation of DNA-Templated Vanadium Dioxide Nanowires

The preparation of VO_2-DNA nanowires employed a combination of two methods; the hydrothermal synthesis of VO_2 as used by Liu and a DNA templating protocol adapted from that used for CdS by Dong.[10,11]

$VO_2$was prepared via the reduction of V_2O_5 using oxalic acid. 191 mg of V_2O_5 (1.05 mmol) was added to a 35 mL H_2O:acetone (5:2) solution. This was followed by 397 mg of oxalic acid ($C_2H_2O_4$, 3.14 mmol). The flask was then evacuated and left stirring for 18 hours at 40 °C during which time the solution colour had changed from bright orange to light blue. The solution was allowed to cool to room temperature before 100 μL of λ-DNA (500 $\mathrm{ng}\ \mu\mathrm{L}^{-1}$) was slowly added and allowed to stir for 24 hours. The solution was transferred to a Teflon-lined steel autoclave (4 cm diameter, 125 cm^{-3} volume) and heated to 180 °C for 24 hours and allowed to cool naturally to room temperature. The solution was then filtered and the black precipitate was kept and washed with H_2O and acetone.

Finally. to prepare VO_2-DNA solutions 5 mg of the precipitate was added to 500 μL of deionized H_2O, mixed vigorously before being left for a further 24 hours after which the solution was centrifuged for 5 minutes and the supernatant removed and stored.

3.2.2 UV-Visible Absorbance Spectroscopy

UV-Vis absorption spectroscopy is an important and simple method to characterise the optical properties and electronic states of a material. In particular, DNA is well known to have no absorption at wavelengths longer than about 300 nm. The lack of absorption above 300 nm means that materials, templated on the DNA, with an optical gap less about 4.1 eV can be studied simultaneously.

UV-Vis samples were measured between 240 - 800 nm using a Thermo Scientific NanoDrop One MicroVolume spectrometer at room temperature. VO_2-DNA samples were measured in a 1 cm path-length cuvette using deionised water as a background. They were prepared for the measurement by mixing 1 mL of VO_2-DNA with 2 mL of deionised water.

Figure 3.1 below shows UV-Vis spectra for VO_2-DNA and VO_2. There is a peak at 260 nm in both spectra; this can be assigned to a charge transfer transition between the vana-

dium (IV) and oxygen atoms in a tetrahedral coordination geometry.[12] The peak at 260 nm is slightly larger and more pronounced for VO_2-DNA when compared to the similar peak present in VO_2. This is likely to be due to the presence of DNA which also shows a characteristic peak at around 260 nm.[13] Such an absorption peak originates from the $\pi \rightarrow \pi^*$ transition of the nucleobase systems of pyrimidine and purine. Guanosine absorbs at 253 nm and cytidine at 271 nm, causing the peak to be broadened with the centre at 260 nm for polymeric DNA.[14] DNA does not show any absorbance at wavelengths greater than about 300 nm therefore the absorption feature near 400 nm is associated with the VO_2 within the sample. Interestingly, this is feature is more prominent in the DNA-templated material.

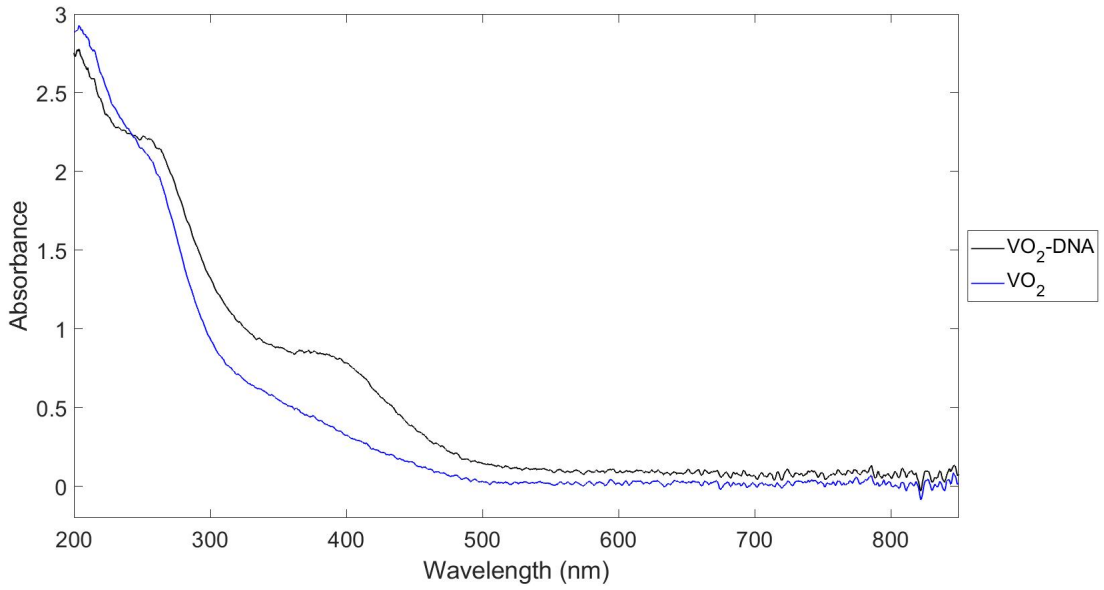

Figure 3.1: UV-Vis spectra of aqueous samples of VO_2-DNA (black line) and VO_2 with no DNA involved (blue line).

As well as characterising the final VO_2-DNA sample, UV-Vis spectroscopy was useful for observing the intermediate species as the reaction progressed because of the change in oxidation state from V(V) to V(IV):

$$V_2O_5 + \text{oxalic acid} \rightarrow VO_2^+ \rightarrow VO_2$$

Figure 3.2 shows the spectra for the starting orange V_2O_5 dispersion, the blue intermediate species $VO_2{}^{2+}$ and the end VO_2-DNA product. The starting mixture of reagents was a brick orange colour and shows a peak at around 440 nm. The spectrum shows a long tail

which extends across the full visible spectrum. This can be explained due to the fact that the V_2O_5 is a suspension and the tail is elastic scattering of light caused by the V_2O_5 particles within the suspension. As the reaction proceeds the starting V_2O_5 is reduced to VO_2 by oxalic acid via the intermediate species VO_2^+ which forms a light blue solution in which a peak can be found at around 750 nm. The resulting product of the VO_2-DNA is a pale yellow solution and we can see a peak at 400 nm showing a lack of starting or intermediate product present within the final solution.

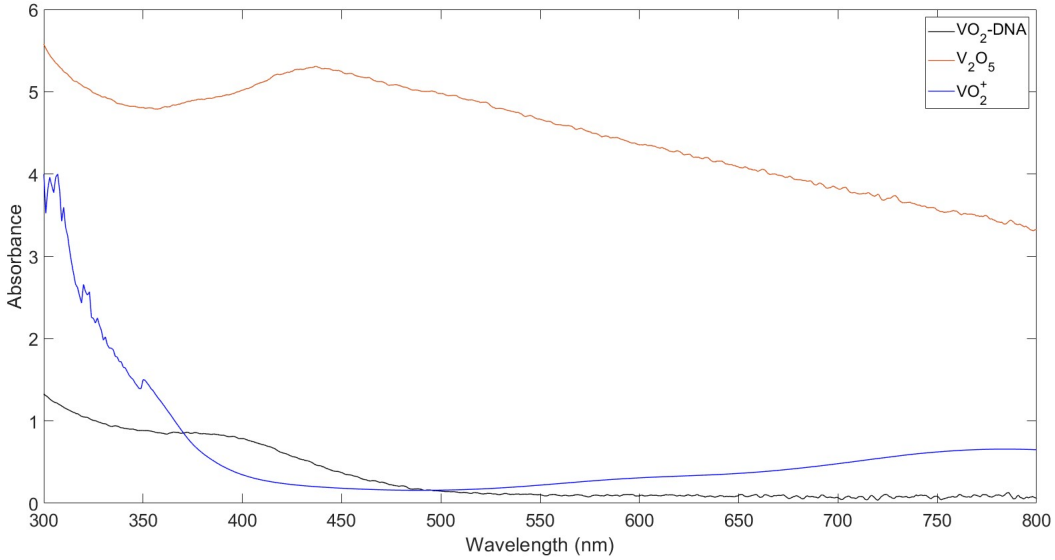

Figure 3.2: UV-Vis spectra of VO_2-DNA (black), V_2O_5 (orange) and VO_2^+ (blue) to show the difference between the starting reagents and final product.

UV-Visible spectroscopy in this research indicates a presence of DNA in the VO_2-DNA sample due to the larger peak at 260 nm. It can also be used as a simple check to confirm the reduction of V(V) to V(IV) is occurring.

3.2.3 Fourier Transform Infrared Spectroscopy

FTIR is a commonly analytical method which is often used to to characterise functional groups and can also be used to find information on the nature of the bonding within a compound. The main reason FTIR was chosen as a technique was to evaluate the differences between VO_2-DNA and bare DNA.

For aqueous samples of VO_2-DNA a background was recorded using a clean silicon wafer

after the instrument had been purged with nitrogen. The VO_2-DNA was then dropcast onto the silicon and allowed to dry, after which the spectra obtained. For powder samples, an attenuated total reflectance (ATR) attachment was used. The instrument was again purged with nitrogen before a background reading was recorded, after which the desired spectra was obtained.

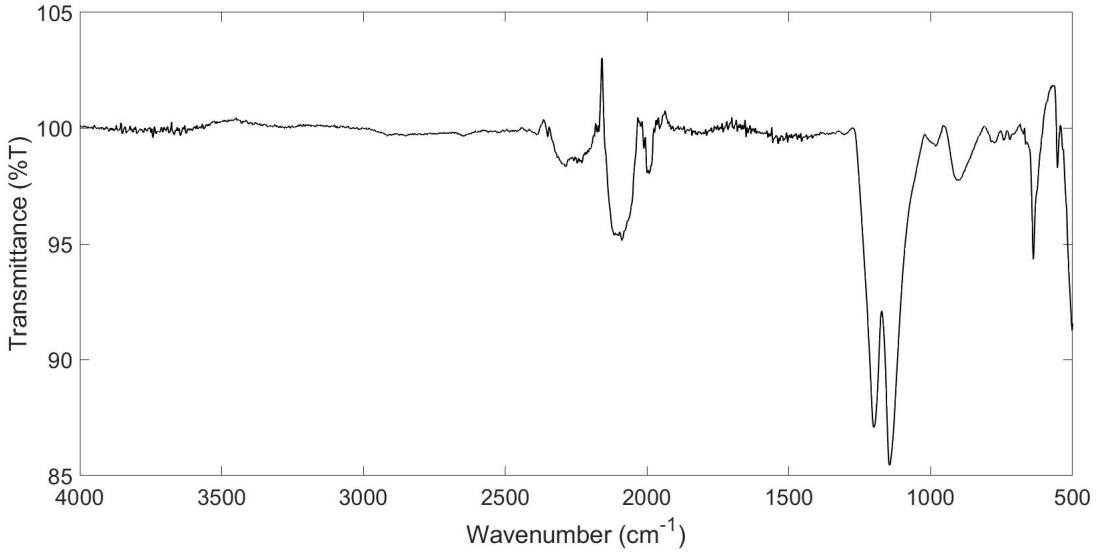

Figure 3.3: FTIR transmission spectra of VO_2-DNA. The spectra was collected over 50 scans at 4 cm^{-1}

Figure 3.3 shows the Fourier Transform Infrared Spectrum (FTIR) of the prepared VO_2-DNA. The peaks from 1900 - 2350 cm^{-1} are due to a difference in CO_2/H_2O levels between the background and sample. The structure of VO_2 (B) is shown below in figures 3.4 and 3.5 and contains VO6 octahedral units with some shared edges (V-O-V moieties) and some oxygens coordinated to one vanadium (V=O). Broad peaks at 982 and 898 cm^{-1} can be assigned to stretching V=O bonds on an octahedral structure.[15] The 982 cm^{-1} peak is slightly shifted from 1020 cm^{-1}. The sharp band at 638 cm^{-1} could be related to hydrogen bonding between the oxygens of the vanadyl group.[16] The final absorption band associated with the VO_2-DNA is at 554 cm^{-1} and can be attributed to V-O-V octahedral bending modes.[17]

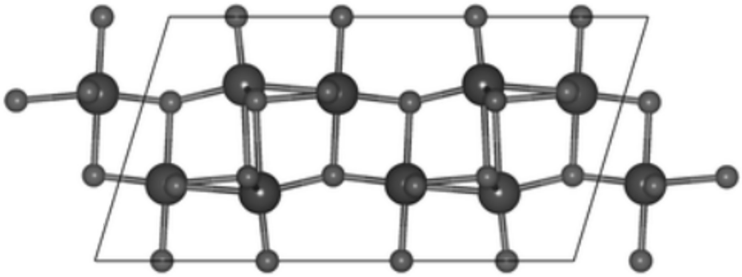

Figure 3.4: The crystal structure of VO_2 (B) as discovered by Oka[26] and then drawn by Corr.[27] VO_2 adopts a monoclinic structure C2/m. The large, dark grey spheres represent vanadium and the smaller, light grey spheres represent oxygen. Each vanadium atom is coordinated to 6 oxygens, one hidden behind each vanadium in the diagram. Neighbouring vanadium atoms share two oxygens, i.e. there is an edge in common between neighbouring VO6 units.

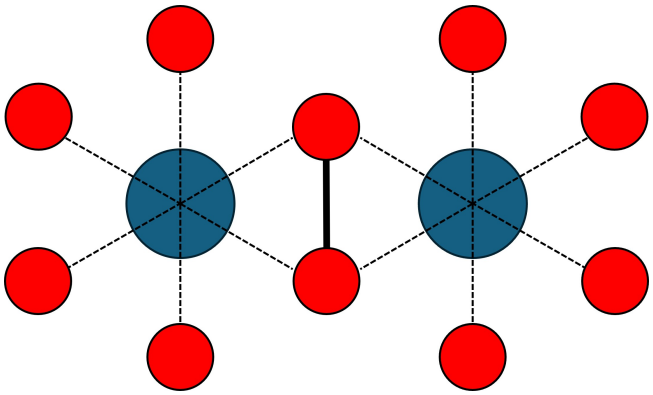

Figure 3.5: Illustration of two VO6 octahedra with a shared edge (bold line). Red = oxygen, blue = vanadium. Dotted lines indicate the coordination shell of the vanadium ions.

The two peaks 1139 and 1203 cm^{-1} can be assigned to stretching, symmetric and asymmetric PO_2^- on the deoxyribose backbone of the DNA.[18] These peaks are shifted from the previously reported values of 1123 and 1331 cm^{-1} respectively, indicating there is a change within the bonding of PO_2^-.[19] This change in band position suggests coordination of the vanadium to the phosphate which in turn suggests that the VO_2 is templated on the DNA and not simply mixed in solution with it.

Wavenumber (cm^{-1})	**Assignment**
554	V-O-V Octahedral bending
638	V-O hydrogen bonds
898	V=O Octahedral bending
982	V=O Octahedral bending
1139	PO_2^-
1203	PO_2^-
1900 - 2350	CO_2/H_2O Miscancellation

Table 3.1: An overview of the peak assignments found from the FTIR for VO_2-DNA[20–22] The structure of the B polymorph of VO_2 contains edge and corner sharing irregular VO_6 octahedrons.[32]

FTIR was also used in order to compare the final VO_2-DNA sample and the starting materials of V_2O_5 (+30 %T) and oxalic acid (+60 %T) as seen in figure 3.6. The two main peaks for V_2O_5 are at 812 and 1000 cm^{-1} of which the former can be assigned to V-O-V symmetric stretch and the latter to the V=O symmetric stretch.[23,24] When compared to the same peaks for VO_2-DNA a small shift can be found indicating a slight change in the bonding possibly due to the presence of DNA. A clear indicator there is no remaining oxalic acid is the lack of a carbonyl peak at 1685 cm^{-1}.

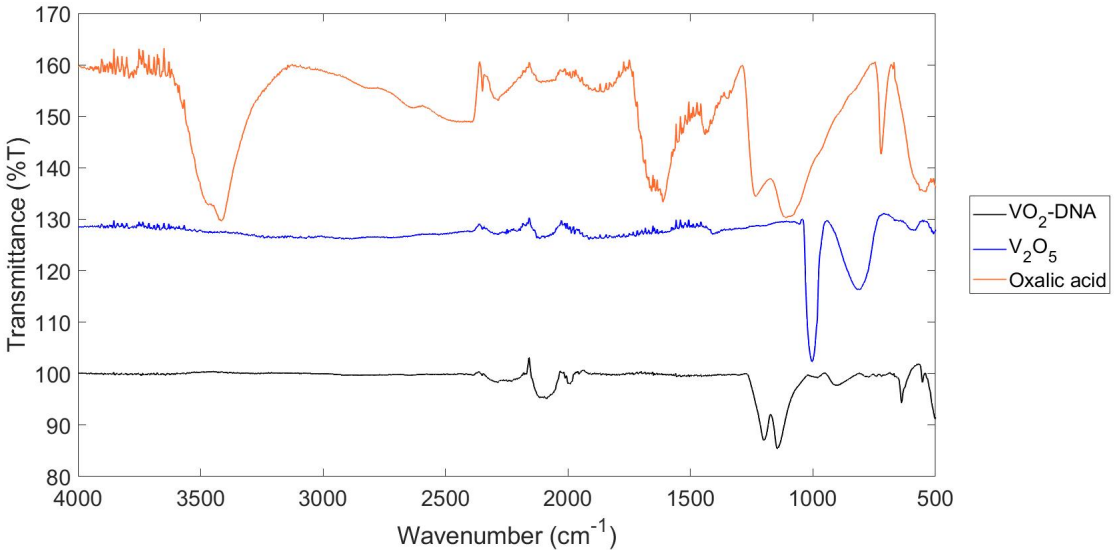

Figure 3.6: FTIR spectra of VO_2-DNA (black), V_2O_5 at +30 %T (blue) and oxalic acid +60 %T (orange)

The FTIR conducted shows there is a distinct difference between λ-DNA and the DNA present in VO_2-DNA showing that there is a potential interaction between the DNA and V and the sample is not just a mixture of the two. It has also been used to prove the lack of starting reagents within the end product.

3.2.4 Powder X-ray Diffraction

Powder XRD demonstrated that VO_2 had been prepared and to deduce the phase and structure. It was then also used to check for any differences between samples that had DNA present and those that did not. The VO_2-DNA was suspended in methanol and transferred to a zero-background holder. A preliminary scan was measured to determine the location of all the diffraction peaks before a higher resolution scan was run. The 2θ range: 10 - 90°, step size: 0.0334°, time per step: 12 s. Soller slit: 0.04 rad, beam mask: 20 mm and slit 2 = 0.5°.

A comparison between VO_2-DNA and VO_2 is shown below in figure 3.7 in which it can be seen that the two patterns are identical to one another and match closely to a past example of VO_2 'nanorods' which have also been produced using this methodology.[25] This also shows the lack of contamination from other vanadium oxide phases or general impurities.

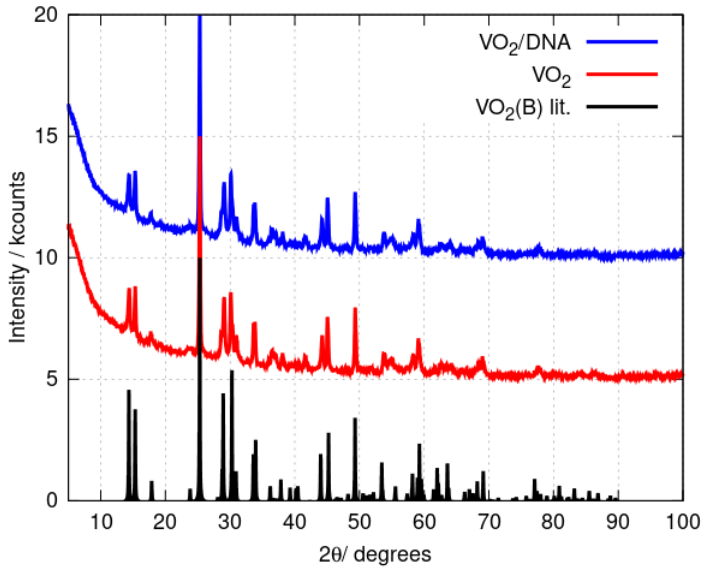

Figure 3.7: pXRD patterns of VO_2-DNA (blue), VO_2 with no DNA involved (red) and literature VO_2 (B) nanorods (black). The intensities of VO_2-DNA and VO_2 have been increased by 5 in order to better see the patterns.[25]

Table 3.2 shows the lattice parameters of the measured sample which are in agreement with the reported values (JCPDS Card No. 31-1438). The three vectors(a,b and c) form the edges of the parallelepiped unit cell. The angles between the vectors form α, β and γ in which α is the angle between b and c, β is the angle between a and c and γ is the angle between a and b. For a system to be classed as monoclinic α and γ must be equal to 90.

Crystal System	Monoclinic
Space Group	C 2/m
Space Group Number	12
a ($\mathring{A}$)	12.0300
b ($\mathring{A}$)	3.6930
c ($\mathring{A}$)	6.4200
α (°)	90.0000
β (°)	106.1000
γ (°)	90.0000

Table 3.2: The unit cell details found from the pXRD of VO_2-DNA. The cell parameters match those of VO_2 reported previously.[28]

The pXRD conducted here shows that the sample produced matches near identically to that of VO_2 nanorods, indicating that VO_2 nano systems are present and that they are in the B phase.

3.2.5 X-ray Photoelectron Spectroscopy

XPS can be used to analyse the chemical composition, as well as the oxidation state of a material. It was utilised in this area of research in order to find any potential differences in the binding energy of vanadium when it is templated to DNA, compared to plain VO_2.

VO_2-DNA samples were prepared in two ways for X-ray photoelectron spectroscopy (XPS) in order to compare the black precipitate formed during the autoclave stage and the aqueous solution prepared from the precipitate. For the black precipitate, a thin layer of powder was applied to a carbon tape tipped metal stub which was then used for all measurements. The aqueous samples were first dropcast onto clean silicon wafers and allowed to dry before being attached to carbon taped tipped metal stubs. The samples were measured using a monochromic Al Kα X-ray excitation source of a Thermo Scientific K-Alpha X-ray photoelectron spectrometer with a 30 - 400 $\mu\mathrm{m}$ spot size with 5 $\mu\mathrm{m}$ steps. The photoelectrons were filtered with a hemispherical analyser and the measured with a multichannel detector. To eliminate electrostatic charges on the surface of the sample a dual beam neutralisation gun was used. The calibration for the vanadium samples was done using the Au 4f peak at 84 eV and the CdS-CNT-DNA samples were calibrated using the C 1s peak at 284.8 eV.

Figure 3.8 shows the V 2p spectra for VO_2-DNA on the left and VO_2 with no added DNA on the right. The energy scale was calibrated using the Au 4f peak at 84 eV. Four components were chosen for fitting the XPS spectra to model both the V(IV) and V(V) present within the samples. The presence of V(V) can be explained by the oxidation of the surface vanadium before the measurement was recorded and had to be accounted for whilst fitting. The large peak from around 514 - 518 eV corresponds to the V $2p_{3/2}$ split which can then be further separated into V(V) and V(IV). The V(IV) peak for VO_2-DNA has been fitted to a value of 515.92 eV which is 0.05 eV lower than that of plain VO_2 at 515.87 eV. This small shift could indicate that the vanadium is being effected by the DNA and provides some evidence that an interaction is occurring. When PO_2^- is coordinated

to V(IV) the binding energy of the electrons in V 2p could be lowered by the electrostatic effect of the negative charge. The V $2p_{1/2}$ also supports this statement with the VO_2-DNA V(IV) peak having a fitted value of 522.73 eV compared to the VO_2 (IV) peak at 523.12 eV, a difference of 0.39 eV.

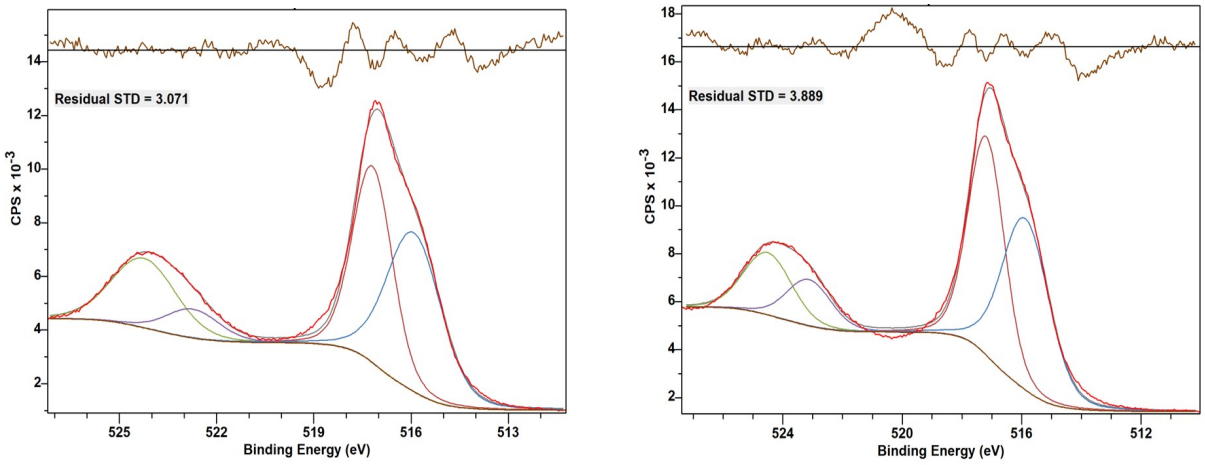

Figure 3.8: V 2p spectra for VO_2-DNA (left) and VO_2 (right). The red curves show the experimental data and the others are fitted components. The residual fit is shown on the top of each spectra.

Overall the XPS conducted shows a difference in binding energy between plain VO_2 prepared without DNA and the sample of VO_2-DNA which indicates that the V in the VO_2-DNA is in a different environment than the control. This could be due to the binding of the V to the phosphate backbone of the DNA.

3.2.6 Atomic Force Microscopy

The structure of the prepared VO_2-DNA was further investigated using tapping mode AFM. Samples were prepared for atomic force microscopy by first diluting them by a factor of 10^4. Silicon chips were used as a substrate for VO_2-DNA in which they were first sonicated in deionised water for 15 minutes followed by 15 minutes sonication in acetone. From here they were then immersed in a 3:1 piranha solution for 1 hour and rinsed under running deionised water. 2 $\mu\mathrm{L}$ of the diluted samples were then dropcast onto the cleaned silicon chips and left to dry in a laminar flow hood before being imaged. The laminar flow hood was used in order to minimise the risk of any outside impurities such as dust being present when an image was recorded.

With bare DNA the expected images would show wire like structures with a height of approximately 2 nm or less as found in figure 3.9. With the samples of VO_2 it was found that larger wires were formed with heights ranging between 4 and 8 nm.

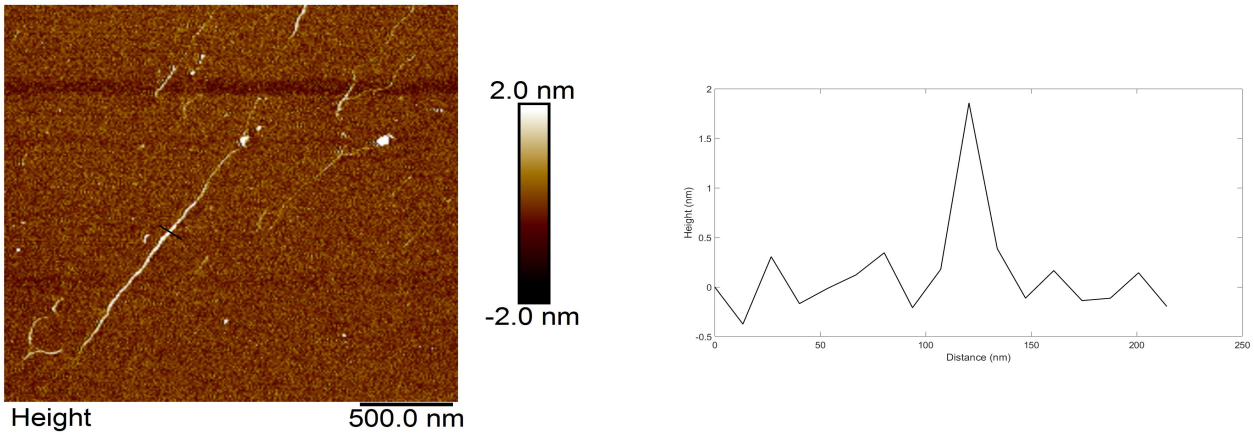

Figure 3.9: AFM image (left) showing bare DNA with the corresponding heigh graph (right). The black line on the AFM image corresponds to the area the height was recorded.

Figure 3.10 shows an example of two wire-like structures formed by VO_2-DNA and the accompanying height graph. This height graph shows the heights of the particles along the wire structure as indicated by the coloured lines within the image. Due to the wires showing heights between 4 and 8 nm they cannot be bare DNA. The height graphs also show the coating is not smooth with a variance of around 1 - 1.5 nm in some areas potentially caused by a lack of nucleation during the growth stage as referenced in 1.2.2.

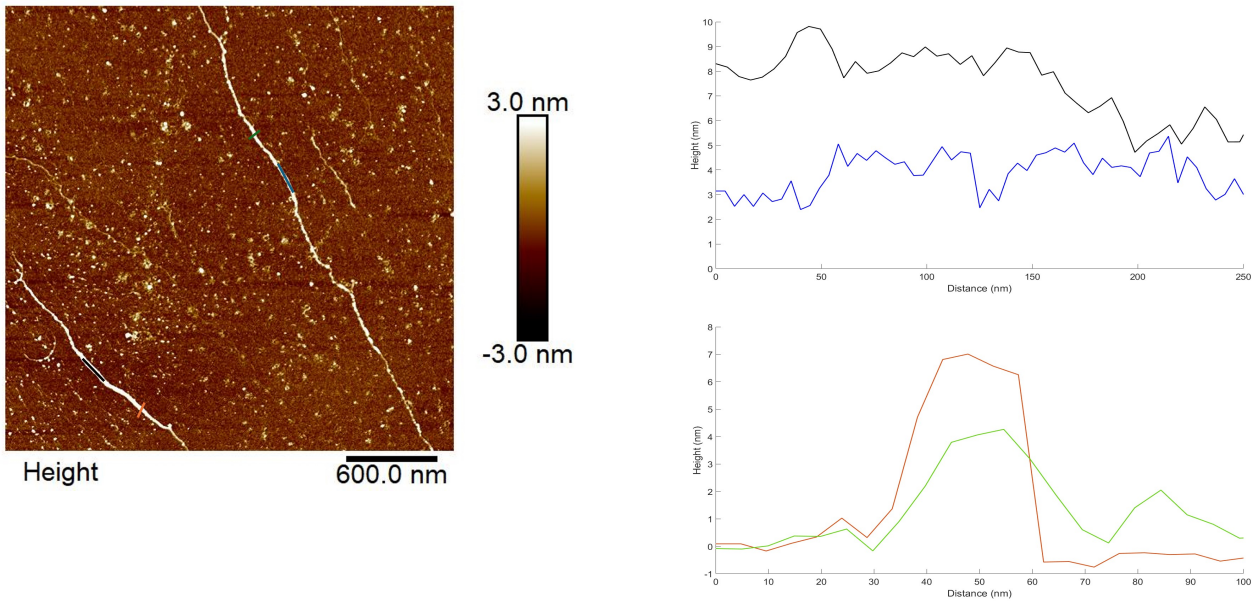

Figure 3.10: AFM image (left) showing VO_2-DNA nanowires with the corresponding length (top) and height (bottom) graphs. The coloured lines on the AFM image correspond to the same colour on the length and height graphs.

Figures 3.11 and 3.12 both show three VO_2-DNA wires that are more uniform in size with heights reaching around 4 - 5 nm. The shortened length of wires compared to the 16 $\mu\mathrm{m}$ DNA used can most likely be explained due to the high temperatures (see section 2.2.1) used during the preparation. If any bare DNA is present during these stages then it is likely that the DNA will denature therefore splitting the larger wires into shorter sections.

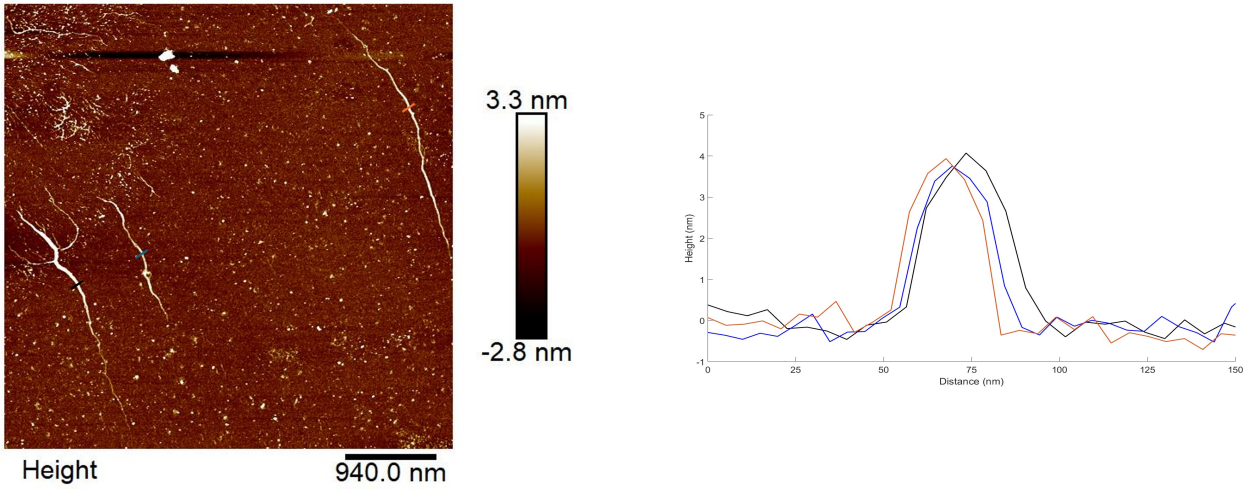

Figure 3.11: AFM image (left) showing VO_2-DNA nanowires with the corresponding height graph (right). The coloured lines on the AFM image correspond to the same colour on the height graph.

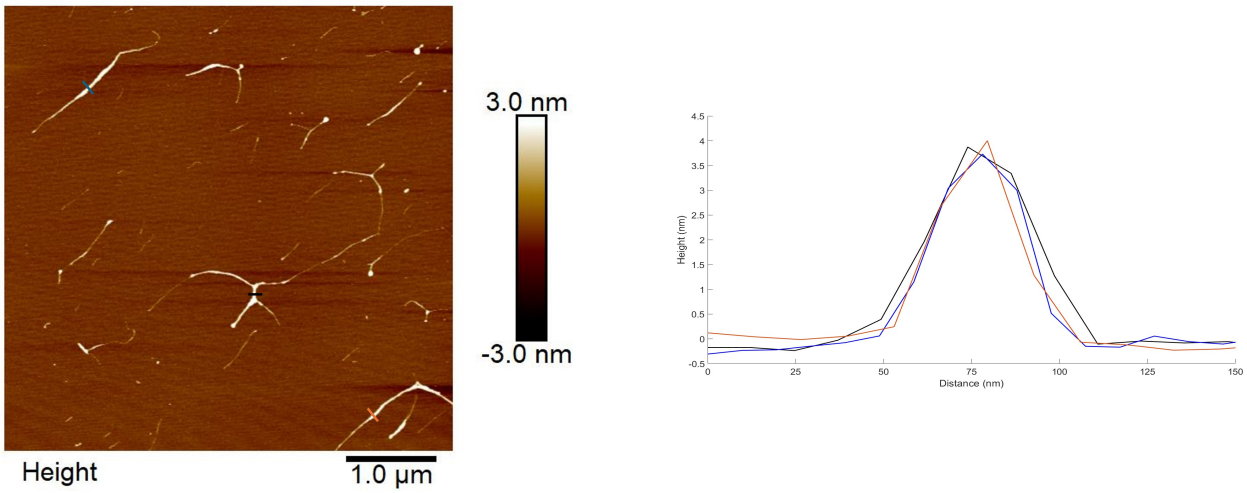

Figure 3.12: AFM image (left) showing VO_2-DNA nanowires with the corresponding height graph (right). The coloured lines on the AFM image correspond to the same colour on the height graph.

Figure 3.13 shows thicker structures of VO_2-DNA with heights ranging from 8 - 12 nm. This is higher than other samples recorded and can be attributed to the formation of rope like structures. This occurs due to the bundling of the VO_2-DNA wires and is commonly found in DNA-templated materials.[29] When compared with the height of bare DNA shown in figure 3.9 the VO_2-DNA wires are upwards of 6x the height which gives a good indication that the DNA is being used as a template.

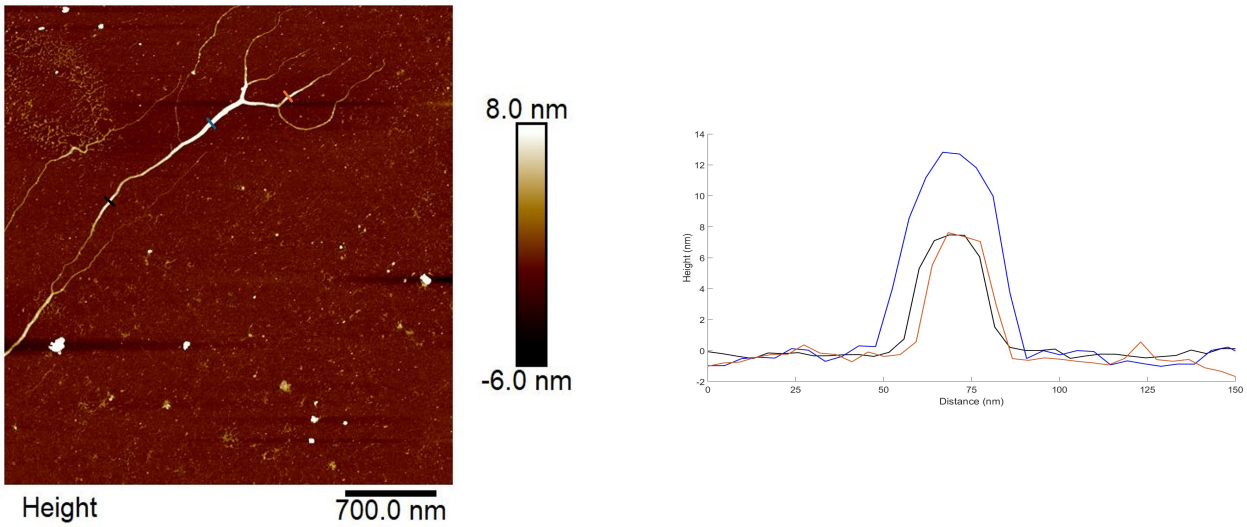

Figure 3.13: AFM image (left) showing VO_2-DNA nanowires with the corresponding height graph (right). The coloured lines on the AFM image correspond to the same colour on the height graph.

The structure of VO_2 without the addition of DNA was also investigated to check for any

similarities or differences and in order to check the DNA was making a difference. Figure 3.14 shows examples of what was found whilst imaging. It was found that in the absence of DNA, small structures with no set geometry were formed compared to the wire like formation shown above when DNA was present. This shows that the DNA helps facilitate the growth of VO_2 nanowires.

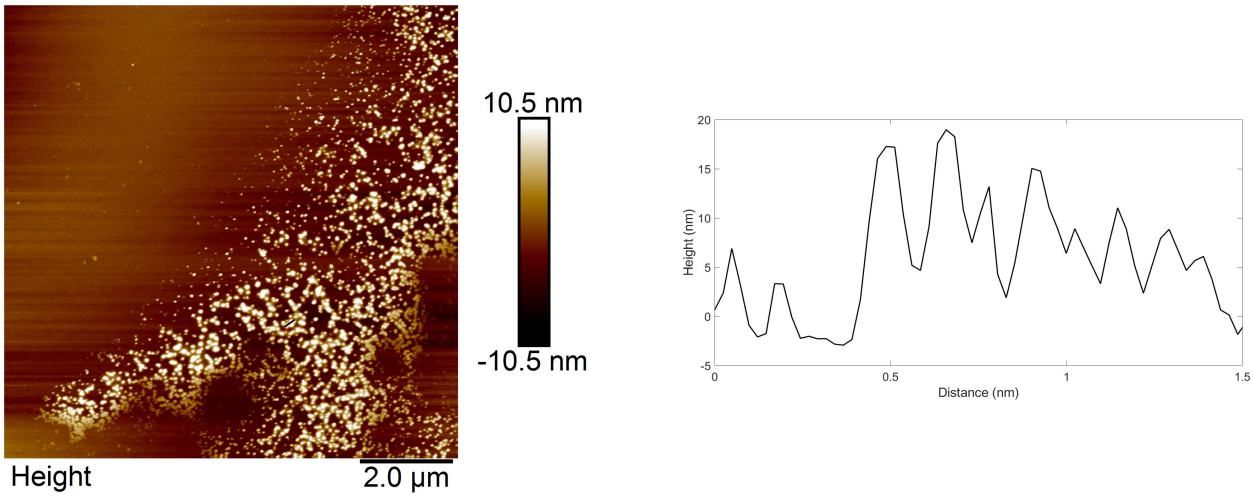

Figure 3.14: AFM image (left) of a sample of VO_2 prepared in the absence of DNA template strands with the corresponding height graph (right). The black line on the AFM image correspond to the area the height was recorded.

The AFM images above show two main points. The first is that nanowires form when the VO_2-DNA is prepared and without the DNA present these wire structures are not present. This shows that the DNA facilitates the growth of nanowires. The second is that the nanostructures in the images can not be bare DNA due to the height of the wires being 3 - 6x larger than the bare DNA found in figure 3.9. In total, 27 measurements were recorded along 9 wire like VO_2-DNA structures in which the average height was 5.83 nm with a standard deviation of 2.62 nm.

3.2.7 Scanned Conductance Microscopy

SCM is a lift mode technique which uses similar principles to electrostatic force microscopy, EFM.[30] However, SCM provides a non-contact, qualitative assessment of the con-

ductance of nanostructures. Figure 3.15 shows two images, the left image shows an AFM image of a VO_2-DNA nanowire and the right image shows the corresponding EFM phase image. This was recorded using the same wire with a $+1$ V bias between the tip and the sample. Images produced by SCM have lower resolution than AFM because (i) the metallised tip has a larger radius and (ii) the SCM effect relies on long-range electrostatic forces. The phase image is related to conductance as explained in section 2.3.4. The darker areas indicate a negative phase shift and a conductive structure.

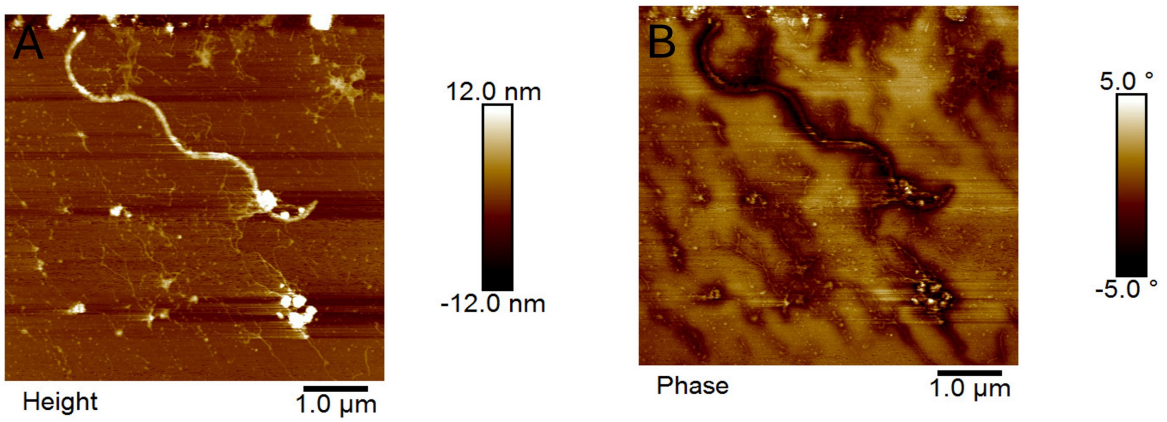

Figure 3.15: Image A shows an AFM image of a VO_2-DNA nanowire. Image B shows the same VO_2-DNA nanowire imaged using EFM with lighter colours showing a more positive phase shift and darker colours showing a more negative phase shift.

By keeping the height of the cantilever constant and varying the bias applied to the tip, a plot of phase shift against bias can be constructed. This is shown in figure 3.16. Importantly, the phase shift observed is independent of the sign of the dc bias applied; this allows the SCM conductance effect to be distinguished from electrostatic effects from trapped charges that typically give a linear dependence on applied bias.

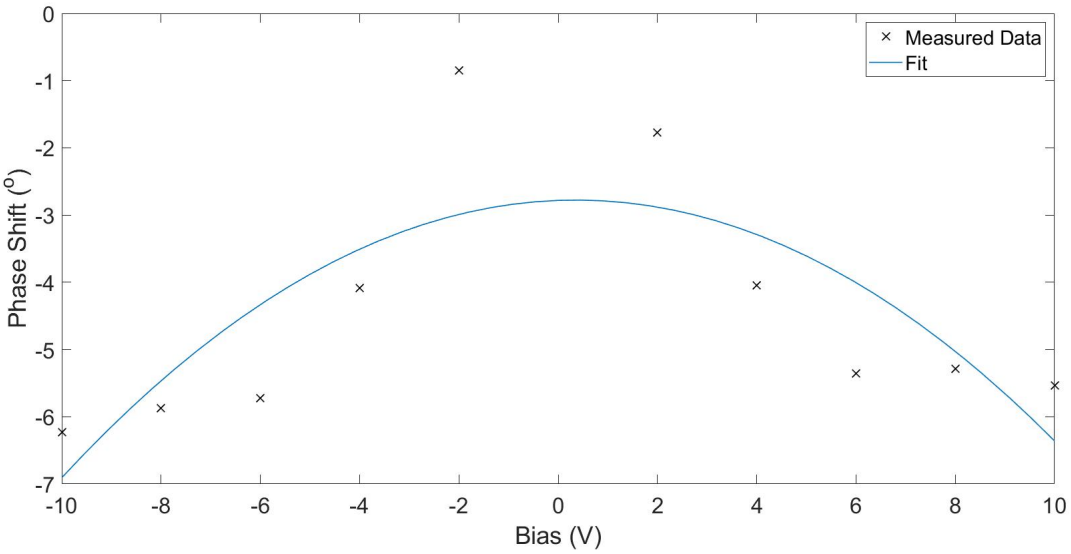

Figure 3.16: The phase shift (°) plotted against the tip bias when varied between -10 - 10 V.

Typically an insulating material will show a positive phase shift and therefore appear bright in an SCM image, whereas a conductive material shows a negative phase shift and appears dark on an SCM image. The pattern in figure 3.15 shows a bright centre with a darker contrast in the centre showing a negative-positive-negative phase profile over 'nanowires' that are weakly conducting and is often observed for weakly conductive materials. The technique is not sensitive to the type of doping and measures the differential conductance at zero bias. The negative-positive-negative phase profile is explained qualitatively by long range interactions between the tip and the nanowire when the tip is not immediately above the nanowire.[31]

Due to the change in phase measured using SCM, evidence has been provided that indicates the VO_2-DNA nanowires imaged could be classed as weakly conductive. The issue with SCM is that it does not allow the conductivity of a sample to be measured quantitatively meaning further electrical measurements were required.

Although SCM is a qualitative technique, the shape of the phase shift diagram indicates that the material is of a weakly conductive nature however this is can only be inferred.

3.2.8 IV Characteristics

In past studies, one of the main issues with DNA-templated materials is their low conductivity, whilst not insulating they generally allow little current to pass through. In order

to thoroughly investigate the electrical capabilities of the prepared VO_2-DNA nanowires, they were first analysed by basic two-terminal IV measurements using an Agilent Technologies B1500A Semiconductor Device Analyzer. The solution described in section 2.2.1 was dropcast as prepared onto 10 and 5 $\mu\mathrm{m}$ IDEs and allowed to dry under vacuum. These are prefabricated electrodes with two connection tracks connecting to micro-fingers with inter-electrode gaps as mentioned above. These were chosen due the 10 $\mu\mathrm{m}$ inter-electrode gap. This gap is shorter than the 16 $\mu\mathrm{m}$ long λ-DNA, meaning it was possible for a single nanowire to span the inter-electrode gap. The IV curves were recorded between -2 to 2 V in steps of 0.2 V at room temperature in a dark nitrogen atmosphere. These conditions were chosen as they allow a controlled environment for every sample. The lack of light excludes any potential photocurrent effects and the nitrogen allows for a dry atmosphere in which stray ionic currents from humidity and condensation forming on the sample are avoided. Figure 3.17 shows an example of the IV curve produced by a sample of VO_2-DNA. In total 12 samples had their IV curves recorded at temperatures between 20 $^{\circ}\mathrm{C}$ - 100$^{\circ}\mathrm{C}$. It was found that the material shows non-ohmic conductivity. As discussed in section 1.7 there are several possible origins for this behaviour. The XRD measurements show that the nanowires are the VO_2 (B) phase which is reported as metallic at room temperature.[32] A true metal would not show such nonlinear behaviour at the low voltages applied, but it is possible that the conduction in the VO_2-DNA nanowires is better described as a hopping process between neighbouring crystallites, similar to that in a grannular metal as explained in section 1.7.3.

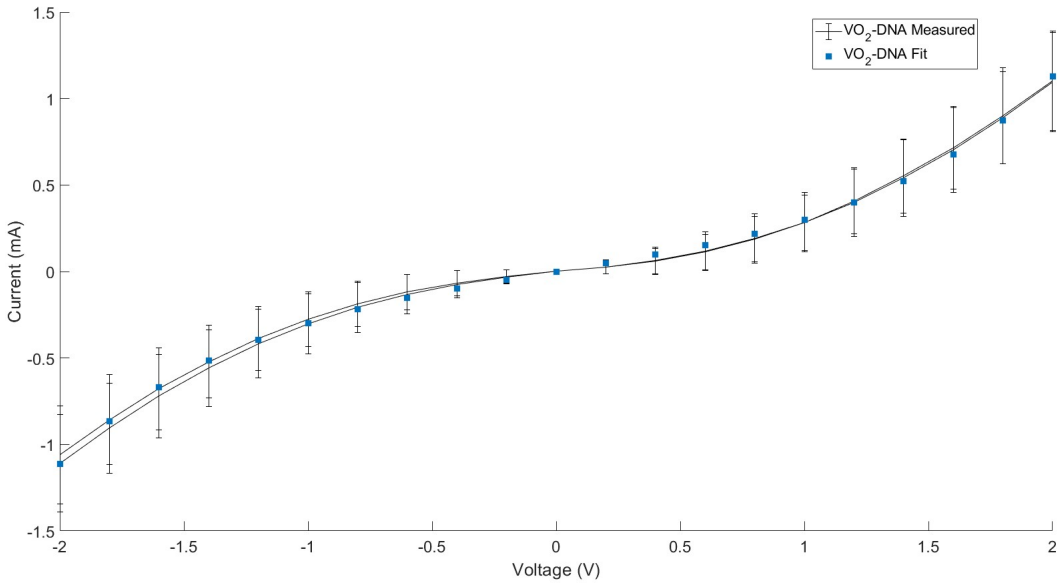

Figure 3.17: IV curve of VO_2-DNA at 20 $^{\circ}\mathrm{C}$ using a 10 $\mu\mathrm{m}$ platinum interdigitated electrode. The blue square indicate fitting using equation 1.23.

The differential conductance at zero bias was determined from the data in figure 3.17 by linear regression of the data over the range $-0.5 < V < +0.5$ V. These conductances were then plotted at various temperatures, found in figure 3.18, in which it can be seen that there is a rise in conductance as the temperature increases. This behaviour is also inconsistent with a true metal, but can be rationalised in the context of a hopping mechanism of conduction.

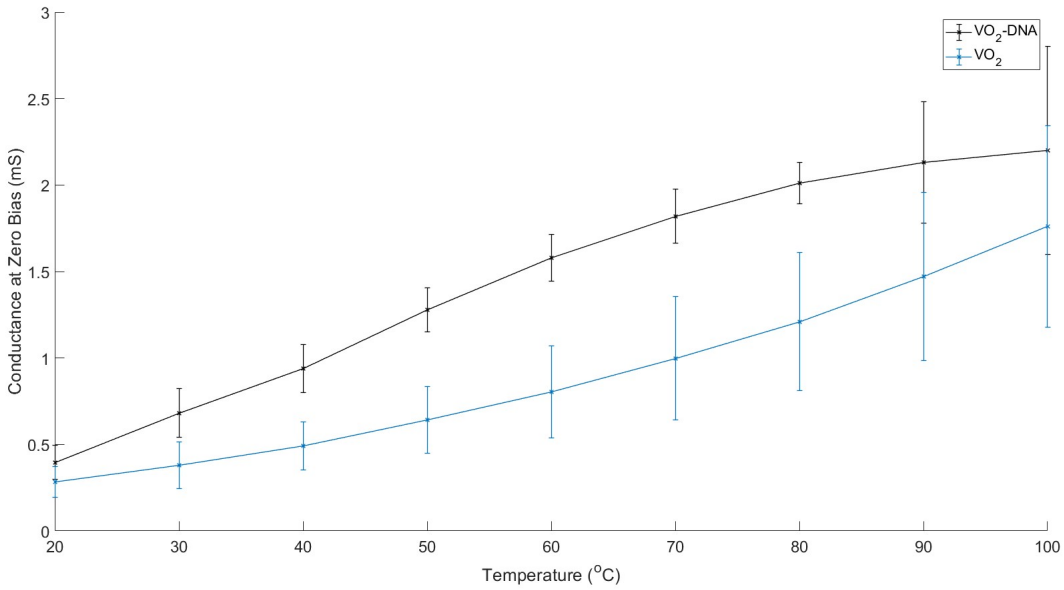

Figure 3.18: A comparison between the temperature dependent conductances at zero bias between VO_2-DNA (black) and VO_2 (blue) over a temperature range of 20 - 100 $^{\circ}\mathrm{C}$.

When comparing the VO_2-DNA sample with a control of VO_2 with the DNA absent, an increase in conductance can be observed as shown in figure 3.18. One of the possible reasons for this is that the wires formed when DNA is present are better at bridging the 10 $\mu\mathrm{m}$ gaps on the interdigitated electrode. The AFM images show that the VO_2-DNA nanowires are continuous over longer distances than the VO_2 samples which consist of many disconnected small particles when deposited on a substrate. This would allow a more direct and efficient pathway for the charge to cross the inter-electrode gap in VO_2-DNA.

A plot of lnG against $1/T$ is shown below in figure 3.19 where G is the zero bias differential conductance. This gives an activation energy of $\Delta E = 0.19\ \mathrm{eV}$.

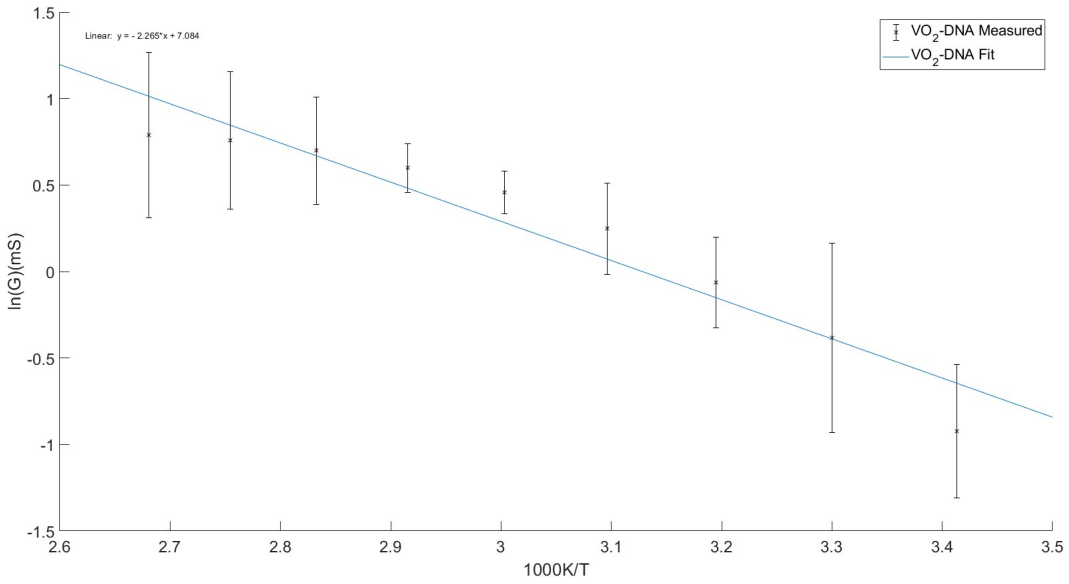

Figure 3.19: An Arrhenius plot for VO_2-DNA. The black crosses show the measured data and the blue line is the computed fit.

The prepared VO_2-DNA nanowires are clearly not behaving as conventional metals, however the mechanism of charge transport in these samples (non-ohmic IV, increase ion conductivity with temperature) can be explained on the basis of a charge transport mechanism in which hopping occurs between between small crystallites. The crystallites themselves may indeed be metallic in nature, but it is proposed that the conductivity is limited by electron transfer between neighbouring crystals.

3.2.9 Sintering Effect

After the measurements at 100 °C had been completed, a room temperature reading was then recorded in which it was noticed the current produced by the sample had increased by around 50 % along with a more ohmic shaped IV as found in figure 3.20.

In order to investigate this, further samples were prepared as mentioned in 2.4.1 and IV curves recorded at room temperature. After this the samples were heated to 150 °C for 2 hours in a vacuum oven before IV curves were recorded again. Figure 3.21 shows the conductance at zero bias before and after this heating step and it can be seen that there are increases in conductance for all 4 samples.

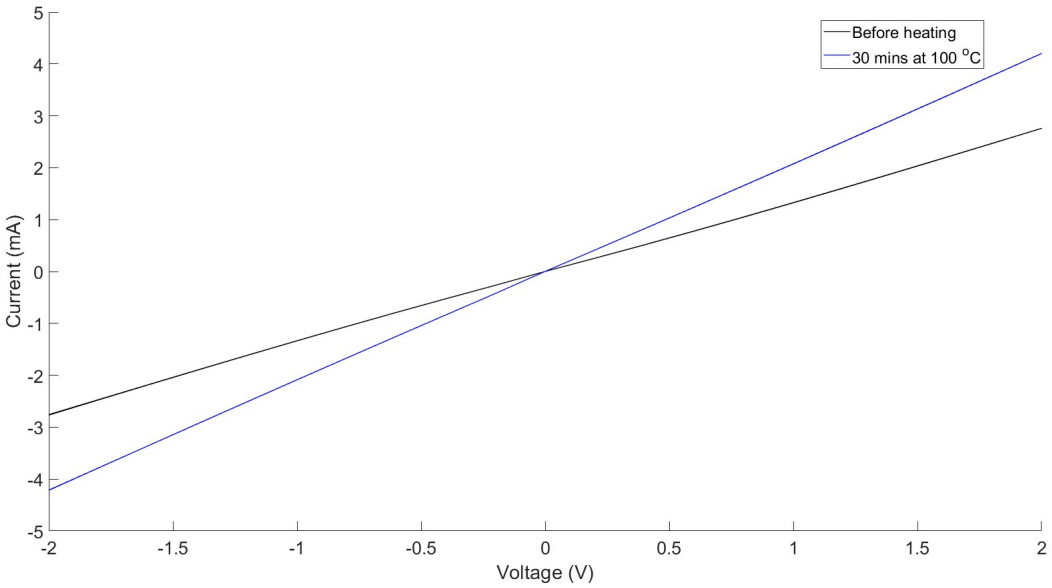

Figure 3.20: A comparison between the IV curves of VO_2-DNA (black) that had been heated to 100 °C for 30 minutes and unheated VO_2-DNA (blue).

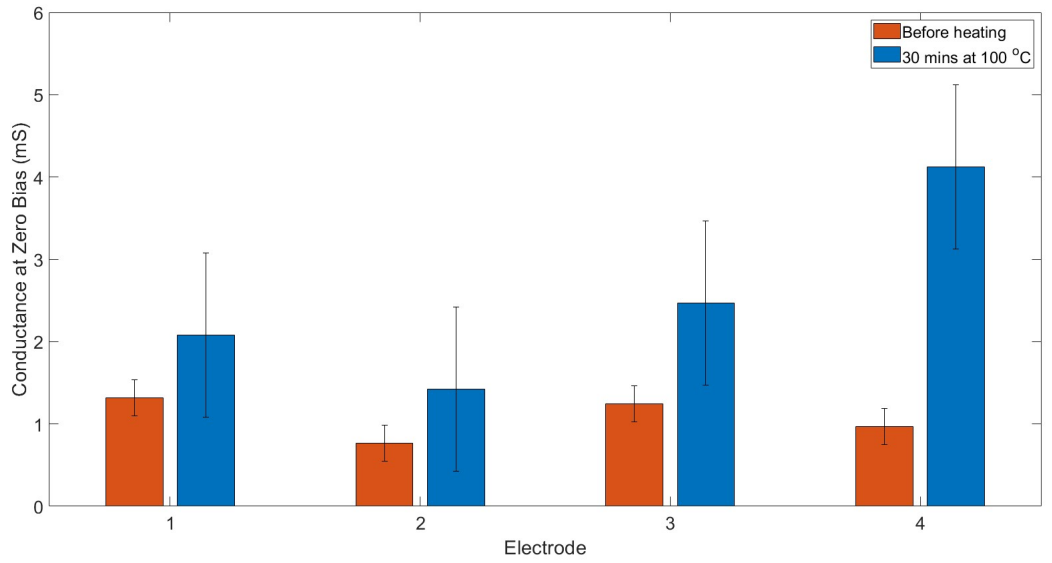

Figure 3.21: A comparison between the conductance at zero bias of VO_2-DNA (orange) that had been heated to 100 °C for 30 minutes and unheated VO_2-DNA (blue). A t test was performed in which a P value of 0.0296 was calculated. By conventional criteria this difference is considered statistically significant.

One possible reason for this is a sintering effect taking place during the heating of the VO_2-DNA samples. Such a process could improve the conductivity by increasing the crystallite size (and reducing the number of crystal-crystal junctions) or by altering the

nature of the junctions so that the states on either side have better overlap. AFM images of the nanowires after heating do show large changes in morphology. There is an overall thickening of the wire like structure from widths of around 25 - 50 nm in figures 3.9 to 3.13 to over 300 nm in figure 3.22.

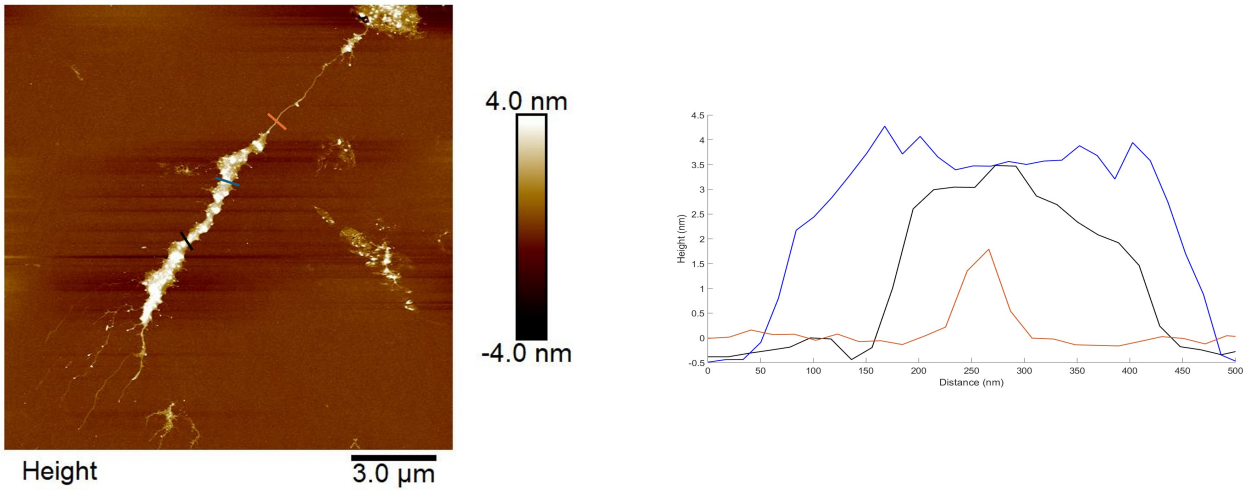

Figure 3.22: AFM image (left) of VO_2-DNA that has been heated for 2 hours at 150 $^{\circ}\mathrm{C}$ with the corresponding height graph (right). The 3 coloured lines on the AFM image correspond to the area the height was recorded.

The sintering of the VO_2-DNA nanowires has shown a large increase in conductance, in some cases a doubling of the conductance of the sample. The precise nature of the effect is difficult to establish, but it is consistent with a model for the conduction mechanism in which junctions between crystallites in the sample control the overall conductivity.

3.2.10 Thin Film Transistor

Once all 2 probe electrical measurements had been recorded, the VO_2-DNA nanowires were incorporated into a thin film transitor as described in section 2.4.2. The same Agilent Technologies B1500A Semiconductor Device Analyzer was used for the 3 probe measurements in which the voltage was maintained at 0.1 V across the source and drain whilst the gate voltage was varied. By varying the gate voltage of a FET device an electric field is created perpendicular to the channel region which might cause a depletion or accumulation of charge carriers within the VO_2-DNA. This would be observed as a change in the current flowing between source and drain.

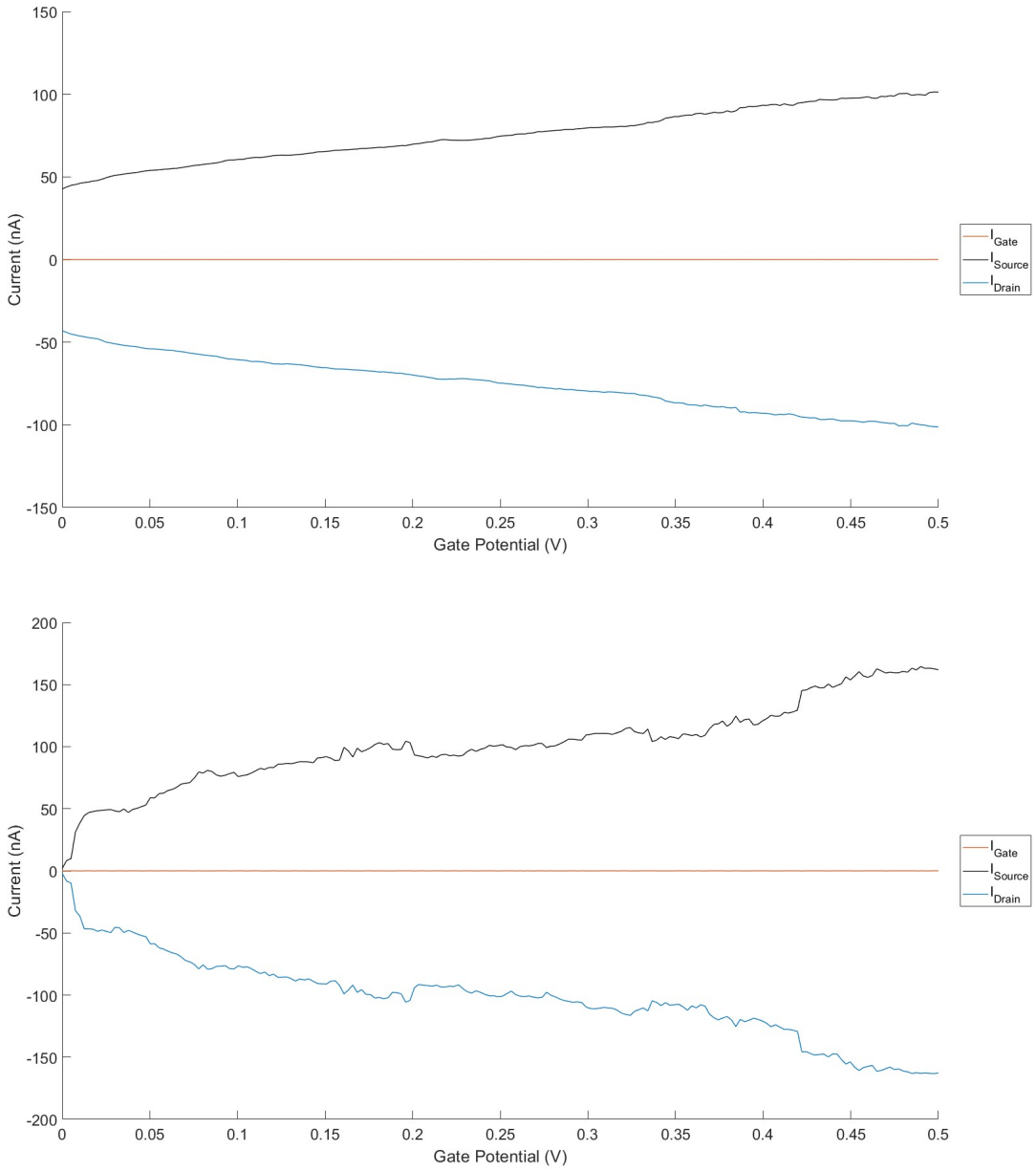

Figure 3.23: Drain current plotted against gate potential curve for a VO_2-DNA-FET.

Figure 3.23 show results from measuring two devices. As can be seen, there is a small source current increases as the potential on the gate increases due to a channel being formed within the bulk VO_2-DNA nanowire material in which electrons can hop with less resistance. At the same time the drain current mirrors the source current. This paired with the lack of current flowing from the gate to the source shows that there is no electron leakage through the insulating layer between the source / drain and gate, therefore the increase in current is solely due to the increase in gate voltage. This result shows the first

time a transistor like device has been prepared using vanadium oxide nanowires grown by a templating reaction.

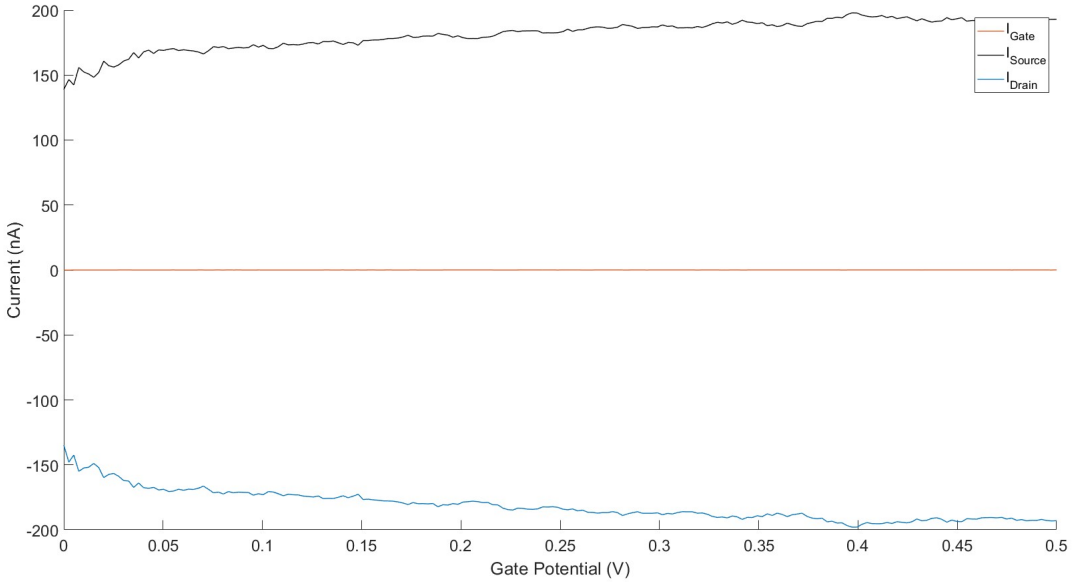

Figure 3.24: Drain current plotted against gate potential curve for a VO_2-DNA-FET.

Another device measured is shown in figure 3.24 however an even smaller rise is shown which can be explained by VO_2-DNA not behaving as a classic semiconductor. It would be expected that there would be a larger and more sudden increase in source-drain current however in VO_2-DNA, the current is only around 2x larger. This could be due to the hopping mechanism described above not being as strongly influenced by a gate voltage compared to a classical semiconductor. The VO_2-DNA network has a more complex morphology than a doped crystalline silicon wafer, making it more difficult to drive charge carriers into the channel when the gate voltage is applied.

Figure 3.25 shows the current running through the drain against the drain potential whilst the gate voltage is held at 2 V. This shows a threshold voltage of around 1.2 V which shows the apparent minimum gate to source voltage that is required to create a conductive path between the source and drain.

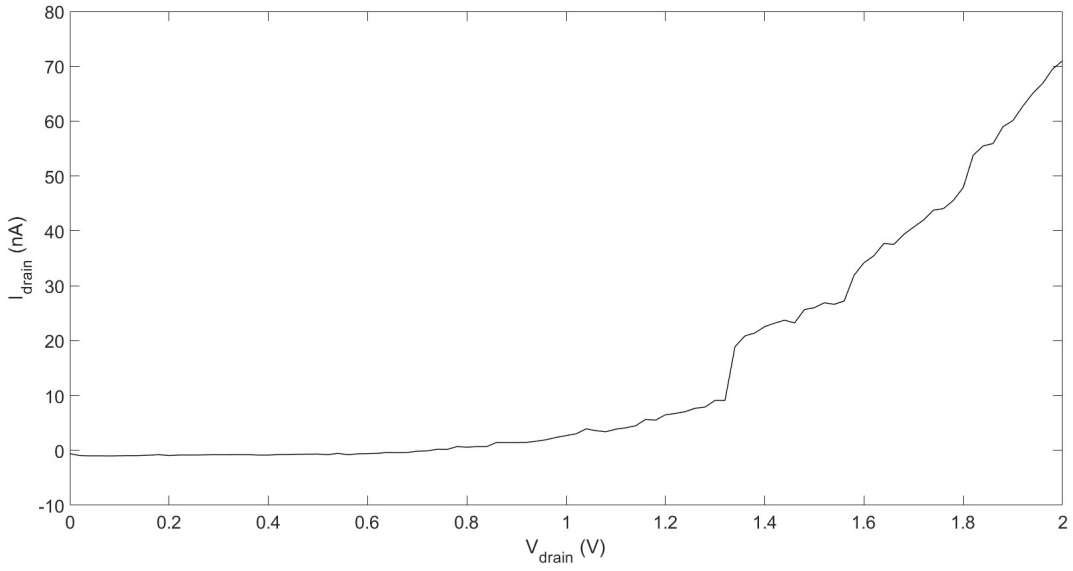

Figure 3.25: Drain current plotted against drain voltage for a VO_2-DNA-FET.

It has to be noted that the above results are from the 2 best devices found and overall there were 4 more which showed similar properties as figure 3.24. Due to the delicate nature of the devices, the yield of working TFTs from a single processed chip was around 3 %. The process involved with testing devices was to first run an IV to check for strong enough current levels. This is the stage the vast majority of devices failed at possibly due to the small amount of material present between the source and drain as well as the low contact surface area. Devices were also very delicate with regards to current levels; 0.01 V was chosen as the potential for the source / drain as it was less likely to cause damage to the devices. The final main failure was pinhole leaks through the insulating layer causing current to travel from the gate to the source and drain as shown below in figure 3.26 Overall the TFTs produced were repeatable however care was needed during processing and testing. Future work should include further optimisation on device design such as maximising the surface area the material has to contact the source and drain.

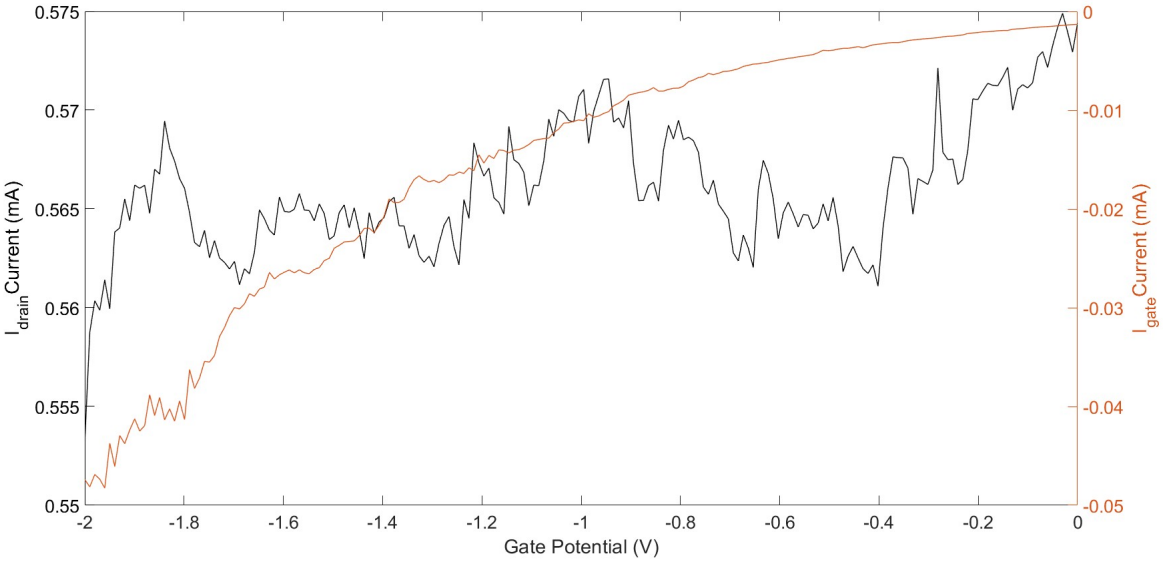

Figure 3.26: Drain current plotted against drain voltage for a failed VO_2-DNA-FET.

This section shows evidence of transistor like behaviour by a DNA-templated material for the first time. As the gate voltage increases, there is also an increase in the source-drain current when set at a constant voltage.

3.3 Conclusion

This chapter outlines the first time that DNA has been used as a template to grow conducting VO_2 nanowires. UV-Vis and FTIR have been used to show both the presence of DNA within the sample along with the lack of V(V) impurities arising from the starting reagents. FTIR also provides evidence of the interaction of the VO_2 with the DNA strands via the shift in the phosphorus-oxygen stretching modes. XPS studies confirm the presence of V(IV) and provided evidence that an interaction was taking place between the vanadium and DNA due to the differing binding energies shown between samples with and without DNA present during preparation. Powder XRD demonstarted that the B phase of VO_2 was formed in the templating reaction on DNA. The morphology of the VO_2-DNA was investigated by AFM and structures of several micrometres in length were observed. These images showed wire-like structures with heights of 6 - 12 nm exceeding what is expected for bare DNA. In the absence of DNA these wires were not formed, instead there are small particles of material with heights between 10 - 15 nm. IV measurements showed good current

levels and mS conductances that have not been seen before in DNA templated inorganic materials. The potential and temperature dependence of the conductivity was however not typical of a metallic conductor as would be expected for VO_2 (B). The conductivity data can be rationalised by a hopping model similar to a grannular metal. A sintering effect was also observed in which the conductivity increased after heating to 100^{o}C and AFM imaging also showed large changes in morphology after heating. VO_2-DNA was incorporated into a thin film transistor and basic transistor like behaviour was found in which the source-drain current increased with an increase in the gate voltage. However, the effect was relatively small, of the order of a factor of 2. This may be due to morphology of the VO_2-DNA and the underlying metallic nature of the VO_2 (B) phase.

Bibliography

[1] V. Mounasamy, G. K. Mani and S. Madanagurusamy, *Microchimica Acta*, 2020, **187**, 253.

[2] D. Chen, J. Li and Q. Wu, *Journal of Nanoparticle Research*, 2019, **21**, 201.

[3] S. Wang, K. A. Owusu, L. Mai, Y. Ke, Y. Zhou, P. Hu, S. Magdassi and Y. Long, *Applied Energy*, 2018, **211**, 200–217.

[4] C. Zhou, D. Li, Y. Tan, Y. Ke, S. Wang, Y. Zhou, G. Liu, S. Wu, J. Peng, A. Li, S. Li, S. H. Chan, S. Magdassi and Y. Long, *Advanced Optical Materials*, 2020, **8**, 2000013.

[5] H. Ji, D. Liu, C. Zhang and H. Cheng, *Solar Energy Materials and Solar Cells*, 2018, **176**, 1–8.

[6] T. Yajima, T. Nishimura and A. Toriumi, *Nature Communications*, 2015, **6**, 10104.

[7] M. Li, S. Magdassi, Y. Gao and Y. Long, *Small*, 2017, **13**, 1701147.

[8] W. Lv, C. Yang, G. Meng, R. Zhao, A. Han, R. Wang and J. Liu, *Scientific Reports*, 2019, **9**, 10831.

[9] H. Ma, X. Zhang, R. Cui, F. Liu, M. Wang, C. Huang, J. Hou, G. Wang, Y. Wei, K. Jiang, L. Pan and K. Liu, *Nanoscale*, 2018, **10**, 11158–11164.

[10] X. Liu, Y. Jiang, D. Ba, W. Zhou, Y. Li and J. Liu, *Chemical Communications*, 2020, **56**, 70–73.

[11] L. Dong, T. Hollis, S. Fishwick, B. Connolly, N. Wright, B. Horrocks and A. Houlton, *Chemistry - A European Journal*, 2007, **13**, 822–828.

[12] I. Derkaoui, M. Khenfouch, I. Elmokri, B. Mothudi, M. Dhlamini, S. Moloi, I. Zorkani, A. Jorio and M. Maaza, *IOP Conf. Ser.: Mater. Sci. Eng.*, 2017, **186**, 012007.

[13] A. V. Tataurov, Y. You and R. Owczarzy, *Biophysical Chemistry*, 2008, **133**, 66–70.

[14] M. Sirajuddin, S. Ali and A. Badshah, *Journal of Photochemistry and Photobiology B: Biology*, 2013, **124**, 1–19.

[15] H. Miyata, K. Fujii, T. Ono, Y. Kubokawa, T. Ohno and F. Hatayama, *J. Chem. Soc., Faraday Trans. 1*, 1987, **83**, 675.

[16] H. ji, H. Cheng, C. Zhang, L. Yang and D. Ren, *RSC Adv.*, 2017, **7**, 5189–5194.

[17] W. Chen, J. Peng, L. Mai, H. Yu and Y. Qi, *Solid State Communications*, 2004, **132**, 513–516.

[18] A. Juan Marcelo, M. Tuttolomondo, S. Beatriz and A. Ben Altabef, *Journal of Raman Spectroscopy*, 2015, **46**, 369–376.

[19] Y. Han, L. Han, Y. Yao, Y. Li and X. Liu, *Anal. Methods*, 2018, **10**, 2436–2443.

[20] A. A. Ouameur and H.-A. Tajmir-Riahi, *Journal of Biological Chemistry*, 2004, **279**, 42041–42054.

[21] S. Alex and P. Dupuis, *Inorganica Chimica Acta*, 1989, **157**, 271–281.

[22] G. I. Dovbeshko, N. Y. Gridina, E. B. Kruglova and O. P. Pashchuk, *Talanta*, 2000, **53**, 233–246.

[23] K. M. Shafeeq, V. P. Athira, C. H. R. Kishor and P. M. Aneesh, *Appl. Phys. A*, 2020, **126**, 586.

[24] A. Venkatesan, N. Krishna Chandar, S. Arjunan, K. N. Marimuthu, R. Mohan Kumar and R. Jayavel, *Materials Letters*, 2013, **91**, 228–231.

[25] L. Zhang, J. Yao, Y. Guo, F. Xia, Y. Cui, B. Liu and Y. Gao, *Ceramics International*, 2018, **44**, 19301–19306.

[26] Y. Oka, T. Yao, N. Yamamoto, Y. Ueda and A. Hayashi, *Journal of Solid State Chemistry*, 1993, **105**, 271–278.

[27] S. A. Corr, M. Grossman, Y. Shi, K. R. Heier, G. D. Stucky and R. Seshadri, *J. Mater. Chem.*, 2009, **19**, 4362–4367.

[28] F. Théobald, R. Cabala and J. Bernard, *Journal of Solid State Chemistry*, 1976, **17**, 431–438.

[29] S. Pruneanu, S. A. F. Al-Said, L. Dong, T. A. Hollis, M. A. Galindo, N. G. Wright, A. Houlton and B. R. Horrocks, *Advanced Functional Materials*, 2008, **18**, 2444–2454.

[30] P. Girard, *Nanotechnology*, 2001, **12**, 485.

[31] C. Staii, A. T. Johnson and N. J. Pinto, *Nano Letters*, 2004, **4**, 859–862.

[32] Y. Zhang, N. Chen, Y. Zhou, H. Lai, P. Liu and W. Xie, *CrystEngComm*, 2022, **24**, 518–542.

Chapter 4

Preparation, Characterisation and Transistor Behaviour of Cadmium Sulphide-DNA Nanowires

4.1 Introduction

Cadmium sulphide (CdS) is a semiconducting material with a narrow band gap of around 2.4 eV which is low cost and has excellent optical and electrical properties.[1–3] CdS nanowires can be prepared through a nucleation process in which DNA acts as a template with the end result being a one-dimensional structure with a large surface area to volume ratio.[4] There are two main methods in which CdS can be grown on DNA, in solution and substrate-immobilized method.[5,6] The former methodology is used in this research in which DNA is suspended in a solvent to which the the cations are added. This method reduces the number of parasitic nanoparticles that form with the substrate-immobilized method.[7] Structures and semiconducting devices have been prepared using thin films such as a thin film transistor created by Mereu, however this has not yet been achieved with CdS nanowires.[8]

The aim of this chapter is to first fully chemically and electronically characterise CdS-DNA nanowires prepared through a precipitation reaction which proceeds via nucleation and growth. This characterisation includes UV-Visible spectroscopy, atomic force microscopy and IV measurements. From there the CdS-DNA nanowires are to be incorporated into a thin film transistor.

4.2 Results and Discussion

4.2.1 Preparation of DNA-Templated Cadmium Sulphide Nanowires

To prepare the cadmium sulphide (CdS) nanowires the same method was followed as found in the paper by Dong.[4] A two stage reaction was used in which $Cd(NO_3)_2$ (100 μL 0.2 mM) was added dropwise to a stirring solution of λ-DNA (100 μL, 500 $\mathrm{ng\,mL^{-1}}$) followed by Na_2S (100 μL 0.2 mM) also being added drop-wise. The suspension was left for 24 hours at 4 $^{\circ}$C. After this incubation $Cd(NO_3)_2$ (10 μL 20 mM) was added drop-wise to the stirring solution. Finally Na_2S (10 μL 20 mM) was added drop-wise and left at 4 $^{\circ}$C for 24 before it was ready to be used.

4.2.2 UV-Visible Absorbance Spectroscopy

To characterise the optical properties of the CdS-DNA solution UV-Visible Spectroscopy was used and figure 4.1 shows the characteristic spectrum of CdS.[9,10] UV-Vis samples were measured between 240 - 800 nm using a Thermo Scientific NanoDrop One MicroVolume spectrometer at room temperature. Due to the smaller volume of sample produced, the nanodrop functionality was used for measurements. After recording a background using the respective solvents stated in section 2.2.2, 2 μL of sample was used in order to obtain a spectra. The large peak at 260 nm is assigned to the DNA present within the sample which is explained in 3.2.2.[11]

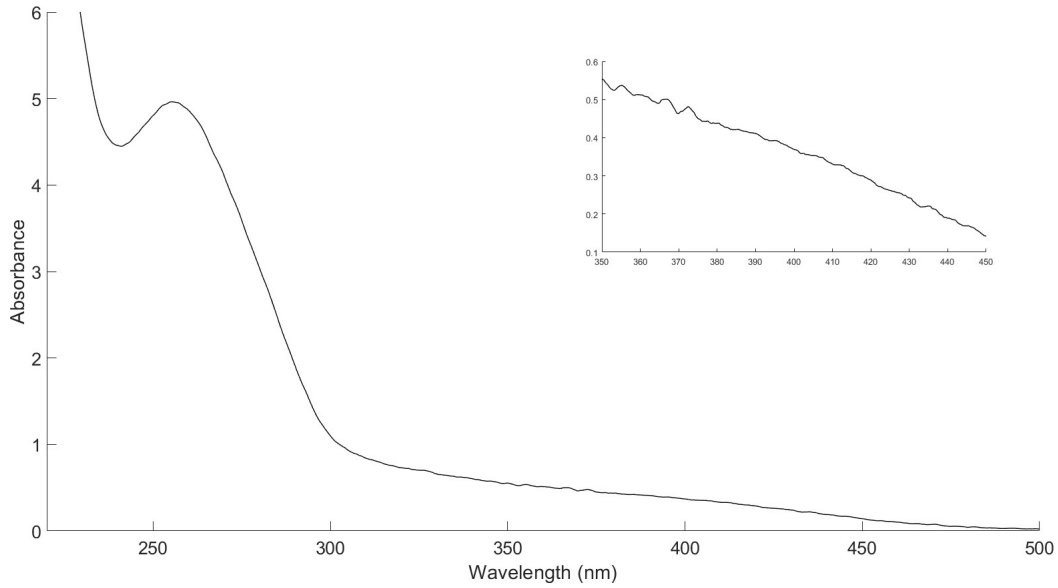

Figure 4.1: UV-Vis spectra of CdS-DNA. Inset shows shows small shoulder peak at around 440 nm.

The inset in figure 4.1 shows a shoulder that can be associated with the CdS present within the sample. The broad peak at 440 - 480 nm shows a blue shift in comparison to the expected 515 nm for bulk CdS and also matches the spectra produced in reference.[10 12] The shoulder peak can be attributed to the CdS exciton and is size sensitive due to the quantum confinement when the crystallite radius approaches the Bohr radius of the exciton at around 5 nm.

4.2.3 Atomic Force Microscopy

The structure of the CdS-DNA was then investigated using tapping mode AFM prepared as described in section 2.3.3. The sample was first diluted by a factor of 10^4 and drop-cast onto a mica substrate which had freshly cleaved to provide a clean surface. The sample was then left in a laminar flow hood to dry. As stated earlier, images of bare DNA show long wire like structures with heights around 1 - 2 nm. DNA was shown to have a radius of 2 nm by Franklin's XRD image in 1953 however in AFM it is often seen to be less than this.[13] This is due to the interaction between the tip and the sample in which DNA can be compressed by the tip.[14] Figure 4.2 shows an example image of the CdS-DNA material on the left and the corresponding height graphs on the right.

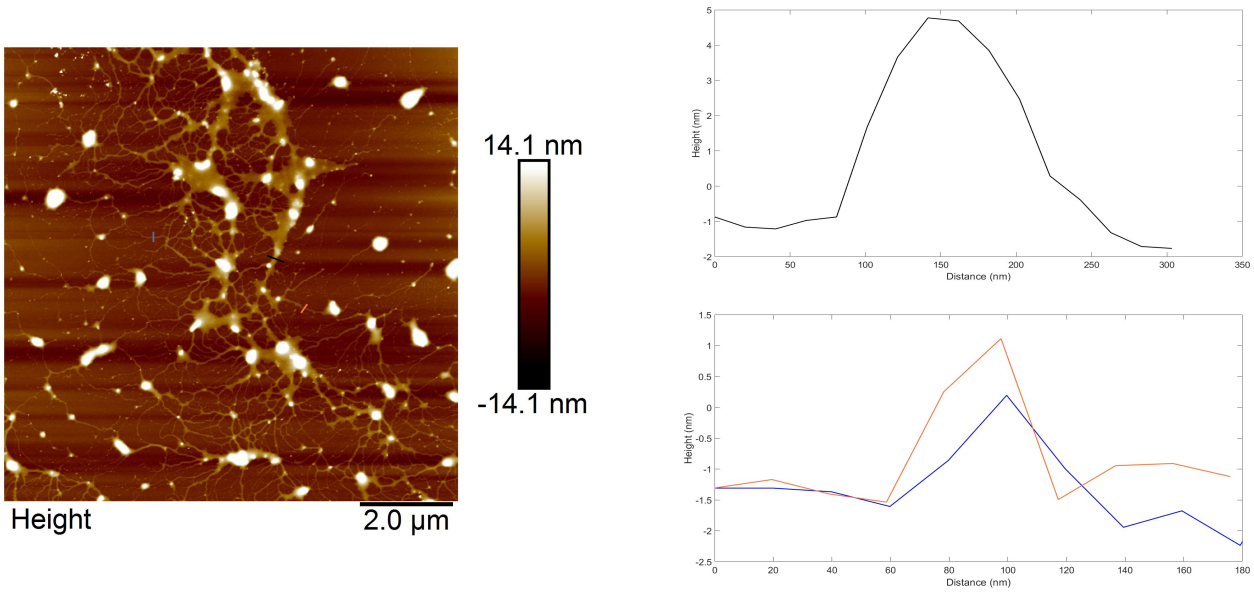

Figure 4.2: AFM image (left) showing CdS-DNA nanowires with the corresponding height graphs (right). The coloured lines on the AFM image correspond to the same colour on the height graphs. The above height graph shows the height of a templated section where as the bottom height graph shows bare DNA.

A large network of structures in which there some are wire like structures of varying heights along with large particles. The black line in figure 4.2 correlates to the maximum height diagram in which one of the thicker structures is approximately around 5 nm high where as the orange and blue lines indicate thinner structures of around 1 nm. The difference in height suggests that the thinner structures are bare DNA, which shows heights of less than 2 nm in AFM images, and CdS coated DNA which would appear thicker, in this case 5 nm. There are also large particles present within the AFM image which are tentatively assigned as CdS crystals which have not nucleated on a DNA strand. CdS prepared in the absence of DNA forms a powder without the extended network that is seen in figure 4.2. Past studies have shown single wire structures of CdS-DNA and not a larger entangled network as seen in figure 4.2 however in these studies the height of the wires measured are similar to those measured in this work.[4,10,15] CdS prepared in the absence of DNA forms a powder with no extended network.

4.2.4 IV Characterisation

Samples were prepared for electrical characterisation as detailed in section 2.4.1 and were analysed using an Agilent Technologies B1500A Semiconductor Device Analyzer. 10 μL of the CdS-DNA solution was drop cast onto a clean interdigitated electrode and allowed to dry in a laminar flow hood. The CdS-DNA nanowires showed a conductance at zero bias in the low nS with the example in figure 4.3 recording 1.82 nS. The measured IV currents are similar to those in past work completed by Nurdillayeva.[4,10,16]

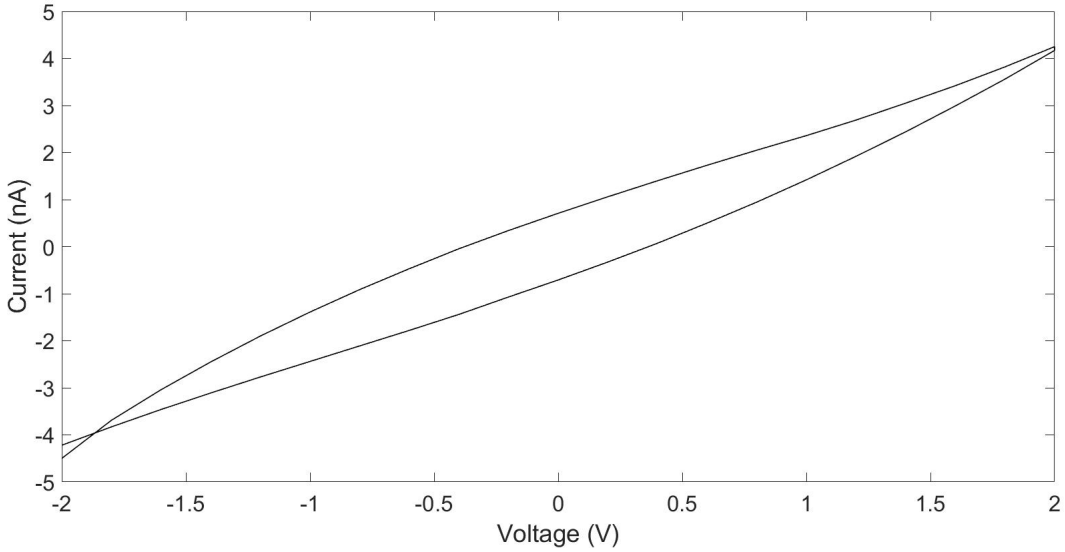

Figure 4.3: IV curve of CdS-DNA at 20 $^{\circ}\mathrm{C}$.

Current - voltage curves were then measured over a temperature range of 20 - 100 $^{\circ}\mathrm{C}$ at 10 $^{\circ}\mathrm{C}$ increments with samples allowed to equilibrate for 20 minutes at each temperature.

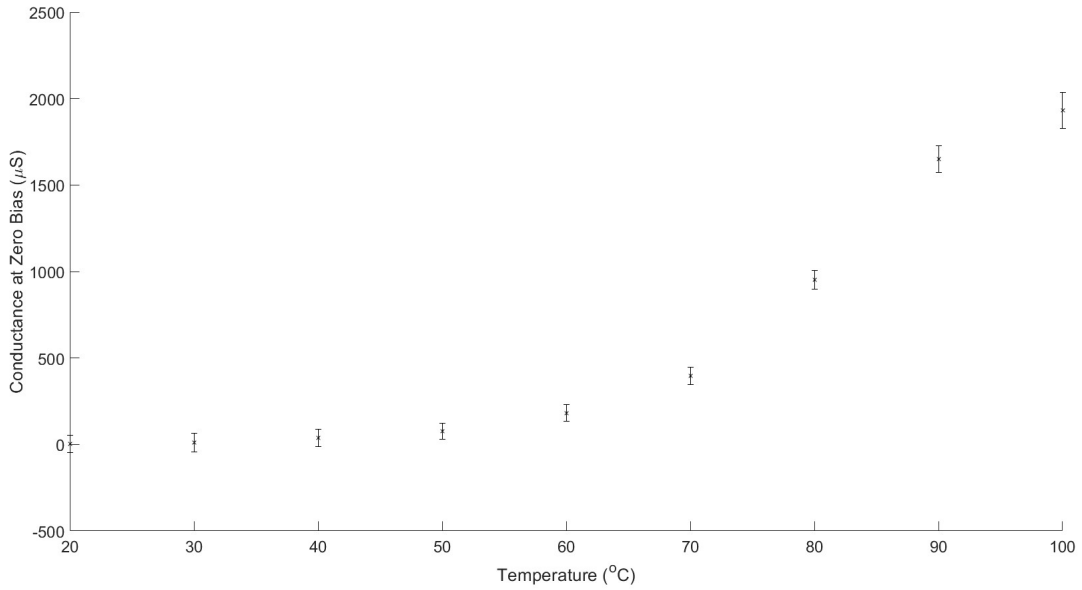

Figure 4.4: Temperature dependent conductance at zero bias of CdS-DNA over a range of 20 - 100 °C.

Figure 4.4 shows the conductance at zero bias for CdS-DNA nanowires with error bars showing the standard deviation for 3 devices. A low number of devices were analysed using this method due to the temperature dependence of CdS-DNA being well characterised within the research group. It shows a steep increase in conductance as the temperature increases temperature increases. As discussed in section 1.7.1 this is typical of a semiconducting material in which the conductance-temperature relation is dominated by the number of carriers which are thermally excited from the valence band to the conduction band as seen in figure 4.5. However, other conduction mechanisms may also produce a rise in conductivity with temperature.

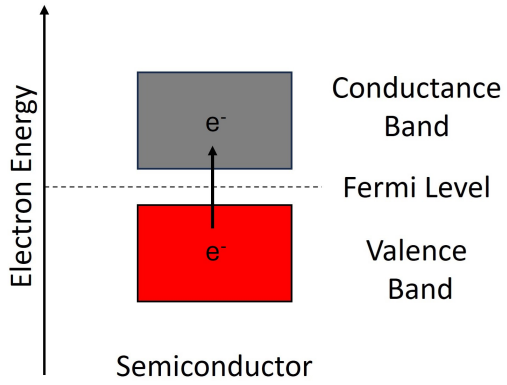

Figure 4.5: A diagram showing the different band gaps between a metal, semiconductor and insulator. Metals have an overlap between the conductance band and valence band, semiconductors have a small gap and insulators a large gap. The more electrons present within the conductance band, the more current can flow.

At higher temperatures it was noticed that the shape of the IV curve changed and the hysteresis (a difference in current between the forward and backward scans) increased compared to lower temperatures. Current peaks were also observed at around 0.5 V as shown in figure 4.6.

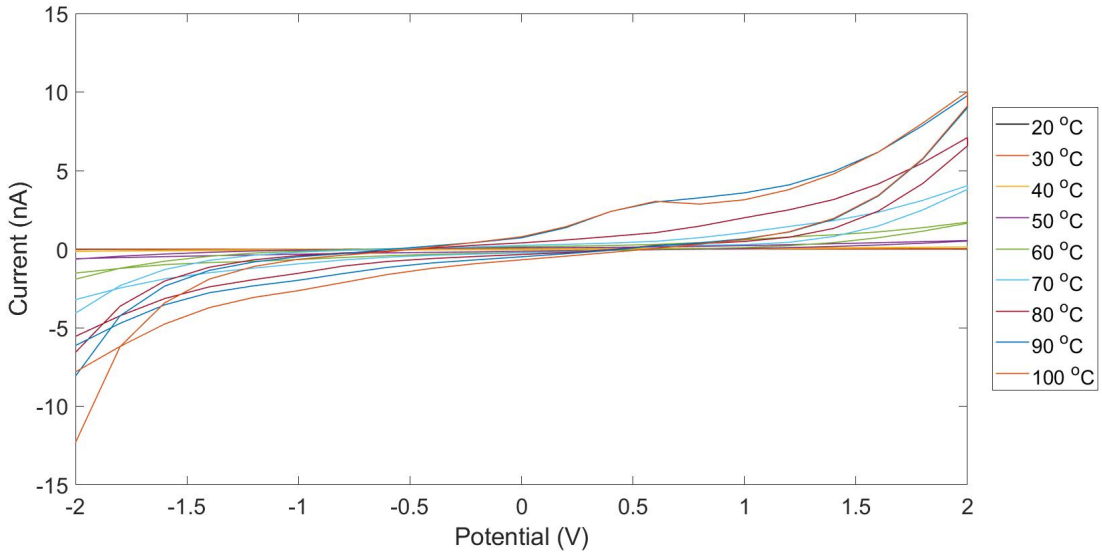

Figure 4.6: Temperature dependent IV curves of CdS-DNA over a range of 20 - 100 °C.

This change in shape is not expected for a semiconductor and is more characteristic of a electrochemical redox cell.[17] The hysteresis and peaks can be rationalised in terms of ionic currents caused by Na^+ ions which were present both within the DNA buffer solution remaining on the samples after drying and in Na_2S which was used as a source of sulfide.

The mass of an Na^+ ion is about 4 x 10^4 times greater than an electron and its mobility is expected to be much lower. When a potential is applied across the CdS-DNA device, the electrons will respond more rapidly to the field and produce a current.[18] However, the Na^+ ions will eventually migrate in the direction of the field and thereby change the potential distribution across the sample. Na^+ are relatively inert (not easily oxidised or reduced) and therefore are not likely to be discharged at the electrodes, instead they would be expected to form a space-charge layer at the negative electrode. This situation is analogous to an electrochemical cell in which the ions of the background electrolyte form electrochemical double layers (space-charge layers) and screen the charge on the electrodes. The current is then determined by the rate of charge injection at each electrode/solution interface. In the present case, it is suggested that residual Na^+ and counter-anions from the preparation are present in sufficient amounts for the device to behave as an electrochemical cell.[10]

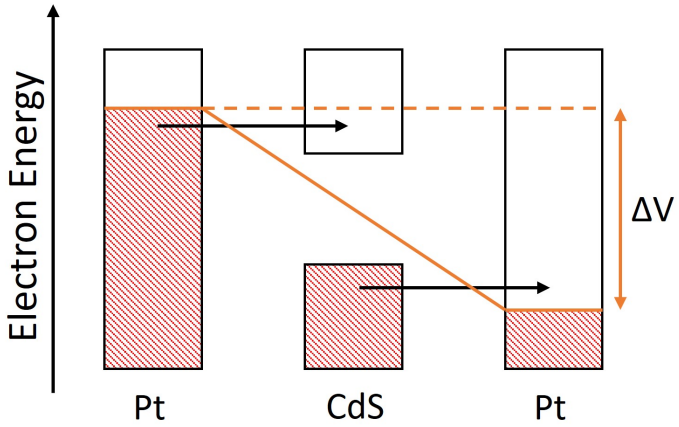

Figure 4.7: A diagram showing the shift in Fermi energy levels between the first and second platinum electrode/CdS interfaces.

he non-linear shape of the IV cure can also be explained in terms of charge injection at the two electrodes. The effect of the applied potential is to shift the Fermi level of the platinum electrodes with respect to the energy bands of the CdS. At negative potentials the energy levels of all electrons in the conduction band of the platinum are elevated and the Fermi level rises. When this approaches the conduction band edge, more electrons have sufficient energy to move to the conduction band of the CdS. Conversely, a sufficiently high positive potential can lower the Fermi energy of the electrode below the valence band edge and facilitate injection of holes into the CdS. This concept is show in figure 4.7. In

general, such a mechanism predicts that the IV curve would show little current within a range where the Fermi levels of the two electrodes lie within the bandgap, i.e., a potential window $V \simeq E_g$. Although this is roughly in agreement with the form of the IV curves in figure 4.3, the potentials at which there is an onset of current are not sharply defined and this is not definitive evidence of the mechanism.

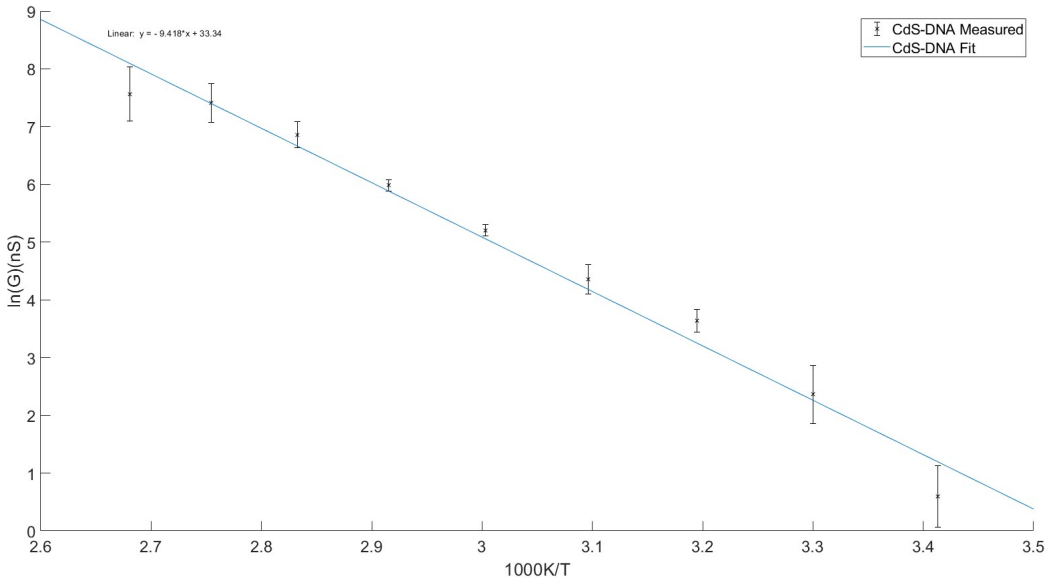

Figure 4.8: Arrhenius plot of CdS-DNA (black) with a linear fit (blue).

To further explore the nature of the conduction mechanism, the conductance-temperature data was plotted in the form lnG against $1/T$ in figure 4.8. The activation energy derived from this plot was 0.81 eV. If the origin of this value were simple thermal excitation of charge carrier across the band gap, then the activation energy would have been about half the gap, which for bulk CdS is $2.4/2 = 1.2$ eV.[12] There is no simple expectation for the value of the activation energy if the charge-injection at the electrodes (or hopping) were rate-limiting, except that it will be less than that required to promote electrons entirely across the band gap. The temperature-dependence of the IV data is at least consistent with an interpretation in terms of rate-limiting charge injection at the contacts.

4.2.5 Impedance

One method which can provide information on the rate of charge transfer across the interfaces at the contacts is impedance spectroscopy. A brief discussion of the method is

given and then it is applied to the case of the CdS-DNA devices.

Impedance is described as the opposition to current flowing around a circuit when alternating current is used and can be used to find both the contact and bulk resistance of a sample. The basic concept is that the alternating current and voltage will have a linear relation as long as the amplitude is in some sense small. For the potential-dependent conductances discussed section 1.7.1, the appropriate criterion is $eV < k_BT \simeq 25$ meV such that the exponential terms can be linearised. Impedance is given the symbol Z, is measured in Ω and includes effect of both resistances (R) and reactances (X) arising from capacitors or inductances in the system. Impedance can be written as a complex number with real and imaginary parts as shown in equation 4.1.

$$Z = R + iX \tag{4.1}$$

In equation 4.1 i denotes $\sqrt{-1}$ and not current. The capacitive reactance is $-1/\omega C$ where $\omega = 2\pi f$ is the angular frequency of the ac signal. Importantly, the impedance of a combination of any circuit elements can be obtained using the well-known rules for series and parallel combinations in the same way as for simple resistors - impedances in series are added and impedances in parallel are added in reciprocal. For example, a series combination of a resistor and a capacitor has impedance $Z = R - \frac{i}{\omega C}$.

In impedance spectroscopy, the frequency of the ac signal applied to the two-terminal device is varied and the plot of impedance against frequency is referred to as the impedance spectrum. This may take the form of a set of points in the complex plane, labelled by the associated frequencies; this is usually called a Nyquist plot.

CdS-DNA devices were prepared as discussed in section 2.4.1 however two copper wires were soldered onto the contact points. Impedance was then measured on a PalmSens 3 instrument in a nitrogen atmosphere with no light present in order to remove any variation in impedance that could be caused by water in the air or photocurrents. The samples was measured at 0.1 V between 10000 - 1 Hz and a Nyquist plot was produced as shown in figure 4.9.

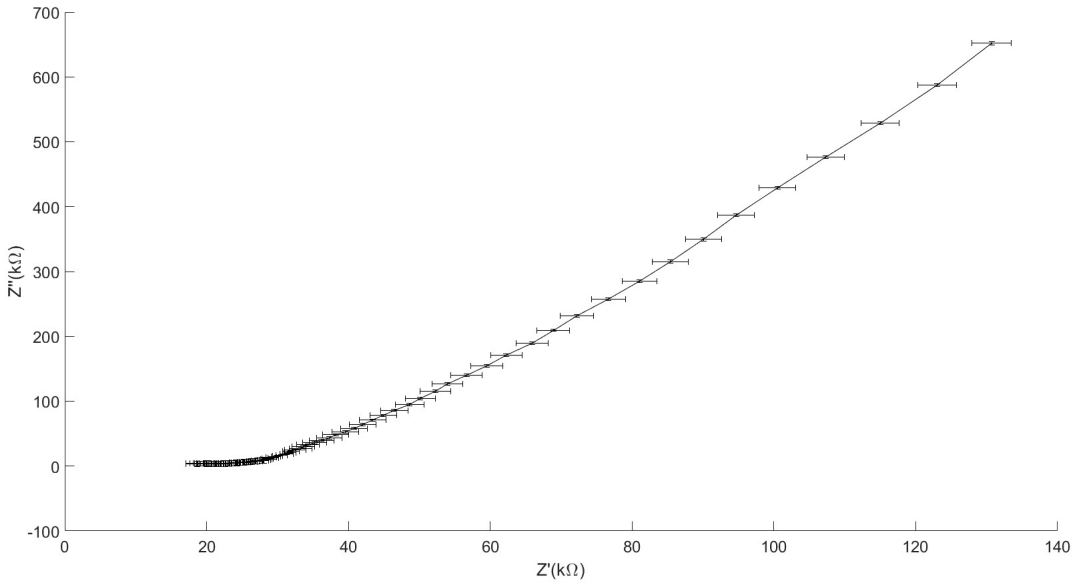

Figure 4.9: The impedance spectrum recorded for CdS-DNA. The samples were measured between 10000 - 1 Hz at 0.1 V.

In order to conveniently analyse the impedance spectra of the CdS-DNA devices an equivalent circuit that represents the physical situation was devised as shown in figure 4.10. In this circuit, R_c represents the contact resistance at the Pt/CdS-DNA interface and is determined by the ease of charge injection into the CdS. R_b represents the bulk resistance of the CdS-DNA nanowires, which may occur via band-like or hopping mechanisms. C is the inter-facial capacitance at the Pt/CdS-DNA contacts which would depend, for example, on the screening of charge on the Pt electrodes by ions present in the CdS-DNA sample.

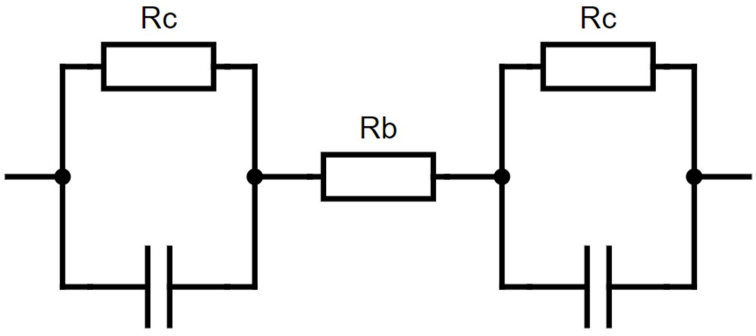

Figure 4.10: The equivalent circuit of the Pt/CdS-DNA/Pt electrode showing a parallel combination of contact resistors (Rc) and capacitors with the bulk CdS-DNA resistance being in series.

The full expression for the impedance of the equivalent circuit is given by equation 4.2.

$$Z = 2R_c \frac{1 - i\omega C R_c}{1 + \omega^2 C^2 R_c^2} + R_b \tag{4.2}$$

Equation 4.1 defines a semi-circle in the Nyquist plot. At high frequencies, Z reduces to R_b because the impedance of the capacitances at the Pt/CdS-DNA interfaces is negligible. In this limit no charge is injected at the contacts, but instead the variation of the applied potential causes charging/discharging of the double layers (space charge regions) at the Pt/CdS-DNA interfaces. At intermediate frequencies the impedance spectrum has the form of a semicircle in the upper half of the complex plane with a maximum at $\omega R_c C = 1$. At low frequencies, the impedance returns to the real axis at a value of $2R_c + R_b$ where the factor of 2 comes from assuming that the two electrodes are identical. In this limit, the interfacial capacitances have a large impedance and the current pathway corresponds to charge injection at either interface.

Figure 4.9 shows typical impedance data for the Pt/CdS-DNA devices. This is assigned to the high-frequency limit because the imaginary part of the impedance is still increasing strongly at the lowest frequencies investigated. Interestingly, the estimate we obtain for the bulk resistance of the CdS-DNA under this assumption is about 0.03 $\mathrm{M}\Omega$, much smaller than observed in the IV characteristic. The natural interpretation of the data is that the measured IV curves are dominated by contact resistance effects and substantial dc currents only flow at large potentials where charge injection into the conduction and valence bands is possible. In view of the low currents obtained, attempts were made to improve the device output, as described in the next sections.

4.2.6 Sintering Effects

Due to the success with sintering the VO_2-DNA nanowires it was hoped this could be repeated with the CdS-DNA nanowires. Samples were exposed to temperatures ranging from 100 - 200 $^{\circ}\mathrm{C}$ for varying times however when IV curves were recorded, large decreases in the current and conductance at zero bias were found, dropping from 14.6 nS to 0.752 nS in the typical data shown in figure 4.11.

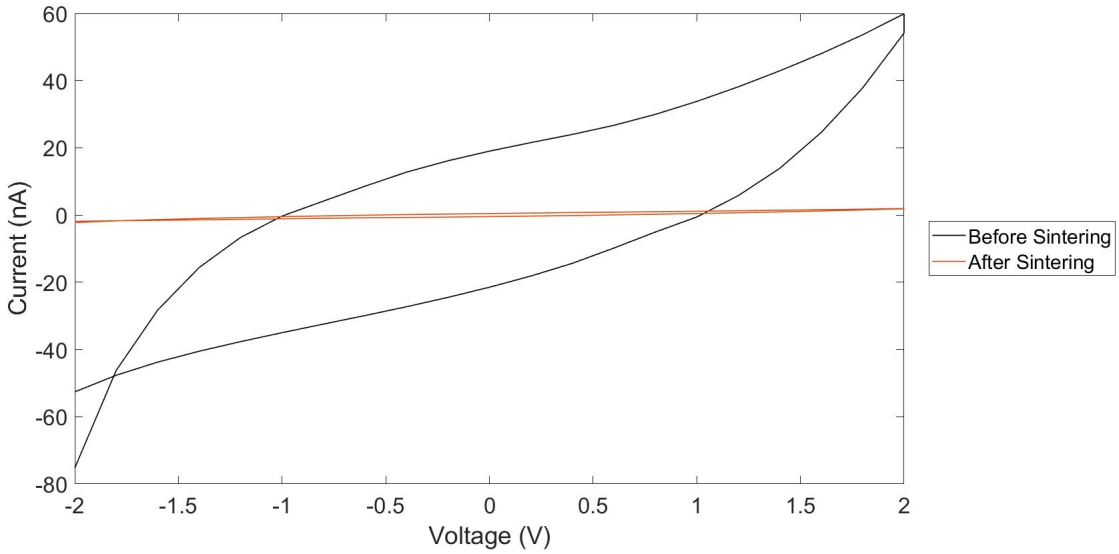

Figure 4.11: IV curves of CdS-DNA before attempted sintering (black) and after being heated for 2 hours at 150 °C (orange).

This was an unexpected result. There are three main theories as to why this decrease occurred. The first is that the sample still had small amounts of residual solvent trapped in the film after drying the solution onto the electrode and during the higher temperatures this solvent evaporated and lifted the nanowires from the surface and contact points. The second possibility involves the denaturing of bare DNA which is when the double helix of DNA separates into single strands The denaturing point of DNA is 76.2 °C according to Wallace et al meaning any areas of the nanowires that had poor templating during preparation would have denatured during the increased temperatures.[19,20] Due to the denaturing, it may be possible that the wires are split therefore large gaps in the conductive material between contact points so the charge transport would be less efficient. Finally, there is the possibility that heat-treatment will cause aggregation of the CdS into larger particles leaving long lengths of bare DNA. An AFM investigation suggests this is indeed what happened. Figure 4.13 shows an image of a sample after heating for 2 hours at 150 °C.

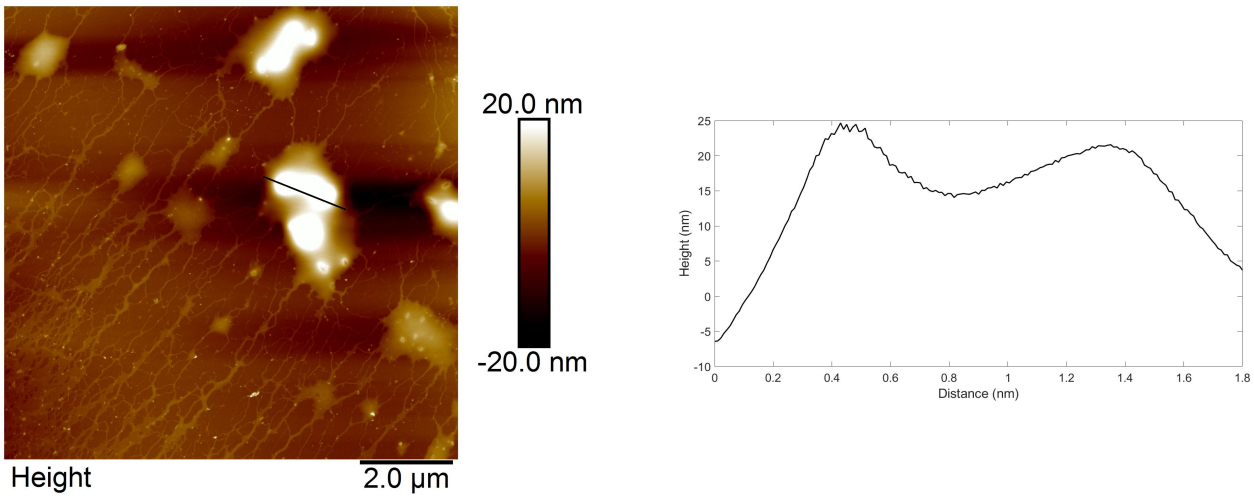

Figure 4.12: AFM images of CdS-DNA before attempted sintering and the corresponding height chart. The black line on the image indicates the area in which the heights were recorded.

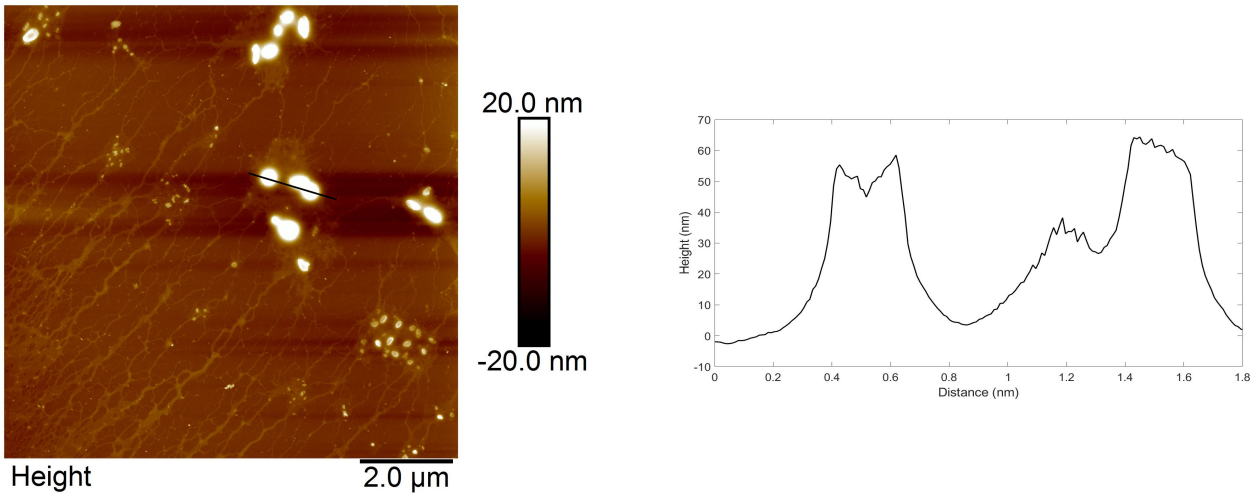

Figure 4.13: AFM images of CdS-DNA after being heated for 2 hours at 150 °C.The black line on the image indicates the area in which the heights were recorded.

A comparison of the image found after sintering (figure 4.13) with the previous image of CdS-DNA samples, figure 4.2, shows an absence of the thicker strands previously assigned to CdS-coated DNA molecules. Instead, after sintering, the image shows a few large particles and many thin strands, which are likely to be bare DNA molecules. Due to the

insulating behaviour of bare DNA and large gaps between the remaining CdS particles, a strong decrease in conductivity is the expected result.[23]

By collecting AFM images from the same area before and after heating, it has been possible to determine that the conductivity of CdS-DNA decreases due to the the CdS reverting to a pre-nucleation state, meaning there are bare patches of DNA which act as an insulator.

4.2.7 Angled Drying

Another attempt to improve the conductivity was made by trying to increase the alignment of the long DNA molecules. A common technique used with DNA is 'molecular combing' in which DNA is stretched to form an array of uniformly aligned DNA strands through a combination of liquid flow and surface adhesion forces.[24,25] To do this, a droplet of DNA solution is deposited on a substrate with a partially hydrophobic surface to which one end of the molecule binds. The liquid surface is then pulled back and the surface forces stretch the DNA leaving it aligned on the surface in the direction of the fluid flow.[26] The process is driven by hydrophobic and electrostatic forces.[27] It was hypothesized that a similar outcome could be achieved by drying the samples under a gentle flow of nitrogen with the substrates on a slope. In this arrangement, the droplets of CdS-DNA solution would move down the slope leaving the CdS-DNA molecules aligned in the direction of travel.

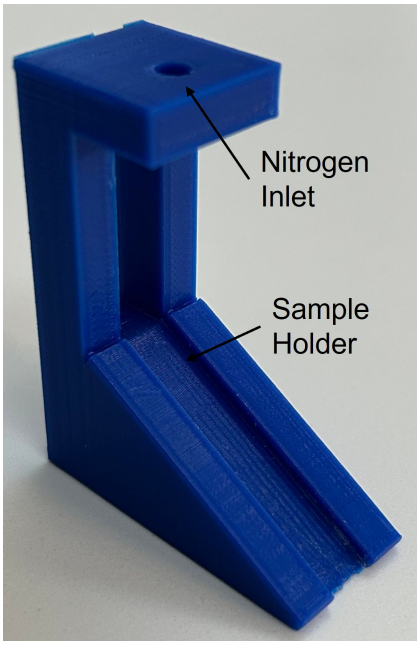

Figure 4.14: The 3D printed device which was used to hold samples at a 45 ° angle. The hole at the top allowed for a nitrogen tube to be inserted and a light flow of nitrogen blow over the sample.

To achieve this the device as pictured in figure 4.14 was 3D printed in which samples could be held consistently at a 60 ° angle whilst a small hole in the top allows for a nitrogen pipe to be inserted. The CdS-DNA solution was applied as mentioned in 2.4.1 but then left for 12 hours under a gentle flow of nitrogen. This was first attempted on a silicon substrate so that AFM images could be recorded which are found below. These images show a set of nanowires with a consistent directionality to them showing that the preliminary testing was a success and the orientation of the nanowires could be controlled to some extent.

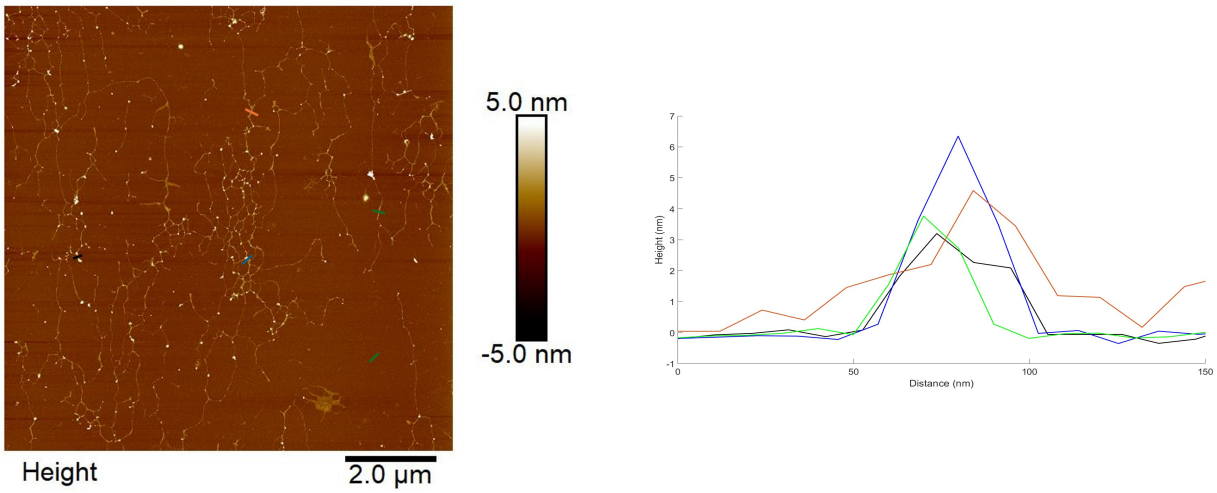

Figure 4.15: An AFM image showing examples of CdS-DNA nanowires which had been dried at a 45° using the device mentioned above and the accompanying height graph. The coloured lines on the AFM image correspond to the same colour on the height graphs. Wires are moving in a general north - south direction.

After the positive AFM images the same method was utilised for the interdigitated electrodes used for IV measurements in which the nanowires would be running perpendicular to the contact points. Figure 4.16 shows the conductance at zero bias for 6 different samples which were prepared by either vacuum drying or the angled method as mentioned above. In all 6 samples the conductance has been increased when the solution was dried at an angle and this can be attributed to a more efficient connection between the electrodes by the aligned CdS-DNA structures. The length of the longest nanowires (16 μm) is larger than the gap between electrodes (10 μm gaps), therefore single CdS-DNA molecules are able to bridge between adjacent contact points if suitably aligned. With a single wire spanning the length of the electrode gap it means electrons can travel between the contact points with a greater efficiency. When no alignment process has taken place the nanowires on the IDE will be randomly scattered and overlapping meaning a less efficient route for the electrons to travel between the two contact points. It is also likely that randomly deposited nanowires will lead to current pathways where the charge carriers must cross multiple gaps between CdS-DNA molecules.[10,28]

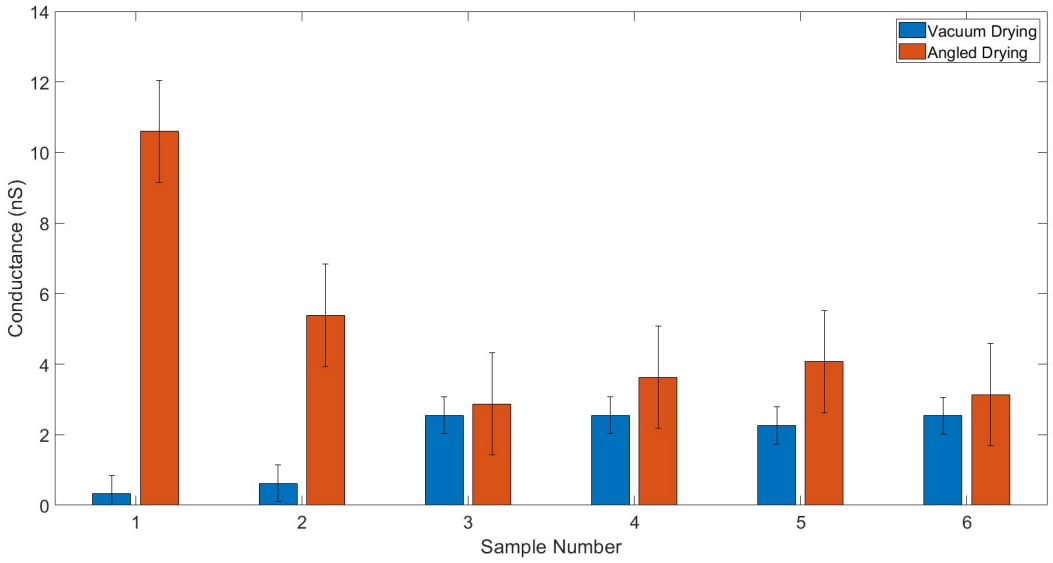

Figure 4.16: A comparison between the conductance at zero bias between normal vacuum drying of samples (blue) vs drying the samples at an angle using the above device (orange). A t test was performed in which the P value equalled 0.0319 and by conventional criteria this is considered to be statistically significant.

To further investigate how the alignment affected the current, the hydrophobicity of the IDE surface was altered with the use of trimethylchlorosilane (TMS). Glass is generally hydrophilic by nature however when exposed to SiR_3X where R is an organic chain and X is a halogen, an organic monolayer forms anchored by Si-O bonds and bearing hydrophobic chains, R.[29,30] In order to vary the surface hydrophobicity the surfaces were exposed to TMS vapour for different times and the water contact angle recorded before the CdS-DNA solutions were deposited as mentioned above and IV measurements were recorded. The hydrophobic layer reduces the adhesion of DNA molecules to the substrate and affects the molecular combing process. At high hydrophilicity, DNA molecules tend to adhere too strongly to be combed, at very high hydrophobicity DNA molecules do not adhere well at all.

The main correlation between the samples recorded was the fact that a contact angle where $\theta = 60°$ seemed to show the highest conductances as seen in figure 4.17. This can be attributed to both the way the droplet forms on the surface of the IDE and how it is affected when exposed to the nitrogen flow. The nanowires adhere very strongly at a highly hydrophilic surface and the combing process fails because the fluid flow is insufficient to affect their alignment. When the surface is too hydrophobic, the nanowires do not anchor

at all and are transported by the flow rather than aligned. A contact angle where $\theta = 60°$ appeared to be a 'Goldilocks' hydrophobicity at which the nanowires attach sufficiently well to become aligned by the flow as the droplet descends the slope. In this case the CdS-DNA is spread over an increased area and has a better chance to provide a good connection between contact points.

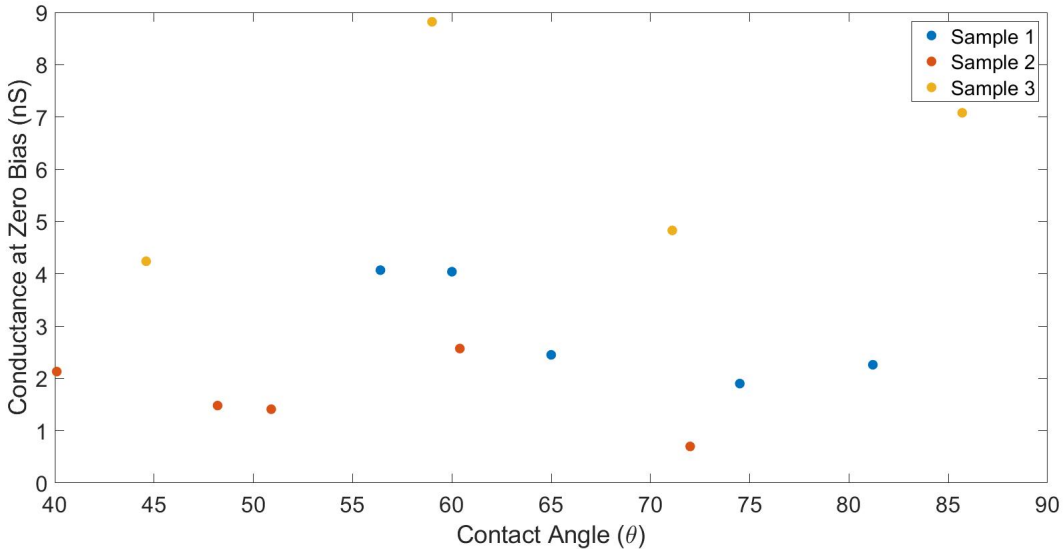

Figure 4.17: The conductance at zero bias of three samples when the contact angle of the electrode was altered using TMS.

This section shows a method for aligning wire like structures on a silicon substrate by holding the substrate at a 60 ° angle with a gentle flow of nitrogen blowing the dropcast sample down the substrate. The alignment caused a large increase in measured conductivity from samples owing to the more efficient charge transport between two contacts. It was found that altering the hydrophobicity of the substrate had an effect on the conductivity with a contact angle of 60 θ showing the best results.

4.2.8 Thin Film Transistor

Once all 2 probe electrical measurements had been recorded, the CdS-DNA nanowires were incorporated into a thin film transistor as described in section 2.4.2. The same Agilent Technologies B1500A Semiconductor Device Analyzer was used for the 3 probe measurements in which the voltage was maintained at 0.1 V across the source and drain whilst the gate voltage was varied. Due to the lower conductance of CdS-DNA the FET devices

were not successful, not enough current was able to pass between the source and drain to get a trustworthy result. This was due to two reason with the first being that the current levels between the source and drain were of the order of pA or even fA. It should be noted that although nA level currents were observed when running a simple two probe IV curve on the platinum interdigitated electrodes, this is due to the high area of contact between the sample and electrodes compared to the transistor device. In the future it may be that the transistor can be redesigned to have a higher contact area. The second reason was that the gate to source current was of a similar magnitude to the source to drain current. Figure 4.18 shows an example of one such device prepared using CdS-DNA. This is a serious flaw in the device because it demonstrates that the gate contact is not really achieving the desired function. More highly conductive CdS-DNA samples are required and better insulation methods for the gate are needed.

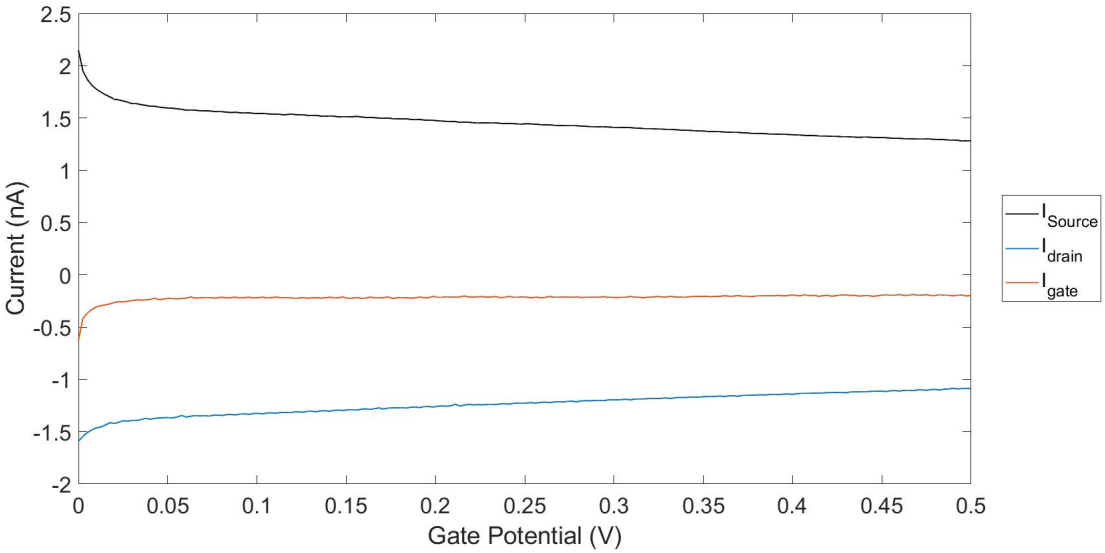

Figure 4.18: Drain current plotted against gate potential curve for a CdS-DNA-FET.

4.3 Conclusion

This section showed the preparation and investigation into CdS nanowires formed by a templating reaction in which DNA was used as the template. DNA was confirmed to be present within the sample by UV-Vis in which a peak at 260 nm was present. This peak is a characteristic sign of DNA in UV-Vis due to the $\pi \rightarrow \pi^*$ transition of nucleobase systems of pyrimidine and purine. AFM was then used to investigate the structure of the CdS-DNA

in which it was found that large wire like structures were found with heights of around 5 nm which is larger than the expected 2 nm expected for bare DNA. This shows that the structures imaged are not bare DNA and provide evidence that the CdS is present on the DNA. The electrical properties were then explored using simple IV measurements as well as impedance. The material was found to show low levels of conductance with high values of contact resistance which were too large to be found with the impedance measurements performed. Extra studies were undertaken in which the drying methodology and sintering was explored. It was found that the optimal drying conditions for the material was at a 45 $^{\circ}$ angle under a gentle flow of nitrogen and a contact angle of 60 θ. This caused alignment across the electrodes and offered the highest conductance levels. When incorporated into a thin film transistor, no transistor like behaviour was found. This is likely due to both the high contact resistance and low conductivity of the material.

Bibliography

[1] K. K. Nanda, S. N. Sarangi, S. Mohanty and S. N. Sahu, *Thin Solid Films*, 1998, **322**, 21–27.

[2] V. N. Soloviev, A. Eichhöfer, D. Fenske and U. Banin, *Journal of the American Chemical Society*, 2000, **122**, 2673–2674.

[3] A. Kariper, E. Güneri, F. Göde, C. Gümüş and T. Özpozan, *Materials Chemistry and Physics*, 2011, **129**, 183–188.

[4] R. N. Nurdillayeva, A. B. Oshido, T. A. Bamford, O. El-Zubir, A. Houlton, J. Hedley, A. R. Pike and B. R. Horrocks, *Nanotechnology*, 2018, **29**, 135704.

[5] K. Deng and L. Li, *Advanced Materials*, 2014, **26**, 2619–2635.

[6] L. Dong, T. Hollis, B. Connolly, N. Wright, B. Horrocks and A. Houlton, *Advanced Materials*, 2007, **19**, 1748–1751.

[7] Z. Wang, J. Liu, K. Zhang, H. Cai, G. Zhang, Y. Wu, T. Kong, X. Wang, J. Chen and J. Hou, *The Journal of Physical Chemistry C*, 2009, **113**, 5428–5433.

[8] B. Mereu, G. Sarau, E. Pentia, V. Draghici, M. Lisca, T. Botila and L. Pintilie, *Materials Science and Engineering: B*, 2004, **109**, 260–263.

[9] C. V. Reddy, J. Shim and M. Cho, *Journal of Physics and Chemistry of Solids*, 2017, **103**, 209–217.

[10] R. N. Nurdillayeva, B. R. Horrocks and A. R. Pike, *Materials Today: Proceedings*, 2018, **5**, 22825–22834.

[11] I. Derkaoui, M. Khenfouch, I. Elmokri, B. Mothudi, M. Dhlamini, S. Moloi, I. Zorkani, A. Jorio and M. Maaza, *IOP Conf. Ser.: Mater. Sci. Eng.*, 2017, **186**, 012007.

[12] Z. H. Zhang, W. S. Chin and J. J. Vittal, *J. Phys. Chem. B*, 2004, **108**, 18569–18574.

[13] R. E. Franklin and R. G. Gosling, *Nature*, 1953, **171**, 740–741.

[14] A. T. Winzer, C. Kraft, S. Bhushan, V. Stepanenko and I. Tessmer, *Ultramicroscopy*, 2012, **121**, 8–15.

[15] Y. Yao, Y. Song and L. Wang, *Nanotechnology*, 2008, **19**, 405601.

[16] C. Pang, B. T. Karlinsey, M. Ward, R. G. Harrison, R. C. Davis and A. T. Woolley, *Langmuir*, 2024, **40**, 14076–14085.

[17] H. Razmi and M. Harasi, *Int. J. Electrochem. Sci.*, 2008, **3**, 82–95.

[18] P. Kohn, K. Schröter and T. Thurn-Albrecht, *Phys. Rev. Lett.*, 2007, **99**, 086104.

[19] X. Wang, H. J. Lim and A. Son, *Environ Health Toxicol*, 2014, **29**, e2014007.

[20] R. B. Wallace, J. Shaffer, R. Murphy, J. Bonner, T. Hirose and K. Itakura, *Nucleic Acids Research*, 1979, **6**, 3543–3558.

[21] Q. Zhao, Y. Liu and E. W. Abel, *Journal of Colloid and Interface Science*, 2004, **280**, 174–183.

[22] X. Yuan, J. Yang, J. He, H. H. Tan and C. Jagadish, *J. Phys. D: Appl. Phys.*, 2018, **51**, 283002.

[23] A. J. Storm, J. van Noort, S. de Vries and C. Dekker, *Applied Physics Letters*, 2001, **79**, 3881–3883.

[24] A. Kaykov, T. Taillefumier, A. Bensimon and P. Nurse, *Sci Rep*, 2016, **6**, 19636.

[25] X. Michalet, R. Ekong, F. Fougerousse, S. Rousseaux, C. Schurra, N. Hornigold, M. v. Slegtenhorst, J. Wolfe, S. Povey, J. S. Beckmann and A. Bensimon, *Science*, 1997, **277**, 1518–1523.

[26] Y. Wang, K. R. Kumar and T. Liehr, *Molecular Cytogenetics*, 2022, **15**, 50.

[27] A. Bensimon, A. Simon, A. Chiffaudel, V. Croquette, F. Heslot and D. Bensimon, *Science*, 1994, **265**, 2096–2098.

[28] A. K. Jonscher, *J. Phys. C: Solid State Phys.*, 1971, **4**, 1331.

[29] S. Brito e Abreu and W. Skinner, *Langmuir*, 2012, **28**, 7360–7367.

[30] X. Cui, B. Yan, B. Zhang and Z. Fang, *Vacuum*, 2018, **151**, 15–24.

Chapter 5

Preparation, Characterisation and Transistor Behaviour of DNA - Cadmium Sulphide - Carbon Nanotube Nanowires

5.1 Introduction

Carbon nanotubes (CNTs) have been widely studied due to the unusual electronic and mechanical properties that they possess.[1–3] CNTs come in two main forms either single walled (SWCNT) or multi-wall (MWCNT) with each having different electrical properties. SWCNTs can be both semiconducting or metallic depending on the chirality of the nanotube in which: (n,n) SWCNTs are metallic, (n,m) SWCNTs where n - m = 3j where j is a non zero integer is a tiny gap semiconductor and all other SWCNTs are large gap semiconductors.[4,5] All MWCNTs on the other hand can be classed as metallic.[6,7] The first CNT field effect transistor (CNTFET) was prepared in 1998 by Martels group in which they showed evidence that both SWCNT and MWCNTs could be used within a FET device.[8,9] CNTFETs can be fabricated using both wet and dry methods with wet methods including drop-casting, spin-coating and inkjet printing.[10–12] The main issue with these methods however is the aggregation of individual nanotubes which in turn can cause a wide variation in bundle sizes which can degrade the devices performance and reproducibility.[13] One way to help with effective dispersion of CNTs is the addition of DNA into the solution.[14–16] It is also an aim to improve the conductance of the CdS-DNA found in the previous chapter. Past work has been completed using CdS-DNA hybrids with an example being the work produced by Ali *et al* who prepared hybrids with varying percentages of DNA.[17] They found that increasing the ratio of DNA:CNT decreased two terminal IV measurements as well as changing the temperature dependence behaviour from a metallic like response to a behaviour similar to a semiconductor. The work completed by Ye *et al* forms the basis of

this chapter. Ye prepared photoresponsive devices from PbS/CdS-DNA-CNT hybrids which involved first wrapping the CNTs in DNA before using a two step process to facilitate the addition of either PbS or CdS.[17]

The aim of this chapter is to first fully chemically and electronically characterise CdS-CNT-DNA nanowires prepared through a nucleation reaction. The chemical characterisation includes Fourier transform infrared spectroscopy, atomic force microscopy and X-ray photoelectron spectroscopy. The material has then been probed for the electronic properties it shows including two terminal measurements and temperature dependence. From there the CdS-CNT-DNA nanowires are to be incorporated into a thin film transistor and tested for any transistor like behaviour.

5.2 Results and Discussion

5.2.1 Preparation of DNA-Templated Carbon Nanotube-Cadmium Sulphide Nanowires

The DNA-templated carbon nanotube-cadmium sulphide (CNT-CdS-DNA) composite was prepared using a method by Ye.[18]

0.1 mg of MWCNTs was added to 10 mL of methanol and sonicated for 3 hours at room temperature. 100 μL of λ-DNA (100 μL, 500 $\mathrm{ng\,mL^{-1}}$) was added to 500 μL of the MWCNT suspension before being sonicated for 5 min and allowed to stand overnight. To finish the composite, the same method mentioned in section 2.2.2 was used in which $Cd(NO_3)_2$ (100 μL 0.2 mM) was added drop-wise to the CNT-DNA suspension followed by Na_2S (100 μL 0.2 mM) also being added drop-wise. The suspension was left for 24 hours at 4 $^{\circ}\mathrm{C}$. After this incubation $Cd(NO_3)_2$ (10 μL 20 mM) was added drop-wise to the stirring solution. Finally Na_2S (10 μL 20 mM) was added drop-wise and left at 4 $^{\circ}\mathrm{C}$ for 24 before it was ready to be used.[19]

5.2.2 X-ray Photoelectron Spectroscopy

It is possible to analyse the chemical composition of CdS-CNT-DNA by using XPS. The main reasoning behind using XPS was to help confirm the presence of DNA within the

samples as well as gain a further insight into the chemical state of the prepared material. Samples were first dropcast onto clean silicon wafers and allowed to dry before being attached to carbon taped tipped metal stubs. The survey spectrum as well as the elements found in DNA (C, N, O, and P) are shown below in figure 5.2. The samples were calibrated using the C 1s scan in which was at a binding energy of 284.8 eV. This peak is usually due to the aliphatic carbon in methylene CH_2 groups.

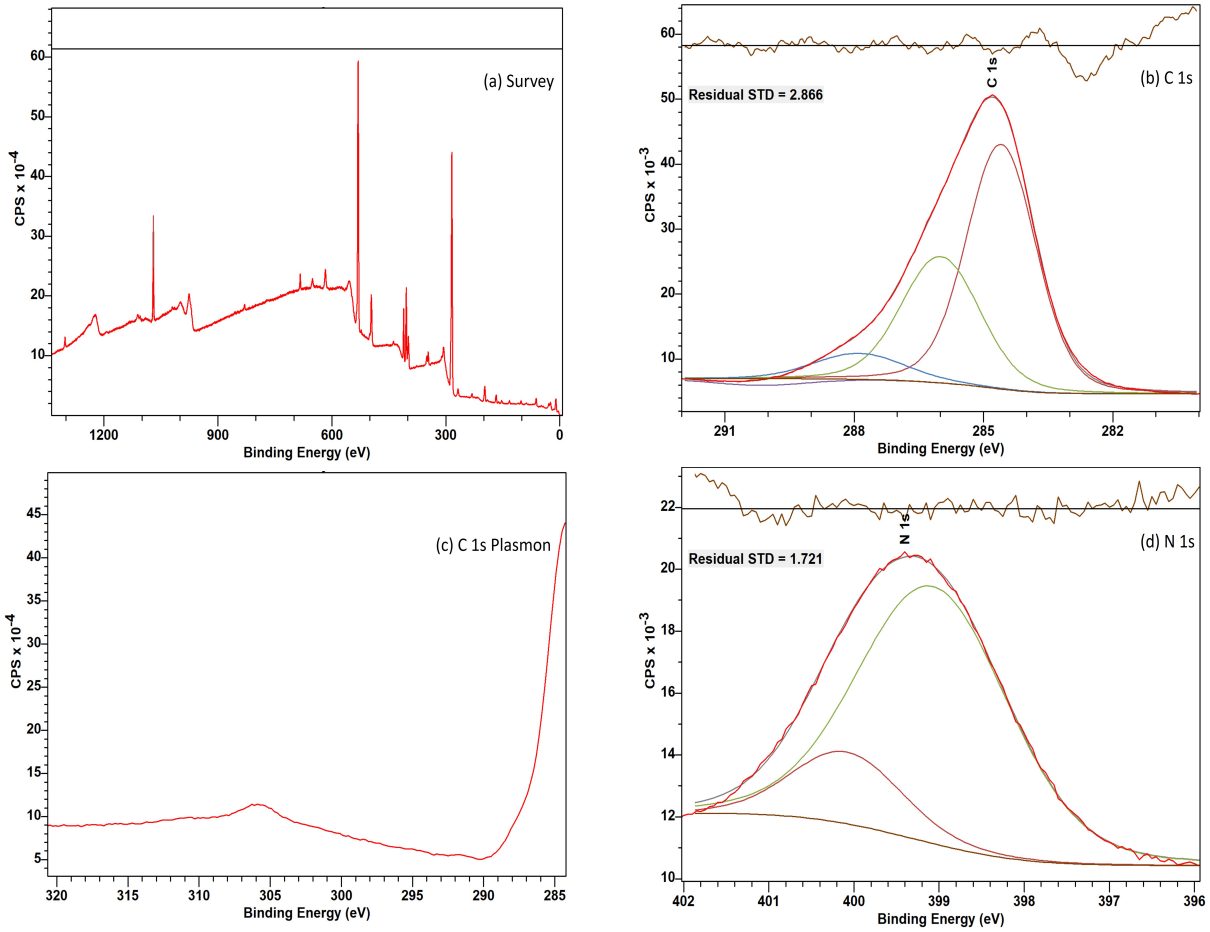

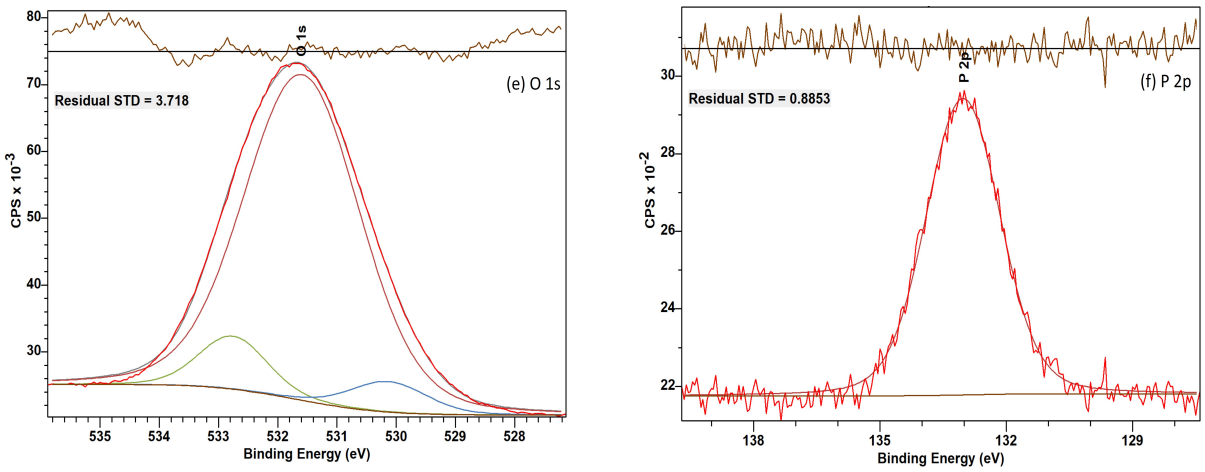

Figure 5.2: XPS spectra of CdS-CNT-DNA. The sample was dropcast onto a silicon substrate before measurement. The red curves show the experimental data and the others are fitted components. The residual fit is shown on the top of each spectra. (a) survey spectrum; (b) C 1s spectrum; (c) C 1s region showing evidence of a plasmon peak near 310 eV; (d) N 1s spectrum; (e) O 1s spectrum; (f) P 2p spectrum.

Further peaks at 286.0 and 287.8 eV were fitted within the C 1s spectrum. These are higher energy than the aliphatic carbon used for the calibration and can be assigned to C-O and C=O that is present within DNA bases. At 306 eV there is a small peak which could be attributed to a plasmon peak from the CNTs within the sample, however this in itself is not good enough evidence to confirm the presence of CNTs.[17] The first evidence of DNA being present within the sample comes from the 2 components at 399.1 and 400.1 eV in the N 1s spectrum. These peaks can be assigned to imines and amines respectively within DNA. This is further shown by the the ratio in which the two are present in which 83 % can be attributed to imines and 17 % for amines.[20] The P 2p peak at 133.0 eV can be assigned to the phosphate backbone of DNA.[21]

Combining both the P 2p and N 1s spectra shows clear evidence that DNA is present within the sample that cannot be interpreted as contamination.[17] The presence of CNTs are also suggested owing to a plasmon peak visible at 306 eV.

5.2.3 Fourier Transform Infrared Spectroscopy

FTIR can be used to compare the difference between bare λ-DNA and the CdS-CNT-DNA and observe any small shifts that can provide evidence for the binding of the CNTs or CdS. First a background was recorded using a clean silicon wafer after the instrument

had been purged with nitrogen. The CdS-CNT-DNA was then dropcast onto the silicon and allowed to dry, after which the spectra obtained. Figure 5.3 shows the FTIR for a sample of CdS-CNT-DNA.

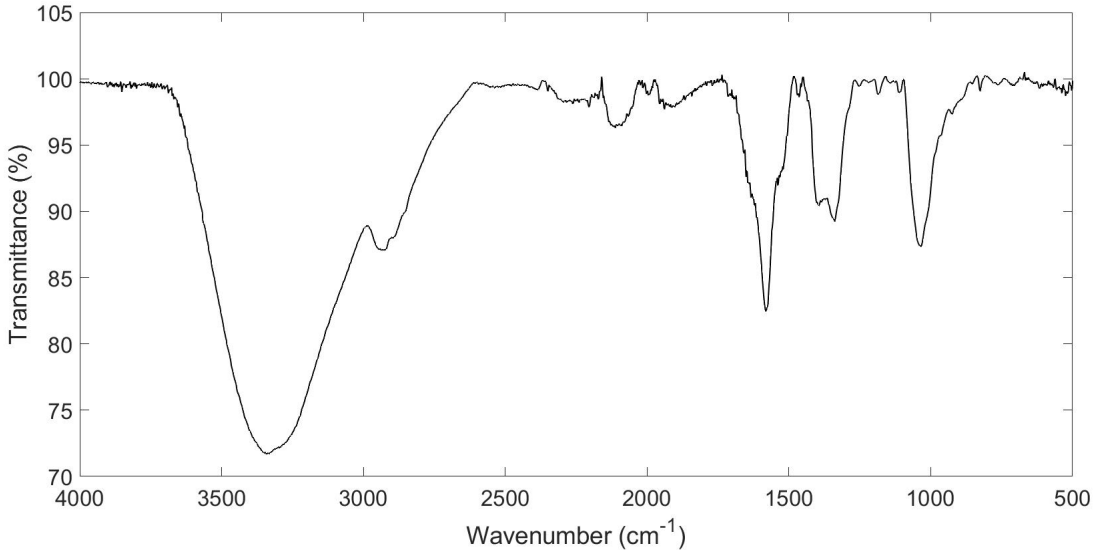

Figure 5.3: FTIR transmission spectra of CdS-CNT-DNA. The spectra was collected over 50 scans at 4 cm^{-1}

The peaks from 1830 - 2375 cm^{-1} are due to a difference in CO_2/H_2O levels between the background and sample. The largest variance between peaks comes at the peak assigned for the asymmetric stretch of PO_2^-. For bare DNA this peak appears at 1223 cm^{-1} however in the composite CNT-CdS-DNA sample this peak has shifted by 43 cm^{-1} to 1180 cm^{-1} indicating an interaction taking place between the negatively charged phosphate group and the CNTs.[22] There are also shifts seen for the peaks associated with the nucleobases however these are not as prominent as the phosphate backbone typically due to the phosphate interacting strongly with cations.[17] Nucleobases are positioned within the helical structure of DNA and are therefore are not in close contact with either the surface of the CNT or CdS causing the interactions to have a reduced effect. The literature FTIR values for bare DNA as well as the FTIR values for the measured CNT-CdS-DNA sample are summarised below in table 5.1

Wavenumber (cm^{-1}) in DNA	Wavenumber (cm^{-1}) in CNT-CdS-DNA	Assignment
1065	1035	C-O deoxyribose stretch / PO_2^- symmetric stretch
1223	1180	PO_2^- asymmetric stretch
1331	1340	C-N stretch
1408	1396	C-H, N-H deformation, C-N stretch
1531	1529	In plane vibrations of cytosine and guanine
1585	1579	C=N guanine and adenine C7=N stretch

Table 5.1: A comparison in the FTIR wavenumbers between CdS-CNT-DNA and literature values for bare DNA, along with an overview of the assignments given to each wavenumber.[23–25]

The shift in PO_2^- peak offers some indication that CNTs are present and are binding to the phosphate group. It can be deduced that binding is occurring on the phosphate groups more prominently due to the lower shifts found for nucleobases. This is due to them being further from the edge of the DNA helix.

5.2.4 Atomic Force Microscopy

AFM was used to investigate the structure of the CdS-CNT-DNA composite and the results can be found in figure 5.4 along with the accompanying height graph. Samples were prepared for atomic force microscopy by first diluting the CdS-CNT-DNA by a factor of 10^4. 2 μL of the diluted CdS-CNT-DNA was then dropcast onto cleaned silicon chips and left to dry in a laminar flow hood before being imaged. The image shows wire like structures with heights of 3 - 7 nm indicating these are not bare DNA. A Hybrid PbS-DNA-CNT and CdS-CNT-DNA structures have previously been prepared in which similar heights were obtained for AFM cross sections of PbS-CNT-DNA samples to the CdS-CNT-DNA samples reported in

this thesis. However, the comparison is not direct because the work of ye et al employed single-walled CNTs instead of the multi-walled CNTs used here.[18]

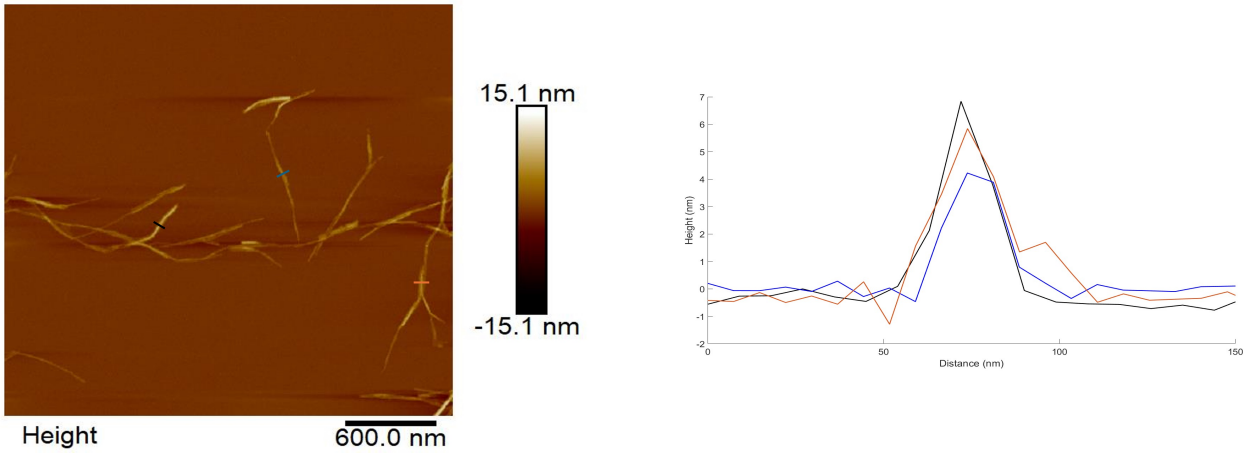

Figure 5.4: AFM image of CdS-CNT-DNA nanowires with the corresponding height graph. The coloured lines on the image match with the lines on the height graph.

AFM images were also recorded of CdS-CNT without the addition of DNA and the results can be found in figure 5.5 When no DNA has been added the image shows many randomly placed clumps of CNTs with no cohesion or wire like structures with heights of 7 - 8 nm which is higher that the spots growing on the DNA. The lack of any wire like structures shows that without the DNA present, wire formation is not facilitated. A control experiment in which a DNA-MWCNT composite without added CdS was not completed however this work has been characterised in the past by members of the research group and published.[17] What they found was a larger bundles of the composite compared to bare MWCNTs due to the strands clumping together. One suggestion is that in the absence of DNA, the MWCNTs do not adhere well to the chosen substrate and are transported to the edge of the deposited droplet during drying.

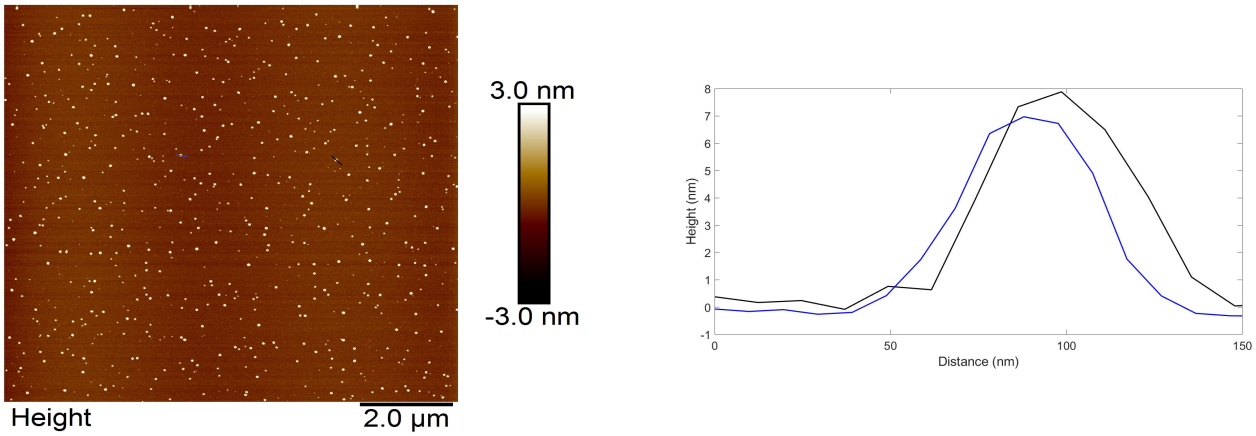

Figure 5.5: AFM image of CdS-CNT with the corresponding height graph. The coloured lines on the image match with the lines on the height graph.

AFM images of the CNT-CdS-DNA hybrid has shown wire like structures with heights ranging from 3 - 7 nm showing that these structures are not just bare DNA. This section also shows that without DNA present, there are no wire like structures present within the sample, only particulates with height of 7 - 8 nm.

5.2.5 IV Characterisation

Prior to incorporation into novel FETs the CNT-CdS-DNA had to be characterised in order to discover the electrical properties of which the first method was current-voltage measurements. 10 $\mu\mathrm{L}$ of CdS-CNT-DNA solution was dropcast onto a 10 $\mu\mathrm{m}$ platinum interdigitated electrode (IDE) and allowed to dry for 2 hours. After drying the IDEs were inserted into a Cascade Mirco-Tech probe station under a nitrogen atmosphere. Measurements were recorded in a nitrogen atmosphere in the dark in order to reduce any effect oxygen or potential photoconductivity may have on the results. If a sample is not sufficiently dry or oxygen is present then any interference from humidity or condensation is negated. An example IV curve recorded at 20 $^{\circ}\mathrm{C}$ can be seen in figure 5.6. This curve is interesting due to the non-ohmic shape that is usually not associated with the metal like conductance of MWCNTs.[26] A direct comparison with work completed by Ye in whici semiconducting SWCNTs were used the past cannot be made due to the differing CNTs.[18] This work focuses on metal-like MWCNTs.

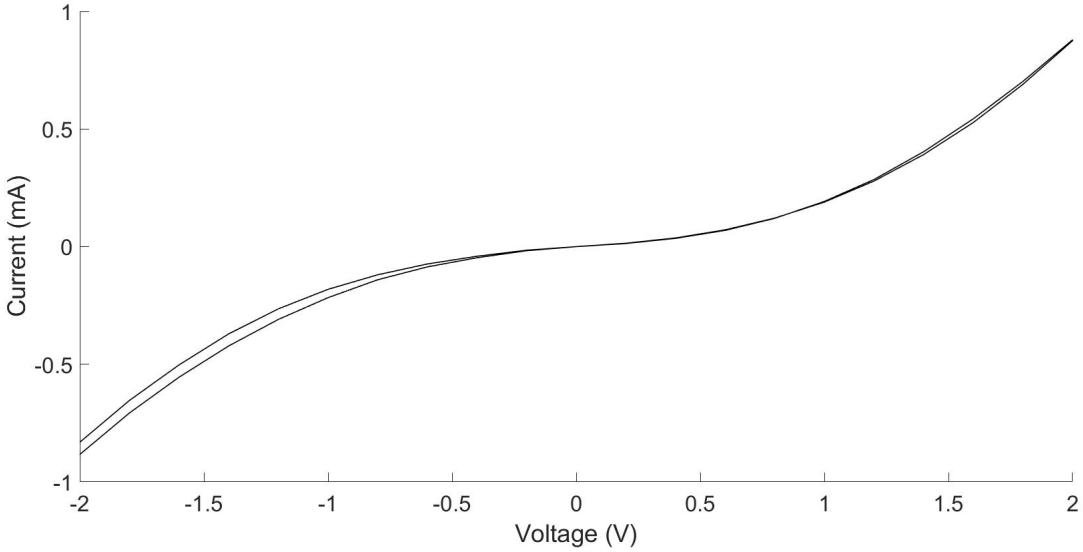

Figure 5.6: IV curve of CdS-CNT-DNA at 20 $^{\circ}\mathrm{C}$.

Figure 5.7 shows an IV curve of the used CNTs without the addition of DNA or CdS. The curve shows a high conductance with the current level exceeding the instrument compliance at just 0.2 A. The MWCNTs can be classed as metal like in the sense that they show a drop in conductance as the temperature rises.[17] The IV curves also provide evidence that CNTs are present within the sample due to the much larger current levels when compared to the CdS-DNA material mentioned in chapter 4. The current levels observed when measuring CdS-CNT-DNA were consistently found to be within the mA range, when compared to CdS-DNA, this is an increase by two orders of magnitude. This is a good indication that there are CNTs within the sample.

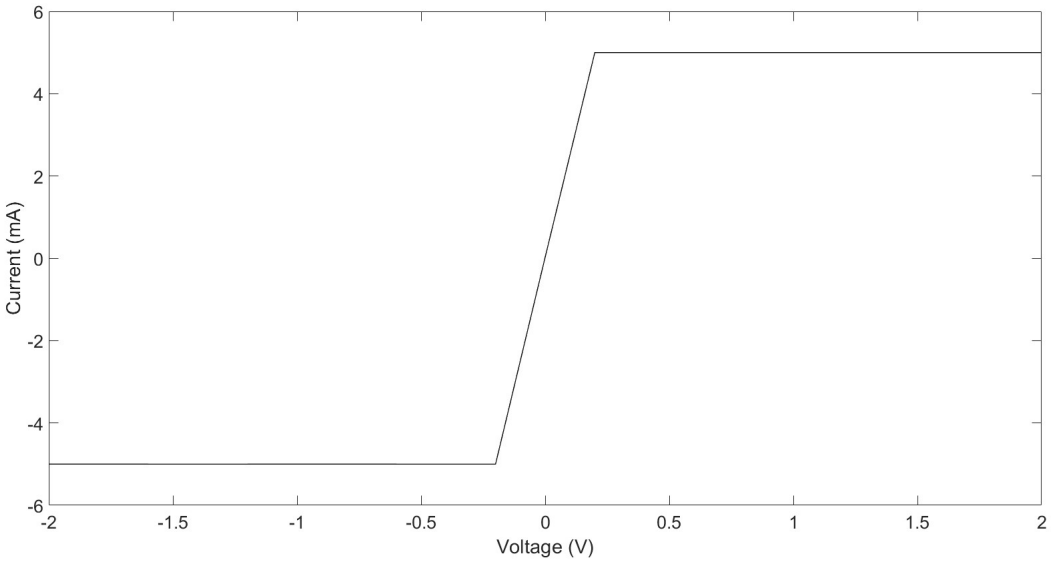

Figure 5.7: IV curve of MWCNTs at 20 $^{\circ}$C with no added DNA or CdS.

The difference in current levels observed between CdS-CNT-DNA and the pure MWCNTs is explained by a model which combines the metal like temperature dependence of the MWCNT conductivity and the activated process assigned to inter-tube hopping. The CNT-CdS-DNA composite electrical properties are modelled as a network of ohmic resistances from the MWCNTs and the tunnel junctions where carriers hop between the MWCNTs. The resistance of the inter-tube junctions (R_j) is given by equation 5.1:

$$R_j = R_j^0 exp\left(\frac{T_0}{T}\right)^{\beta} \tag{5.1}$$

in which R_j^0 and T_0 are constants that are determined by a regression analysis of the experimental data. The CNT-CdS-DNA composite is treated as if it had simple Arrhenius behaviour so that $\beta = 1$.[27] The contribution to the resistance of the DNA depends on the ratio of DNA:CNT and by using a linear function appropriate for a metal the temperature dependence can be given by equation 5.2:

$$R_m = a + bT \tag{5.2}$$

The overall resistance of the composite is assumed to be well approximated as a combination of equations 5.1 and 5.2 therefore the conductance is given by equation 5.3:

$$G = (R_j + R_m)^{-1} \tag{5.3}$$

To further investigate the electrical properties of the composite IV curves were recorded at intervals of 10 $^{\circ}\mathrm{C}$ between 20 - 100 $^{\circ}\mathrm{C}$. The conductance at zero bias was then extracted from the results and plotted against the temperature as found in figure 5.8. This figure shows the conduction is not solely through the MWCNTs due to the increase in conductance with temperature. Bare MWCNTs show a metallic like conductance in which an increase in temperature causes a decrease in conductance.[28] This also shows the vast improvement in conductance from CdS-DNA without the addition of CNTs mentioned in the previous chapter.

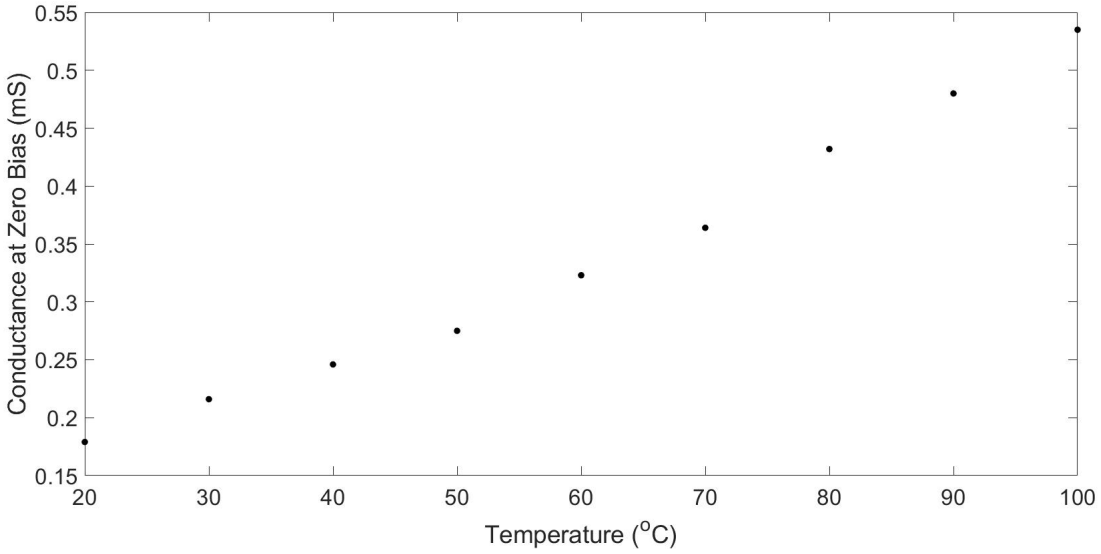

Figure 5.8: Temperature dependent conductance at zero bias of CdS-CNT-DNA over a range of 20 - 100 $^{\circ}\mathrm{C}$.

A plot of lnG against $1/T$ is shown below in figure 5.9 in which the activation energy can be calculated as 0.129 eV. As mentioned in section 4.2.4 if the origin of this value were simple thermal excitation of charge carrier across the band gap, then the activation energy would have been about half the gap, which for bulk CdS is $2.4/2 = 1.2$ eV.[29] The value of 0.129 eV is much lower than this meaning something else is occurring within the sample. This could potentially be hopping between the CdS crystals templated on the DNA and the CNTs. The barrier to hopping is lower in the CdS-CNT-DNA compared to the CdS-DNA due to the CdS crystals are connected with metal-like CNTs which facilitate charge transport more efficiently than the insulating DNA strands. When comparing work completed by Ali

wherein MWCNTs were wrapped with DNA and had the conductance measured, it is seen that the addition of CdS to the mixture increases the conductivity of the sample.[17]

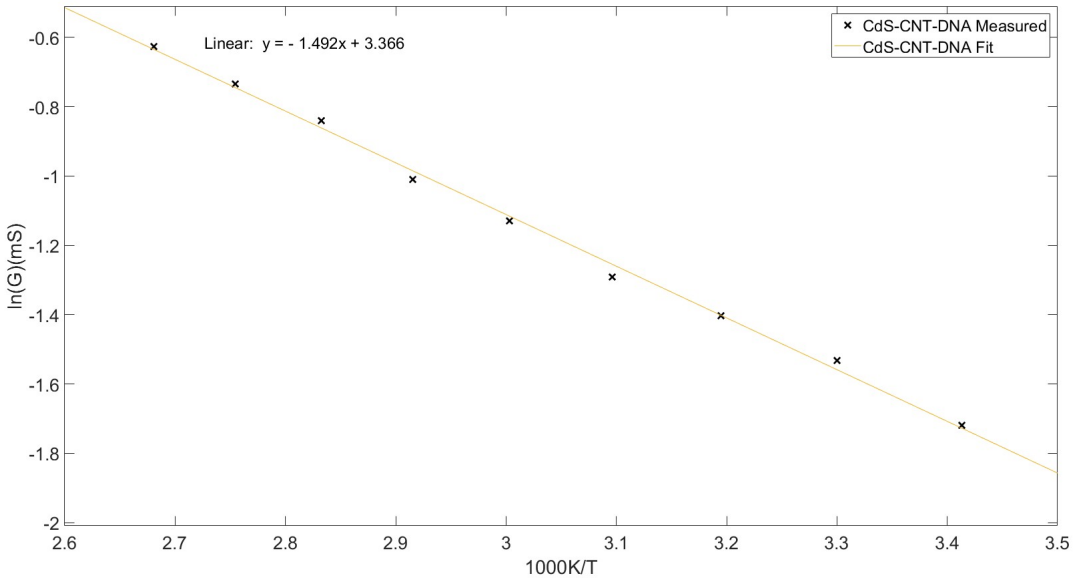

Figure 5.9: Arrhenius plot of CdS-CNT-DNA (black) with a linear fit (yellow).

This section shows the difference between IV curves of the CNT-CdS-DNA hybrid prepared, pure MWCNTs and CdS-DNA. It was found that the addition of CdS-DNA reduced the current levels at the same voltages as well as changing from a metal like conduction to a semiconducting behaviour, as shown by the conductance increasing as the temperature increases. When compared to CdS-DNA with no MWCNTs there is a large increase in conductance at zero bias. This suggests the MWCNTs help mitigate the low conductivity of the CdS-DNA and also remove the issue of large contact resistance.

5.2.6 Thin Film Transistor

The final stage for this composite was the incorporation into a TFT as done with the past 2 materials. Devices were prepared at discussed in section 2.4.2 and measured with a source-drain voltage of 0.1 V and a varying gate voltage. Figure 5.10 shows an example of the source-drain current measured whilst varying the gate voltage, using CdS-CNT-DNA as the weakly conducting material. Again with these devices, the overall successful yield was low with around 3 - 5 % of devices being successful per preparation. The black line

indicated the current at the source which rises from 4 μA to 5 μA when the gate potential is increased from 0 to 0.5 V. Th results shown in figure 5.10 show some improvements over the results in section 4.2.8 due to the overall increase in current between the source and drain. Despite this, there is still no clear gating such as an on/off response commonly expected with FET devices. As mentioned in section 3.2.10 the next stage would be to fabricate a device with a larger service area such as the interdigitated electrodes used for two-terminal measurements or elongating the source and drain contact points in order to increase the surface area.

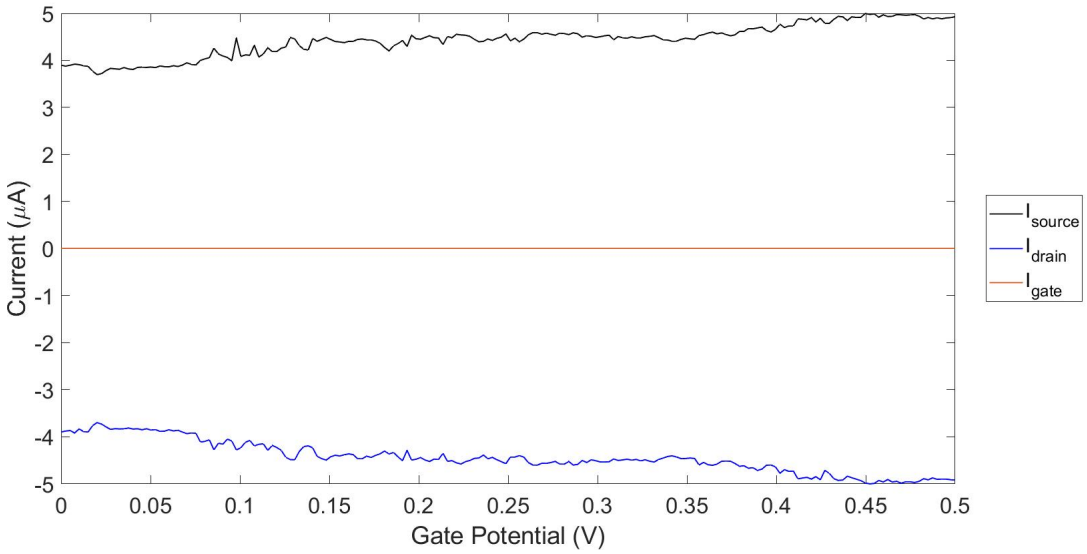

Figure 5.10: Drain current plotted against gate potential curve for a CdS-CNT-DNA FET.

5.3 Conclusion

A composite material has been prepared using cadmium sulphide, carbon nanotubes and DNA to form a weakly conductive material with a wire like structure. XPS proved that DNA was present within the sample due to the N 1s and P 2p peaks and an argument could be made that a plasmon peak around 306 eV shows CNTs present. FTIR has been used in order to show the difference in spectra between bare DNA and DNA within the CdS-CNT-DNA composite. Large variances were found between the PO_2^- peaks with a difference of 43 cm^{-1} indicating a reaction between the phosphate backbone of DNA and the CNTs. AFM studies then showed wire like structures with heights exceeding the expected height of bare DNA indicating templating had occurred. Without the presence of DNA, wire structures

were not present, instead small dots with height of 7 - 8 nm were imaged. Electrical measurements showed semiconducting like properties compared to the metallic behaviour normally shown by the CNTs used. The CNTs used in this research were metallic in regards that as the temperature increases, the conductance drops. When incorporated into a thin film transistor there was a slight increase in source / drain current when the gate voltage was varied however this was not as successful as the VO_2 results. Future work on this would be to vary the ratios of DNA:CNT in order to deduce the full effect DNA has and potentially created a tunable semiconducting material.

Bibliography

[1] P. R. Bandaru, *Journal of Nanoscience and Nanotechnology*, 2007, **7**, 1239–1267.

[2] P. V. Dudin, M. E. Snowden, J. V. Macpherson and P. R. Unwin, *ACS Nano*, 2011, **5**, 10017–10025.

[3] B. Arash, Q. Wang and V. K. Varadan, *Scientific Reports*, 2014, **4**, 6479.

[4] T. W. Odom, J.-L. Huang, P. Kim and C. M. Lieber, *Nature*, 1998, **391**, 62–64.

[5] S. G. Louie, in *Carbon Nanotubes: Synthesis, Structure, Properties, and Applications*, ed. M. S. Dresselhaus, G. Dresselhaus and P. Avouris, Springer, Berlin, Heidelberg, 2001, pp. 113–145.

[6] T. W. Ebbesen, H. J. Lezec, H. Hiura, J. W. Bennett, H. F. Ghaemi and T. Thio, *Nature*, 1996, **382**, 54–56.

[7] T. Fukuda, F. Arai and L. Dong, *Proceedings of the IEEE*, 2003, **91**, 1803–1818.

[8] R. Martel, T. Schmidt, H. R. Shea, T. Hertel and P. Avouris, *Applied Physics Letters*, 1998, **73**, 2447–2449.

[9] S. Darwin, E. F. Irudaya Rani, E. F. Irudaya Raj, M. Appadurai and M. Balaji, 2022 6th International Conference on Trends in Electronics and Informatics (ICOEI), 2022, pp. 25–31.

[10] E. S. Snow, P. M. Campbell, M. G. Ancona and J. P. Novak, *Applied Physics Letters*, 2005, **86**, 033105.

[11] M. C. LeMieux, M. Roberts, S. Barman, Y. W. Jin, J. M. Kim and Z. Bao, *Science (New York, N.Y.)*, 2008, **321**, 101–104.

[12] P. Beecher, P. Servati, A. Rozhin, A. Colli, V. Scardaci, S. Pisana, T. Hasan, A. J. Flewitt, J. Robertson, G. W. Hsieh, F. M. Li, A. Nathan, A. C. Ferrari and W. I. Milne, *Journal of Applied Physics*, 2007, **102**, 043710.

[13] Y. Asada, Y. Miyata, Y. Ohno, R. Kitaura, T. Sugai, T. Mizutani and H. Shinohara, *Advanced Materials*, 2010, **22**, 2698–2701.

[14] R. A. Zangmeister, J. E. Maslar, A. Opdahl and M. J. Tarlov, *Langmuir*, 2007, **23**, 6252–6256.

[15] M. Zheng, A. Jagota, E. D. Semke, B. A. Diner, R. S. Mclean, S. R. Lustig, R. E. Richardson and N. G. Tassi, *Nature Materials*, 2003, **2**, 338–342.

[16] X. Huang, R. S. Mclean and M. Zheng, *Analytical Chemistry*, 2005, **77**, 6225–6228.

[17] S. B. Ali, A. B. Oshido, A. Houlton and B. R. Horrocks, *Nanotechnology*, 2021, **33**, 1 – 15.

[18] Q. Ye, X. Xu, A. Paghi, T. Bamford, B. R. Horrocks, A. Houlton, G. Barillaro, S. Dimitrov and M. Palma, *Advanced Functional Materials*, 2021, **31**, 2105719.

[19] R. N. Nurdillayeva, A. B. Oshido, T. A. Bamford, O. El-Zubir, A. Houlton, J. Hedley, A. R. Pike and B. R. Horrocks, *Nanotechnology*, 2018, **29**, 135704.

[20] E. Mateo-Martí, C. Briones, C. M. Pradier and J. A. Martín-Gago, *Biosensors and Bioelectronics*, 2007, **22**, 1926–1932.

[21] A. Stypczyńska, T. Nixon and N. Mason, *The European Physical Journal D*, 2014, **68**, 333.

[22] X. Guo, A. A. Gorodetsky, J. Hone, J. K. Barton and C. Nuckolls, *Nature Nanotechnology*, 2008, **3**, 163–167.

[23] S. Alex and P. Dupuis, *Inorganica Chimica Acta*, 1989, **157**, 271–281.

[24] A. A. Ouameur and H.-A. Tajmir-Riahi, *Journal of Biological Chemistry*, 2004, **279**, 42041–42054.

[25] G. I. Dovbeshko, N. Y. Gridina, E. B. Kruglova and O. P. Pashchuk, *Talanta*, 2000, **53**, 233–246.

[26] J.-H. Pöhls, M. B. Johnson, M. A. White, R. Malik, B. Ruff, C. Jayasinghe, M. J. Schulz and V. Shanov, *Carbon*, 2012, **50**, 4175–4183.

[27] P. Sheng, B. Abeles and Y. Arie, *Phys. Rev. Lett.*, 1973, **31**, 44–47.

[28] A. Lekawa-Raus, K. Walczak, G. Kozlowski, M. Wozniak, S. C. Hopkins and K. K. Koziol, *Carbon*, 2015, **84**, 118–123.

[29] Z. H. Zhang, W. S. Chin and J. J. Vittal, *J. Phys. Chem. B*, 2004, **108**, 18569–18574.

Chapter 6

Conclusion and Future Work

6.1 Conclusion

This thesis has shown three examples in which DNA has been used as a template to help facilitate the growth of weakly conducting nanowires from the materials VO_2 and CdS. The third example employed DNA to adhere to multi-walled carbon nanotubes and then CdS was formed using the DNA to provide nucleation sites; this is referred to as CdS-CNT. Furthermore, it has been shown that nanowires prepared in this fashion using VO_2-DNA can form working thin film field effect transistors.

VO_2 nanowires have been prepared in the past using various methods and in chapter 3 a new method has been demonstrated. The addition of λ-DNA to VO_2 leads to wire like formations with heights upwards of 12 nm. The new material has been characterised chemically using a variety of different spectroscopic tools. UV-Vis absorbance spectroscopy has been used to show the presence of DNA within the sample as well as help follow the reaction as it proceeds from V_2O_5 to the finished product which is in the V(IV) oxidation state. FTIR then provides evidence that interactions are occurring between the negatively charged phosphate backbone and the V(IV) species due to a shift of the PO_2^- stretching modes. This is then further backed up by a small change in binding energy for V $2p_{\frac{3}{2}}$ when samples are analysed with X-ray photoelectron spectroscopy. The structure was then analysed using pXRD revealing a matching pattern for VO_2 nanorods. AFM and scanned conductance microscopy (SCM) were used to investigate the structural and electronic properties of the VO_2/DNA nanowires. The sample presented wire like formations with heights upwards of 12 nm compared to bare DNA which presents at 1 nm $\geqslant$ in AFM studies. SCM then indicated that the wires were weakly conducting due to the shape of the phase shift

in which there is a negative - positive - negative variation in phase as the tip is scanned across the nanowire. To probe this further, two-terminal IV curves were recorded over a temperature range of 20 - 100 $^{\circ}\mathrm{C}$. Over this temperature range an overall increase in conductance was found which provides evidence of the non-metallic nature of the material. An activation energy for the transport was estimated as about 0.19 eV, although the lnG vs 1/T plot shows deviation from linearity. The temperature dependence can be interpreted in terms of a hopping model of transport appropriate for grannular materials. Nevertheless, VO_2 templated on DNA was found to show higher conductance than previous metal oxide or metal sulfide/DNA templated systems. The final stage was the incorporation of the VO_2-DNA into a thin film FET in which basic functionality was found. This marked the first time that nanowires prepared by using DNA as a template were successfully used within a FET device. The effect of varying the gate voltage was small however. A possible explanation is that the gate voltage is less effective at changing the local concentrations of the charge carriers than in a single crystal semiconductor material.

Chapter 4 focused on the characterisation and optimisation of CdS-DNA nanowires. UV-Vis spectroscopy was first used in order to show the presence of DNA within the sample due to the characteristic absorption peak at 260 nm. The material was then imaged with AFM, showing wire formations with heights of 5 nm. The semiconducting like nature of the material was then shown due to the increase in conductance with an increase in temperature. An activation energy of 0.82 eV was extracted from the linear plot of lnG against 1/T. If the conductivity were determined by thermal excitation of electrons across the gap, this would predict an activation energy $E_g/2 = 1.2$ eV. The conductance was also found to be much lower (5-6 orders of magnitude) than that for VO_2/DNA. Impedance spectra indicated that there is a large contact resistance in these devices which is partly responsible for the difference between the CdS and VO_2 systems. In order to measure IV curves, the sample is dropcast onto a platinum interdigitated electrode (IDE) and allowed to dry in a vacuum oven. In an attempt to optimise this, directionality was introduced to the nanowires. This was done by holding the sample at 45 $^{\circ}$, altering the surface hydrophobicity of the IDE and a gentle stream of nitrogen blowing over the sample. This resulted in a consistent increase in conductance and is thought to be due to the nanowires spanning the distance between contact points within the IDE, meaning electrons can travel between these points more

efficiently. However, incorporation of CdS-DNA into a thin film FET was not successful due the overall lack of conductivity shown by the material as well as high contact resistance.

The final material investigated followed on from the CdS-DNA found in chapter 3 by incorporating multi-wall carbon nanotubes (MWCNTs) into the preparation in order to increase the conductance compared to CdS by itself. DNA was shown to be present within the sample by using XPS. The N 1s spectrum has two peaks which could be assigned to imines and amines consistent with what is found in DNA. Combining with the presence of a P 2p peak was good evidence that DNA was present within the sample. To then investigate the interactions between the DNA and MWCNTs FTIR was used. Large variances were found between the PO_2^- peak in bare DNA and that found in CdS-CNT-DNA, indicating a strong CdS-DNA interaction is taking place. The structure of the material was then investigated using AFM in which wires with heights of 4 - 5 nm were found. A large difference can be found when comparing images of CdS-CNT-DNA and CdS-CNT with no added DNA. When DNA is absent there are no wire like structures, only small dots with heights of 7 - 8 nm indicating the DNA facilitates the growth of the nanowires. IV measurements recorded showed curves with non-ohmic behaviour that is not usually associated with the metal-like conductance of MWCNTs. When measured over a temperature range the material showed a semiconducting nature - an increase in conductance with temperaure. In contrast the MWCNTs show a resistance rising linearly with temperature. When the material was incorporated into a thin film FET there was transistor like behaviour however the effect was weaker than the VO_2-DNA discussed in chapter 3.

In closing, a number of steps have been made in incorporating DNA-templated nanowires into thin film FETs with both VO_2-DNA and CdS-CNT-DNA showing basic transistor functionality. Future studies should focus on the optimisation of the FET design to maximise the surface area the material has to contact.

6.2 Future Work

There ware two main successes in this work with those being the preparation and testing of the new material VO_2-DNA as outlined in chapter 3 and the the angled drying method as mentioned in section 4.2.7.

The main areas for future work with the VO_2-DNA would be to further characterise the

electrical properties of the material and to prepare the templated nanowires with the different phases of VO_2 such as M and A. The M phase especially shows promising properties such as a metal to insulator transition at 68 $^{\circ}\mathrm{C}$ or via an electrical pulse. The incorporation of this material into a FET like device could potentially open up interesting ways to switch a FET on or off depending on the temperature of the device or by injecting an electrical pulse. With regards to future work with the prepared VO_2-DNA, improved FET designs could be utilised in order to further investigate the gate dependence of the material. A potential final use of the material would be within printed electronics due to the aqueous nature of the material meaning it can be prepared as an ink. This has been attempted within the group before using the CdS-DNA system however due to the large improvement in conductance shown by the VO_2-DNA this could show more potential.[1]

The other main area which should be investigated further is the angled drying of the nanowire systems. Currently, molecular combing is the main technique used for aligning DNA for imaging and analysis however issues can often arise with the silanized coverslips, the pulling rate and potential damage to the DNA. The method shown in section 4.2.7 is a non-contact method for the alignment of fibres which uses a steady flow of nitrogen over the sample. Some optimisation was carried out in this work regarding the surface hydrophobicity in order to control the flow along the silicon sample. To further improve on this other aspects should be investigated such as the concentration of the DNA solution, the flow rate of the nitrogen and the angle the sample is held at. The concentration of the DNA solution can effect how well the fibres can travel within the solvent as a high concentration will reduce the flow. The method carried out in this work used a pipe connected directly to a nitrogen pump within the fumehood with no precise control over the flow rate. By altering the flow rate of nitrogen the distance the DNA fibres travel will be altered. Finally the angle at which the sample is held also makes a difference to the distance travelled by the DNA fibres.

Bibliography

[1] R. N. Nurdillayeva, A. B. Oshido, T. A. Bamford, O. El-Zubir, A. Houlton, J. Hedley, A. R. Pike and B. R. Horrocks, *Nanotechnology*, 2018, **29**, 135704.